Future Tropical Cyclone-Induced Coastal Flood Hazards in Sofala Province, Mozambique

A Probabilistic-Storyline Framework

Fernaldi Gradiyanto

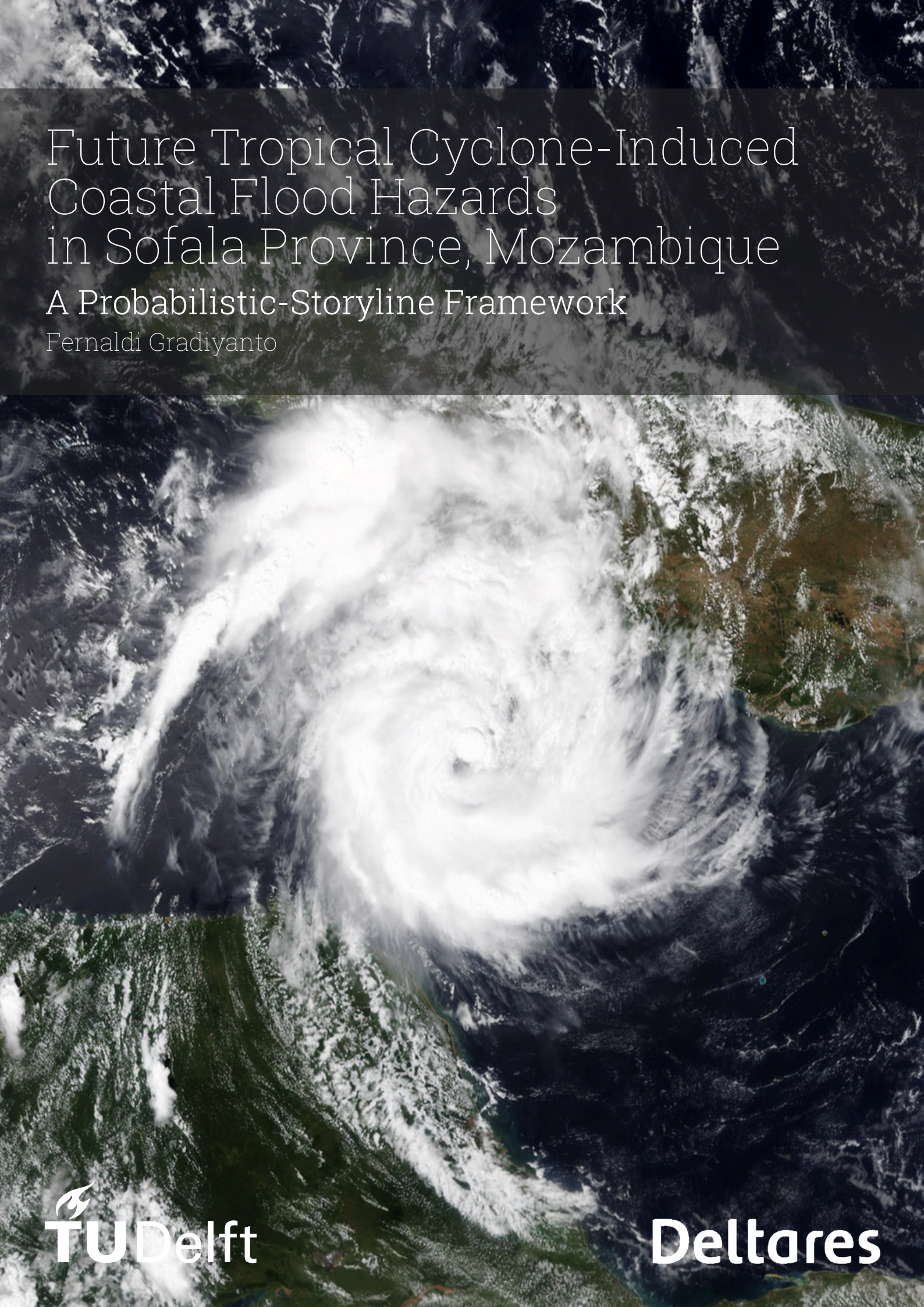

TU Delft

Deltares

Future Tropical Cyclone-Induced Coastal Flood Hazards in Sofala Province, Mozambique

A Probabilistic-Storyline Framework

by

Fernaldi Gradiyanto

An electronic version of this thesis is available at http://repository.tudelft.nl/

The work in this thesis was carried out at:

Hydraulic Engineering Department
Section of Coastal Engineering
Delft University of Technology

Hydrodynamic and Forecasting Department
under the EU Horizon COMPASS Project
Deltares

In partial fulfilment of the requirements for the degree of

Master of Science

In Civil Engineering - Hydraulic Engineering
At the Delft University of Technology

to be defended publicly on Wednesday, August 27, 2025, at 14:30 CET.

Chair committee:	Dr.ing. José A. Álvarez Antolínez	Delft University of Technology
Committee members:	Dr.ir. Renske Gelderloos	Delft University of Technology
	Dr.ir. Tim Leijnse	Deltares
	Dr.ir. Anaïs Couasnon	Deltares

Cover: "*Tropical Cyclone Idai in the Mozambique Channel*" by NOAA
Style: TU Delft Report Style, with modifications by Daan Zwaneveld

Acknowledgment

This thesis completes my master's journey in hydraulic engineering at what used to be and what still is my dream campus, Delft University of Technology. A journey that began at least four years ago, when I first started preparing for the English test, scholarship selection, and TU Delft admission. Reflecting on my arrival in Delft exactly two years ago, I can hardly believe how much I have grown, personally, professionally, and academically.

A significant part of that growth I should owe to my outstanding and energetic thesis supervisory team. I would like to express my deepest gratitude to Anaïs for the opportunity to join the COMPASS project at Deltares as an intern in September 2024, and for trusting me again to undertake this ambitious thesis as a graduate intern. I truly enjoy our conversations and deeply value your advice, which has guided both my personal growth and academic journey. To Tim, my coolest daily supervisor, I am forever grateful for your continuous critical feedback and encouragement like no other. I can't thank you enough for your guidance on hydrodynamic modelling and our weekly technical brainstorming (and of course for the constant reminders to keep my presentations clear and concise :D). To José, my chair since day one, thank you for your wisdom and knowledgeable insight at every meeting. I will do my best to carry your advice with me, keeping my work focused, innovative, and impactful as I move forward in my career. And of course, to Renske, I genuinely appreciate your highly detailed feedback at every stage of my report, as well as your perceptive questions and for always radiating cheerful energy in our monthly meetings. Last but not least, I would like to thank the COMPASS team, Natalia, Doris, and Sanne, for always making me feel welcome and for your feedback and support throughout this thesis period.

For those who make this whole journey possible, I would like to especially thank the Indonesia Endowment Fund for Education (LPDP-RI) under Indonesia's Ministry of Finance, which has sponsored me to pursue a fully-funded master's study here in Delft. To Mama and Bapak, thank you for your unwavering support and love, even before this journey was thought of. To my partner, Tania, thank you for always being there for me, to listen, share, laugh, love and care through the endless cycle of hours-long video calls. Also, to my fellow Indonesian peers at Delft, who make this academic journey more colourful and enjoyable. I will forever cherish this chapter of my life, and I genuinely hope that I can contribute my gained knowledge and experience here to the development of our beloved country, Indonesia.

To end, this thesis represents the "hardest work" I have ever dedicated to yet, and I hope it will contribute meaningfully, both academically and beyond. Happy reading.

Fernaldi Gradiyanto
Delft, August 2025

Abstract

This study investigates how projected changes in tropical cyclone (TC)-induced storminess, defined by extreme wind, surge, and wave events, will affect coastal flood hazards along the Sofala coastline in Mozambique under the near-future SSP5-85 climate scenario (up to year 2050). While global studies have suggested intensified storm characteristics in the Sofala region, no study to date has assessed their implications for regional coastal flood hazard in conjunction with sea-level rise (SLR). Using the synthetic STORM dataset in combination with probabilistic extreme value analysis and a storyline-based TC Idai simulation, this study quantifies the projected increase in TC-induced hazards and evaluates the relative contribution of storminess change and SLR to future flood depth and extent. Results show a consistent upward shift in the 100-year return levels for wind, surge, and wave. These changes can be mainly statistically attributed to the exceedance frequency (i.e., how often extremes occur) rather than exceedance intensity (i.e., how extreme they are when they occur). As such, the effective return period of historical 100-year events is found to be 45–60 years on average under the near-future scenario, suggesting that extreme events will become significantly more frequent. Although the upper tail dependence between surge and wave slightly weakens, the likelihood of joint surge–wave extremes still increases, lowering the joint return period from an average of 200 years to 120 years. In the TC Idai storyline, SLR accounts for 60–90% of the increase in total water levels, with a magnitude of around 0.25 m. However, storminess change contributes up to 40% in some areas, and is shown to substantially heighten flood extent and population exposure. The findings underscore the importance of integrating TC-induced storminess change in Sofala's future coastal hazard assessments, in addition to SLR. Recommendations include extending analyses to additional synthetic TC models and emissions scenarios (e.g. SSP2-45), improving hydrodynamic model validation, and incorporating rainfall and fluvial forcing to capture the full spectrum of compound flood hazards under a changing climate.

Keywords: *STORM dataset, Tropical Cyclone, Climate Change, Storyline Approach, Storm Surges, Wave, Coastal Flood Hazard, Delft3D, SFINCS*

Contents

1

Introduction

1.1. Research Context

Sofala Province is a central pillar of Mozambique's economy and regional connectivity. With its strategic coastal location along the Indian Ocean, this province served as a vital gateway for trade and logistics. It is regarded as the host of the oldest port in Southern Africa, dating back to the tenth century, before it was relocated to the city of Beira around the beginning of the nineteenth century (Britannica 2025). Beira is now anchored as the capital of Sofala Province and the second largest city in Mozambique, home of the busiest port in the country, still regarded as a crucial transit for landlocked neighbouring countries, supported by major roadways and a key international airport (Filipe et al. 2017). The province's economy is diversified, encompassing agriculture, fisheries, and manufacturing, and its transport infrastructure underpins both national and international commerce, making it indispensable to Mozambique's socio-economic framework (World-Bank 2019).

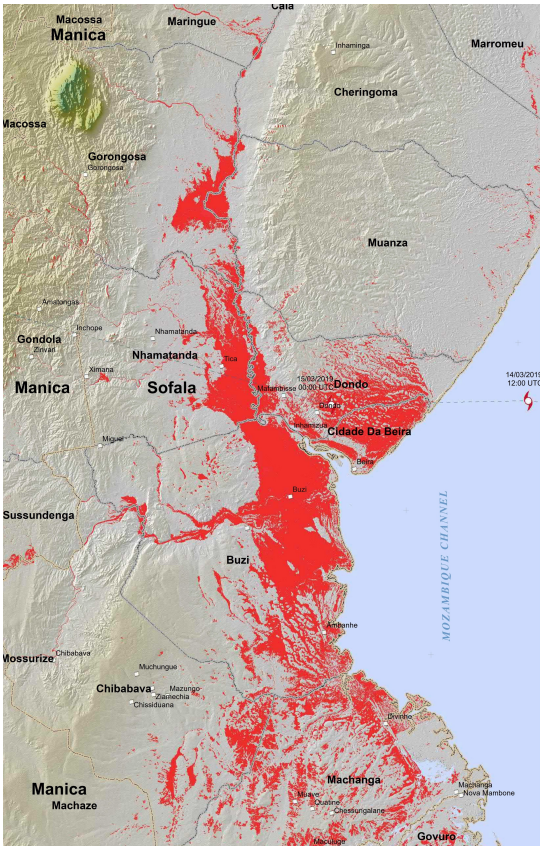

Figure 1.1: UNOSAT Cumulative Tropical Cyclone Idai Flood Map (UNITAR 2019). The red mark indicated flood extent derived from analysis based on satellite imagery.

However, Sofala province, being in the heart of the warm tropical waters of the Indian Ocean, is prone to Tropical Cyclone (TC)-induced hazards such as extreme winds, storm surges, and river flooding (Deltares 2021; Eilander et al. 2023b). Considering that the densely populated areas mainly reside in the province's low-lying terrain along Sofala Bay, especially around Beira and the delta of Buzi and Pungue rivers (CIESIN 2018), it denotes a significant flood hazard exposure, especially when cyclones make landfall. Vulnerabilities such as chronic poverty, rapid urbanisation, and limited disaster-resilient infrastructure amplify the risks, often resulting in widespread displacement, destruction of critical infrastructure, and severe disruptions to livelihoods and food security (Williamson 2022).

Tropical Cyclone Idai, which struck Sofala in March 2019, exemplified the severity of these risks (see Figure 1.1). Making landfall near Beira with winds of 180–220 km/h (Knapp et al. 2010), torrential rains exceeding 200 mm in 24 hours and a skew surge of around 2 meters (Eilander et al. 2023a), Idai unleashed devastating floods. Due to the compound fluvial, pluvial and coastal flooding as well as wind hazards, over 70% of Beira was reported damaged or destroyed, crippling logistics infrastructure such as the airport and seaport due to intense wind and surge (UNDP 2019). The cyclone displaced nearly 400,000 people, destroyed more than 715,000 hectares of crops, and left over 1.5 million people affected, with at least 600 fatalities and

thousands injured, making it regarded by World Meterorological Organization (WMO) as ”One of the Worst Weather-related Disasters in the Southern Hemisphere” (UNDP 2019; UNITAR 2019). Such events highlight the importance of developing robust flood adaptation strategies and protection measures.

Reducing TC-induced flood hazard effectively depends on learning from past events to understand the risks and vulnerabilities involved; however, because conditions and hazard patterns can change over time, it is also crucial to consider how these hazards might evolve (UNDRR 2024). Critical components when considering the future TC-induced flood hazard, especially in the context of coastal flooding, are its response to sea level rise (SLR) (Woodruff et al. 2013; Xu et al. 2022; Grimley et al. 2024) and storm climatology change (Emanuel 2008; Lee et al. 2020; Bloemendaal et al. 2022), or what is often called the change of ”storminess”. Storminess here corresponds to the magnitude as well as the temporal and spatial pattern of extreme wind, which thus also affects the surge and wave generation (Leijnse et al. 2022; Bakker et al. 2022). These evolving drivers can amplify coastal flood risks by raising baseline water levels and modifying the intensity or frequency of storm tides, which consist of the combination of tide, TC-induced surge, and wave-induced water level components (Lin et al. 2012; Marsooli et al. 2019; Gori et al. 2022). Therefore, integrating historical analysis with forward-looking scenario modelling is essential for designing resilient and adaptive coastal protection measures.

1.2. Research Problem

Past studies have provided indications of an increased TC-induced coastal flood hazard around the Sofala region under future climate scenarios. Goulart et al. (2025) demonstrated that superimposing a sea level rise (SLR) scenario associated with 3°C warming by 2100 could increase the population exposure to TC Idai’s coastal flooding by approximately 80%. Regarding changes in storminess, Bloemendaal et al. (2022) projected an increase of about 5–10 m/s in 100-year return period TC-induced wind speeds for this region. Extending these findings, Grossmann-Matheson et al. (2024a) estimated a rise of 0.5–1 m in offshore significant wave heights. Muis et al. (2023) projected a 10% increase in 100-year return period storm surge levels over the 2021–2050 period, although this estimate does not explicitly isolate TC-induced events and therefore may under-represent the intense localised storms.

Despite these signals of changing storm characteristics from global-scale studies presented above, no study to date has explicitly assessed how storminess changes would translate into future total water levels and flood hazard at a finer regional scale along the Sofala coastline. In contrast, studies focusing solely on SLR effects, such as Goulart et al. (2025) and Deltares (2021), risk considerably underestimating future flood hazards by neglecting dynamic storm contributions. One instance is given by Marsooli et al. (2019), in which the TC climatological change effect on 100-year return period surge levels is shown to have a comparable magnitude proportion to the SLR at the Gulf of Mexico coast; meanwhile, it has less contribution in the US east Atlantic coast. However, for the Sofala region, the individual and combined effects of TC-induced storminess changes and SLR on coastal flood hazards remain largely unexplored. This includes their spatial variability, which has yet to be adequately assessed.

1.3. Research Objectives

To bridge this critical gap, this research’s first objective is to quantify the change of storminess—wind, surge, and wave—on a regional scale. This requires bringing global-scale studies on storminess change presented by Grossmann-Matheson et al. (2024b) and Muis et al. (2023) into a regional scale, employing consistent input of a synthetic tropical cyclone database under the current and future climate, STORM-IBTrACS (Bloemendaal et al. 2020c; Bloemendaal et al. 2020b) and STORM-CC (Bloemendaal et al. 2021; Bloemendaal et al. 2022). STORM-IBTrACS and STORM-CC are open-source datasets consisting of global 10,000 years of synthetic tropical cyclone tracks for current and future climate, respectively (a full explanation of these datasets is presented in Chapter 3).

Given that TC-induced events dominate the upper tail of the hazard distributions (Dullaart et al. 2021), particular emphasis is placed on assessing how climate change alters the marginal and joint return period curves for wind, surge, and wave along Sofala’s coastline. In marginal cases, emphasis is placed on the shift in wind, surge, and wave magnitude at a specific return period and what statistical attribution best characterises this change. These statistical attribution refers to either extreme frequency (i.e.,

how often extremes occur) or extreme intensity (i.e., how extreme they are when they occur). In the joint cases, specifically joint surge and wave extremes, emphasis will first be placed on extremal dependence, that is, how likely surge and wave are to become extreme simultaneously. For both marginal and joint cases, the effective return period will be evaluated, which is defined as the return period in the future climate corresponding to the same wind, surge, and wave magnitude associated with a given return period under the current climate.

As changes in storminess and its spatial variability are identified, their contribution to future coastal flood hazards can be systematically assessed. This assessment, particularly in comparison to the effects of sea level rise (SLR), constitutes the second objective of this study. Unlike the approach adopted by Marsooli et al. (2019), which compares SLR contributions to changes in the 100-year return period surge levels, this study evaluates storminess-related water level magnitude changes: wave runup (setup + swash) and skew surge, based on the return period associated with TC Idai in a spatially varying manner. This approach is commonly referred to as a probabilistic-scaled past event (see red dots in Figure 1.2). Combining this with a sea level rise counterfactual scenario as presented in Goulart et al. (2025) produces a combined probabilistic and storyline framework (equivalent to the blue dots presented in Figure 1.2). This combined approach not only quantifies changes in hazard magnitudes but also preserves the physical coherence and realism of extreme event characteristics under future climate conditions. This approach further enhances the communication of risks by providing tangible, event-based narratives that are easier for stakeholders and decision-makers to understand and act upon.

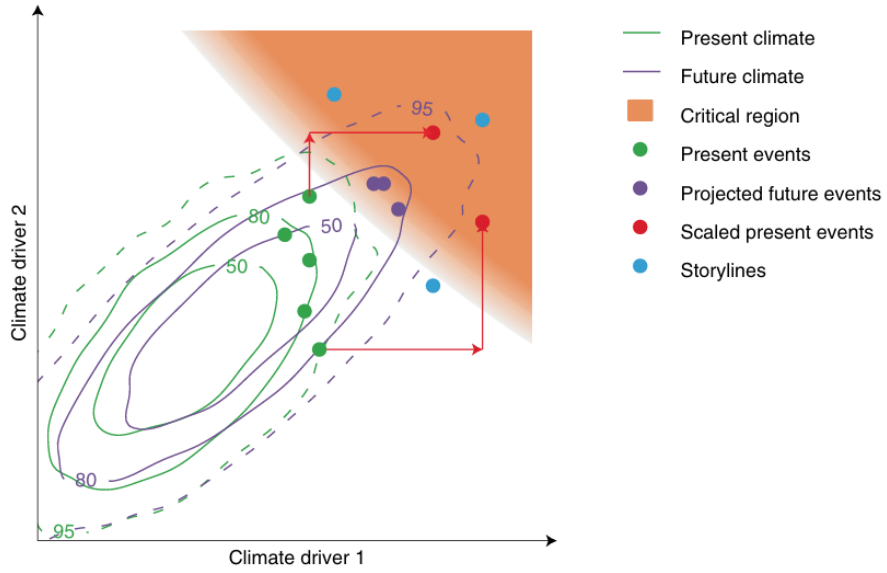

Figure 1.2: Illustration by Zscheischler et al. (2018) of different possibilities to simulate potentially critical compound events in the future climate. In the context of this research, the climate drivers are represented by TC-induced surge and wave.

By integrating both storminess changes and sea level rise (SLR), this study fills a critical gap in the current understanding of TC-induced flood hazard in the Sofala region. This approach offers a more comprehensive assessment of future coastal hazards at a regional scale by evaluating the individual and combined impacts of these evolving drivers, which have remained to be studied. As the dataset used, STORM-IBTrACS and STORM-CC are fully open source and available at a global extent, hence the methodology used in this study can also be replicated elsewhere where the TC-induced effect is abundant. Furthermore, by utilising a storyline approach, the findings will not only advance scientific knowledge but also effectively inform regional policy-making, providing essential insights for the development of adaptive coastal flood protection strategies and disaster risk management plans.

1.4. Research Questions

Building upon the identified research problem and objectives, this study formulates a set of research questions to guide the analysis. In essence, these questions consist of the quantification of the pro-

jected changes in TC-induced coastal hazards and assessing the relative contribution of storminess and SLR to future flood risks. A probabilistic-scaled future event framework combined with a storyline-based approach forms the basis for addressing these questions at a regional scale.

Main Research Question:

What are the projected changes in tropical cyclone (TC)-induced wind, surge, and wave extremes in near-future climate conditions, and what is their importance in future coastal flood hazard along the Sofala coast?

Objective A:
To quantify the change in tropical cyclone-induced storminess—wind, surge, and wave—at a regional scale under future climate scenarios.

1. What are the marginal changes in wind, wave, and surge hazards in terms of intensity and frequency?
2. What are the projected changes in joint wave–surge hazard under future climate conditions?

Objective B:
To assess the contribution of storminess changes, relative to SLR, to future TC-induced coastal flood hazard using a probabilistic-scaled future event and storyline-based approach.

1. To what extent do storminess changes amplify total water levels under future climate conditions, relative to sea level rise?
2. How does the inclusion of projected storminess change, and sea level rise modify the spatial patterns of flood extent and depth storyline-based event?

1.5. Research Scope

This study does not incorporate hydrodynamic model calibration and validation, as observation data is hardly available. Consequently, the focus lies not on the absolute accuracy of the simulated values, but rather on the relative shifts in patterns under near-future climate conditions. Moreover, as this study's foundation is based on the STORM-IBtrACS and STORM-CC datasets, the simulated climate change scenario and GCMS variations are limited to the HighRes-MIP CMIP6's GCMs used in STORM-CC under the SSP585 scenario. The 4 GCMs used were CMCC-CM2-VHR4 (Scoccimarro et al. 2017), EC-Earth3P-HR (E.-E.-Consortium 2018), HadGEM3-GC31-HM (Roberts 2017), and CNRM-CM6-1-HR (Voldoire 2019). Since these STORM datasets only involved materials for developing TC-induced wind fields, we exclude contributions from pluvial and fluvial flooding in this study. As the future scenario for HighRes-MIP is limited up to the year 2050, the future period is defined as the year 2015-2050 timespan, while the historical or baseline period is represented by the year 1980-2017, following the timeframe of STORM-CC and STORM-IBtrACS, respectively. Therefore, for the development of the TC Idai storyline, it is assumed that TC Idai belong to the baseline period instead. Lastly, in this study, only the first 5,000 years out of the total 10,000 years of synthetic tropical cyclone datasets in STORM-IBTrACS and STORM-CC are used, under the assumption that these 5,000 years are representative of the overall distribution, providing sufficient coverage for the analysis.

1.6. Thesis Outline

Chapter 2 elaborates on the geographic and hydromorphodynamic characteristics of the study area, reviewing relevant literature on the physics underlying TC in the study area and the underlying theoretical rationale behind the hydrodynamic and statistical models used in the methodology. Chapter 3 outlines the data sources and methods used to quantify changes in storminess and assess their impact on future coastal flood hazards. Chapter 4 presents the results of the analysis, while Chapter 5 discusses the implications and limitations of these results. Finally, Chapter 6 concludes the thesis by presenting key findings and recommendations for future research.

2

Literature Review and General Modelling Rationale

This chapter is divided into two parts: *1.)* a pure review of relevant literature, and *2.)* literature-aided modelling rationales. The first part provides a brief geographical and physical description of the study area (Section 2.1), followed by an overview of the physics behind tropical cyclone-induced wind, surge, and waves, including how these processes may evolve under future climate conditions (Section 2.2). The second part will look closely at the known options, descriptions, limitations, and the justification for the chosen TC modelling approach (Section 2.3) and statistical analysis procedure (Section 2.4). Detailed description of the data and the setup of the TC modelling approach, as well as the utilisation of the chosen statistical analysis procedure, will take place later in Chapter 3.

2.1. Study Area

2.1.1. Geographical Situation

Sofala Province (see Figure 2.1) is located in central-eastern Mozambique, bordered by Tete Province to the north, Zambezia to the northeast, Inhambane to the south, and Manica to the west. On the eastern boundary, this province is directly connected to the Mozambique Channel, part of the Indian Ocean that connects Southeast African countries with Madagascar. This channel brings warm current flowing southward through the channel until it eventually joins the Agulhas Current near South Africa's eastern shore (Britannica 2025). This province covers an area of approximately 68,018 square kilometres, featuring a diverse landscape that includes coastal lowlands, inland plains, and major river systems such as the Buzi, Save, and Púnguè rivers. The latter flows into the sea at the provincial capital, Beira. Just off the Sofala coast, including the deltas where these rivers end, is part of a larger area called Sofala Bay, host to rich marine fishery resources. This area is mostly characterised by extensive coastal wetland and mangrove forest (Deltares 2021). The northernmost coastal districts of this province are where Marromeu National Reserve is located, denoting Sofala's ecological and cultural significance. However, this reserve is listed as one of the African natural heritage sites that will become highly vulnerable to flooding and coastal erosion by the end of the century, according to the IPCC's Sixth Assessment Report in 2022, but only if climate change follows RCP 8.5 (Trisos et al. 2022).

The attached map (Figure 2.1) denoted Sofala's administrative boundaries, major towns, and physical features, with an inset showing its location within Mozambique. Administratively, Sofala is divided into 13 districts, with 9 of which are bordered by the Sofala Bay: (from south to north) Machanga, Divinhe, Sofala, Buzi, Beira, Dondo, Galinha, Inhaminga, and Marromeu. Beira, the provincial capital, is Mozambique's second-largest city and a key port, serving as an economic hub for the province, country and even neighbouring landlocked countries (Filipe et al. 2017). The map's colour gradient reflects population concentrations according to the World Pop dataset (CIESIN 2018), with the highest density exceeding 300 people per hectare found near the coast of Beira. This dense settlement stretches upstream, along the Pungwe River floodplain to the Dondo district. Moreover, rural districts, such as those near the coast of Buzi and Sofala districts, are more sparsely populated (CIESIN 2018). This demographic distribution underscores how dense Sofala's population mainly resides in the low-lying coastal area, potentially exposed to coastal-induced flooding and overflowing from the tidal-influenced

rivers.

2.1.2. Tropical Cyclone in Study Area

Mozambique is located relatively downstream of the TC tracks, with most of the historical TCs coming from the central South Indian Ocean, offshore of Madagascar's eastern coast. With an extensive range of latitudes, a large bay area primarily covering Sofala province, and the blocking effect of the island of Madagascar, the cyclone path affecting Mozambique is somewhat spatially variable (Matyas 2015). Still, the occurrences of cyclone landfalls (or at least passing very close) in any coastal location in Mozambique are calculated to be around 0.1 to 0.2 per year (Deltares 2021). These cyclones commonly occur from October to April during Mozambique's wet season. As shown in Figure 2.2, the yearly arrival rate of cyclones based on the IBTrACS dataset on Sofala's coast and down south to the Maputo province's coast is around 0.1. In contrast, just at the northern end of Sofala province, up to Mozambique's northernmost, the cyclone arrival rate are doubled to around 0.2.

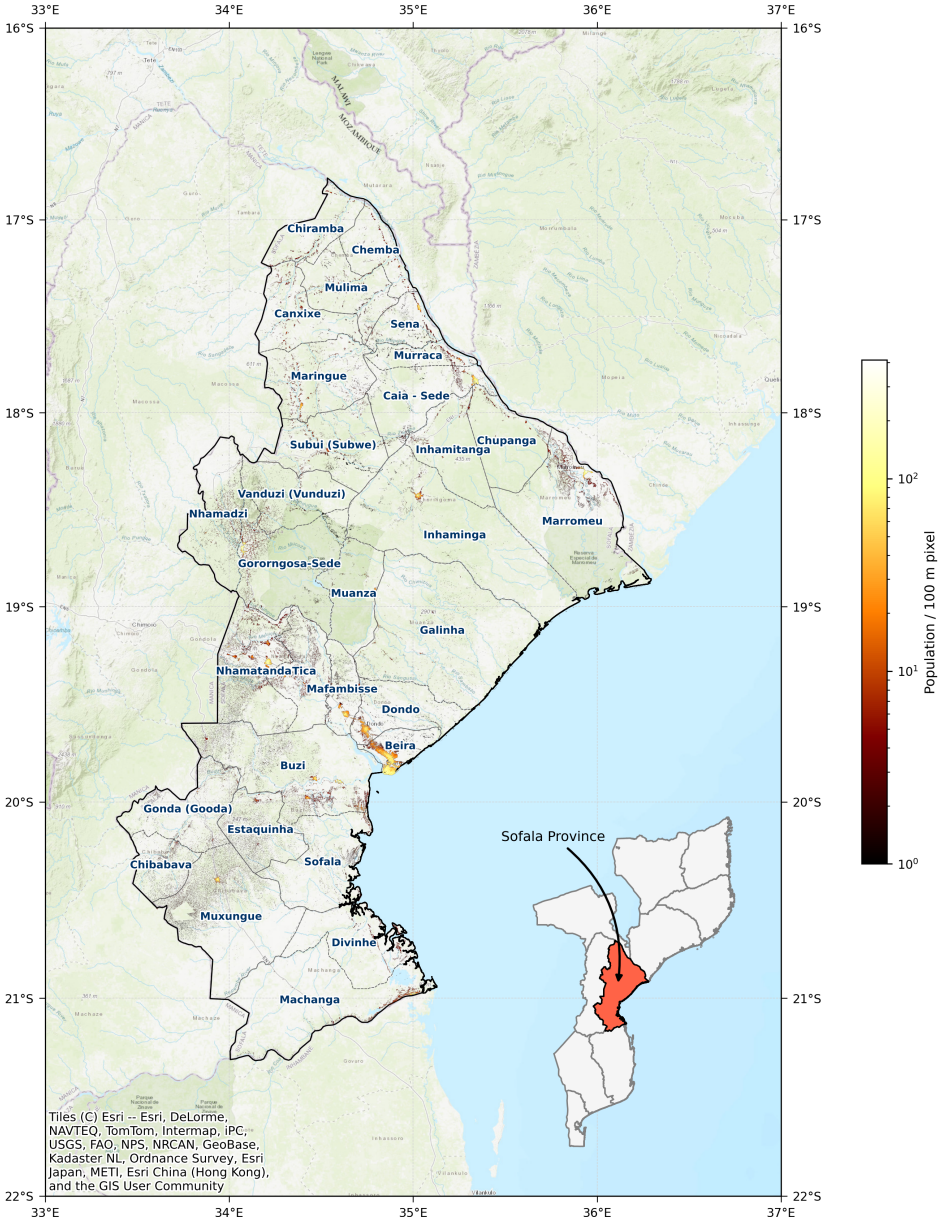

Figure 2.1: Sofala Province's geographical situation, administrative area, and population density based on World Pop dataset (CIESIN 2018)

Figure 2.3 shows historical TC tracks of the Catastrophe level of 1 or beyond (> 64 kts or 33 m/s) that made landfall in or passed very closely to Mozambique between 1970 and 2024. At the Sofala zoom view, we can see notable TC events such as TC Idai 2019 and TC Eloise 2021 that cause increased surge water levels and significant pluvial and fluvial inundation in the region (Eilander et al. 2023a). Notably, the Sofala province has experienced clustered cyclones, sequential TC events that occur very close in time, at least twice. Once in 1961/1962, Daizy and Gina, and in modern times, 2020/2021, Chalane and Eloise made landfall just three weeks apart. Still, these did not match the destruction Cyclone Idai caused, likely due to the relative storm weakness for the Daizy, Gina, and Chalane or timing during neap or low tides for Eloise (Ormondt et al. 2020). However, slight changes in cyclone path or timing might have resulted in significantly greater damage (Goulart et al. 2024; Goulart et al. 2025).

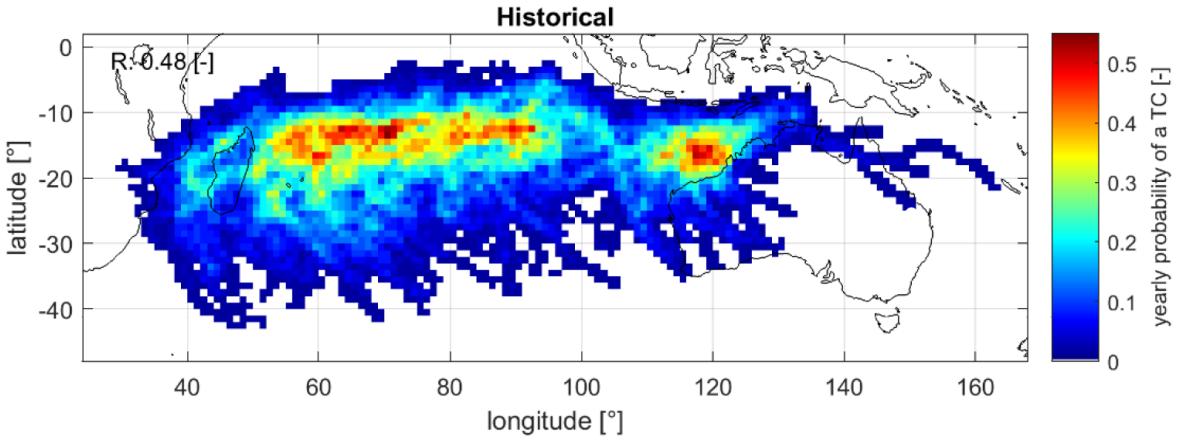

Figure 2.2: South Indian Basin's tropical cyclone yearly occurrence probability based on IBTrACS dataset. This figure is derived from Deltares (2021)

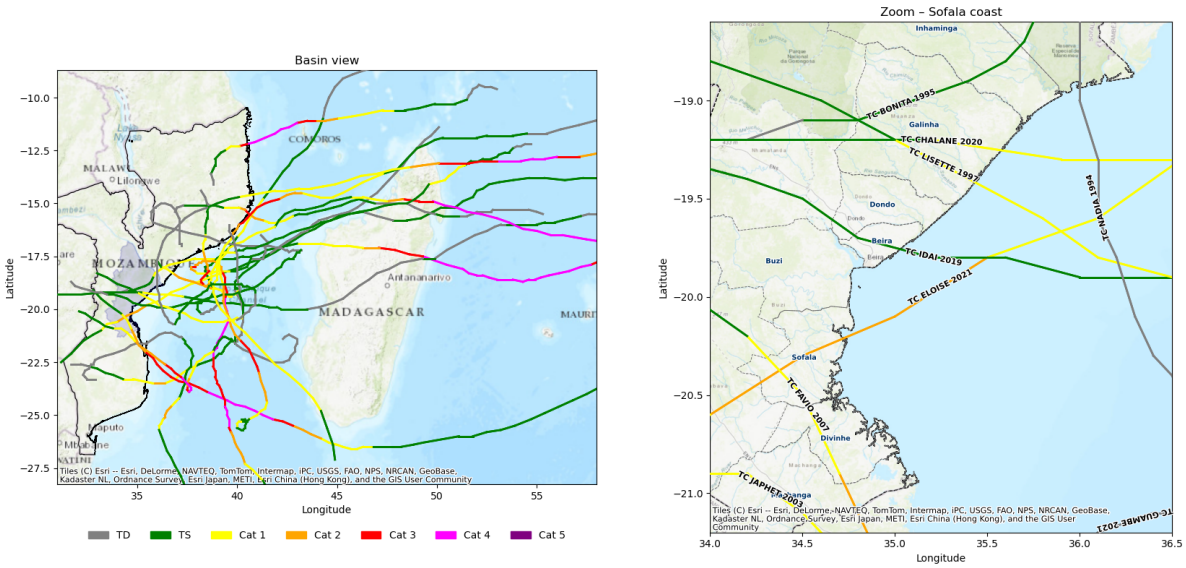

Figure 2.3: Historical TC tracks (1970-2023) of at least categorised as Catastrophic level 1 (> 64 kts or 33 m/s), that made landfall in Mozambique (left) and Sofala province specifically (right)

2.1.3. Tidal Condition

Figure 2.4a shows M2 tide magnitude and phase variability across the Mozambique channel based on the TPXO8.0 dataset. The M2 tidal phase indicates how the tide propagates from south to north in this stretch of coastline. It also becomes clear that the highest M2 tide is found around the Sofala Bay area,

with its peak just off Beira's coast. An IHO station is located just a little inside the mouth of the Pungwe River, near Beira Port. The tide time series constructed based on the tidal constituents at this station for the 1980-2017 period is shown in Figure 2.4b. It can be seen that the tide range in this location reaches more than 7 meters with a HAT of +3.81 m and LAT of -3.3 m, and MHWS as well as MLWS of around +2.9 m and -2.8 m, respectively. From a regional perspective, the tidal range along the coast of Sofala province is found to be at least three meters. Owing to this fact, the Sofala province's coast might also be classified as a hydrodynamically tide-dominated coast with a macro-tidal regime (Davis Jr. et al. 1984).

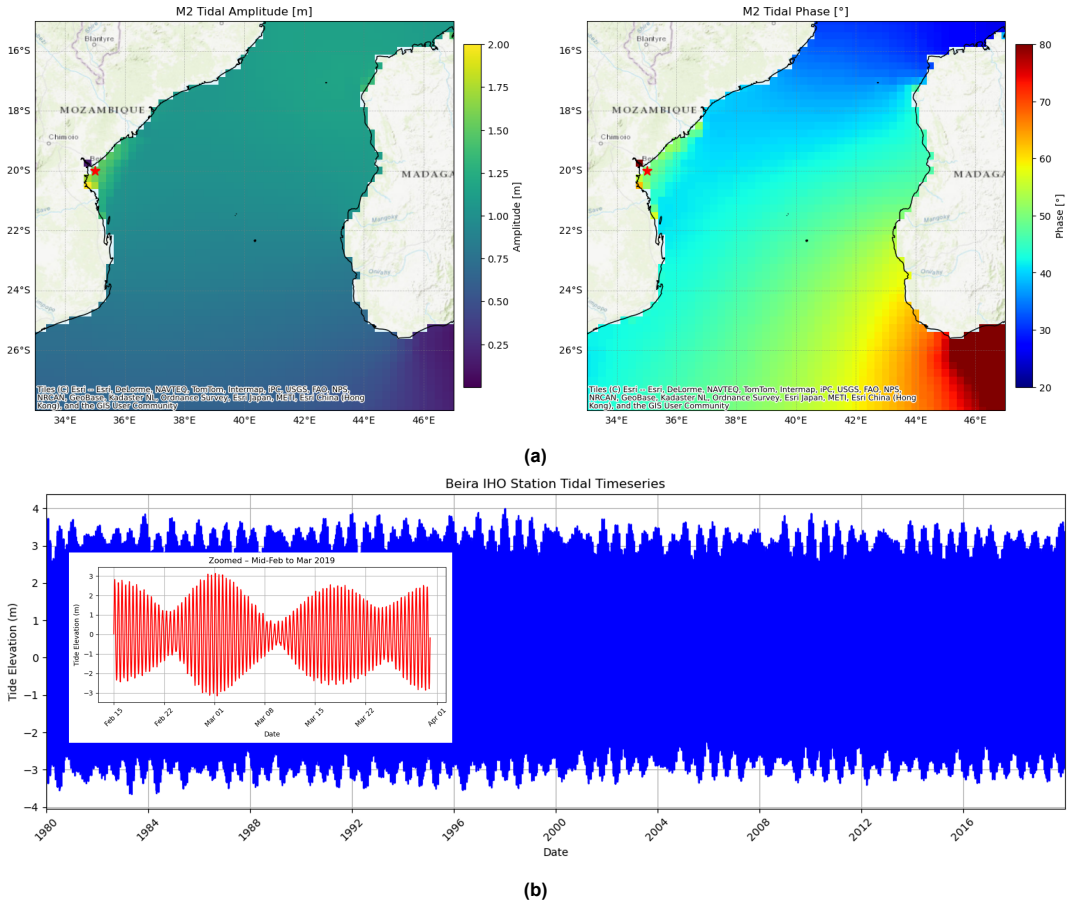

Figure 2.4: Tidal characteristics near Beira. (a) M2 tidal amplitude and phase based on TPXO8.0 (Egbert et al. 2002) tide models around the Mozambique channel. The red star indicated the IHO (International Hydrographic Organization) tide station location at Beira. (b) Constructed tide time series from 1980 to 2019, based on Beira IHO station's tidal constituents (International Hydrographic Organization 2024).

2.1.4. Coastal Characteristic

The characteristic of the bathymetry adjacent to Sofala's concave-shaped coastline is characterised by a very wide (up to 150 km) and shallow continental shelf, as shown in Figure 2.5. Especially near Beira, the sediment deposition carried by the Pungwe and Buzi rivers is evident through the shallow delta protrusion near the river mouth. This then gently slopes into deeper shelf regions, indicating active sediment delivery and morphological shaping by marine and riverine processes. On the inland part, we can see how the coastal area in Sofala province is mainly dominated by a relatively flat and wide low-lying topography, with the majority of elevation below +10 m, before a sudden transition to +30 m. With this topography and bathymetry, it is best to characterise this coast as a trailing edge, or more specifically, a neo-trailing edge coast (Inman et al. 1971). This type of coast, also found on the west coast of Africa, Greenland, and part of Australia, is characterised by its wide and shallow continental shelf, as well as rich sediment deposition, which produces less pronounced wave energy and high

surge amplification (elaboration on this physics is shown later in Subsection 2.2.2.

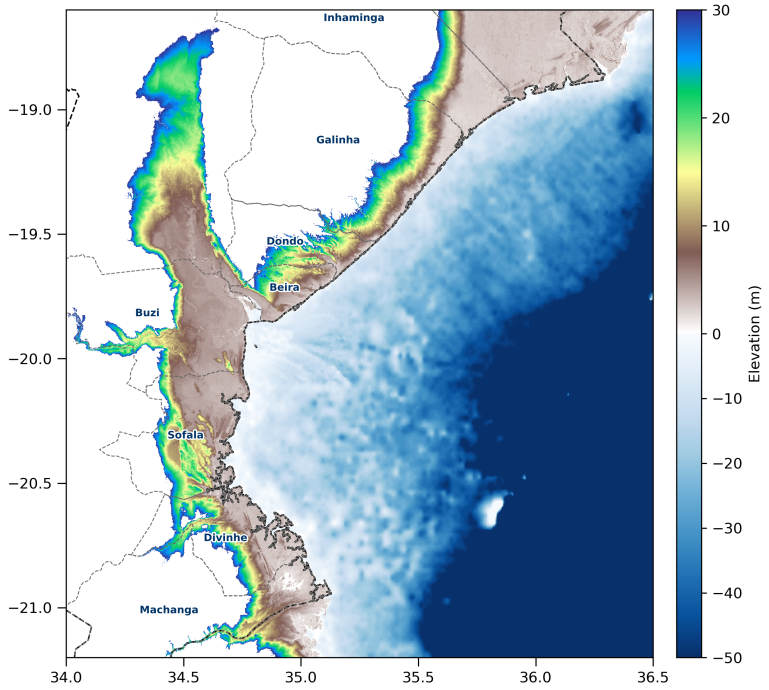

Figure 2.5: Sofala Province's topography (up to +30 m) and bathymetry (down to -50 m) based on Delta-DTM (Pronk et al. 2024) and GEBCO2024 (GEBCO Compilation Group 2024) respectively

Going deeper into a finer scale, Figure 2.6 shows spatial variability of nearshore slope (from coastline to the depth of closure) and backshore slope (from coastline to first dune) in the region. The nearshore slope of the study area becomes progressively steeper towards the north, increasing by approximately two orders of magnitude, from values on the order of 10^{-4} to 10^{-2}. This pattern denoted an extensive surf zone along the coast. In contrast, the backshore slope seems well spread out (mostly below 0.1 slope) with a notable concentration of higher slopes near the port of Beira, close to the Púnguè River mouth. This indicates that Sofala's coastal area is primarily characterised by an exposed morphological setting, lacking natural protective features such as dunes.

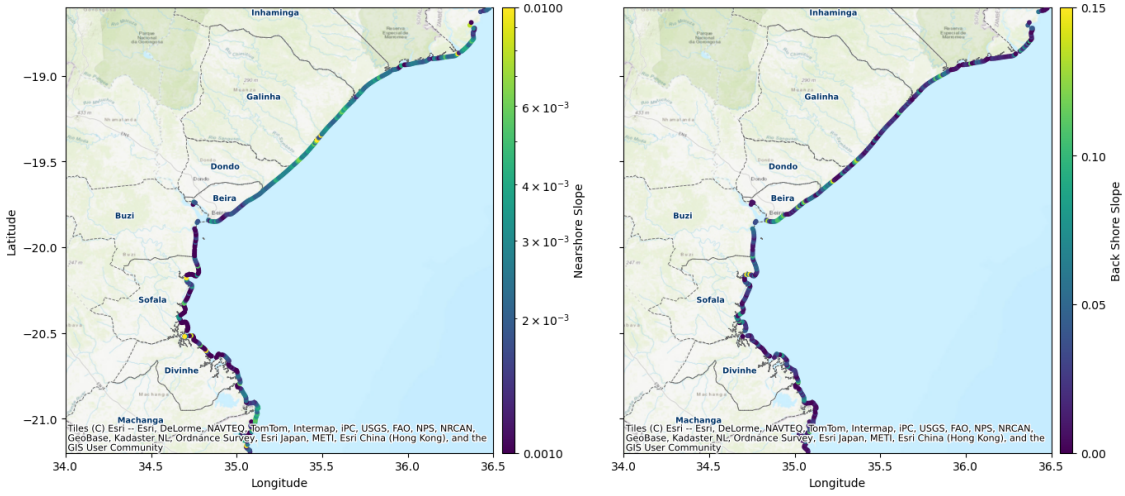

Figure 2.6: Sofala Province's coastal nearshore (left) and backshore (right) slope based on Delta-DTM (Pronk et al. 2024) and GEBCO2024 (GEBCO Compilation Group 2024) respectively, as derived from Global Coastal Characteristic Database (Athanasiou et al. 2024)

2.2. Physics Behind Tropical Cyclone-Induced Coastal Flood Drivers

This section elaborates on the physics behind the development of tropical cyclones, followed by an explanation of how these tropical cyclones drive surge and waves. Additionally, the physics behind the evolution of TC under future climate conditions will also be briefly explored. Special attention will be given to its behaviour in the context of the Sofala region's physical and geographical characteristics, as explained earlier.

2.2.1. TC development and movement

Before understanding how surges and waves are generated by a TC, first, the physics of how a TC is developed and, later, the transport are briefly explored. Several key atmospheric and oceanic conditions are responsible for developing tropical cyclones. Sea surface temperatures greater than 26°C and proximity to the band of low pressure, such as the Intertropical Convergence Zone (ITCZ), or its regional version, e.g., the South Indian Convergence Zones, provide the energy and atmospheric vertical motion necessary for cyclogenesis to occur (Holland 1997; Vincent et al. 2011). After being lifted, a strong Coriolis force will create the cyclonic rotation. This Coriolis movement guides the rotating direction of the TC; clockwise in the Southern Hemisphere and counterclockwise in the Northern Hemisphere. As this force is dependent on the latitude, most TCs form between absolute values of 5° and 25° latitude, where the Coriolis force is strong enough; near the Equator, where the force is weak, TC formation is inhibited (Gray 1998). Even with greater Coriolis forcing at higher latitudes, cooler ocean temperatures and distance from the global band of low pressure usually inhibit further development beyond 25° latitude (Camargo et al. 2007).

Once a TC forms, large-scale atmospheric circulation patterns in its region play a significant role in steering the path and translation speed. Tropical cyclones in the South-West Indian Ocean (SWIO) typically develop between 10°S and 20°S and are first steered westward by the easterly trade winds of the Mascarene High—a quasi-permanent subtropical high-pressure belt east-southeast of Madagascar (Bessafi et al. 2006). Whether the cyclone remains on this westward path or turns southward depends on the location and strength of the subtropical ridge. Once the ridge is weakened or displaced, commonly due to a trough in the jet stream, cyclones may recurve poleward into the open ocean. However, when the ridge is zonally extended and strong, TCs will keep going westward, making landfall in Madagascar or southeast Africa, particularly Mozambique (Matyas 2015). This process is very well illustrated in Figure 2.7. In addition, the Mozambique Channel provides extra steering challenges through local circulation, sea surface temperature gradients, and topography, sometimes allowing cyclones to re-intensify or change course after initial landfall, such as Cyclone Freddy (2023) (Perry et al. 2024; Pall et al. 2024).

Beyond large-scale steering, physical geography also influences landfall patterns. Because westward TC motion demands continuous energy input from the ocean–atmosphere system, cyclones do not always reach deeper into the basin. This geographic filtering effect is especially apparent in the SWIO, where protruding coastal features such as capes, deltas, or islands act as the first intercept points for incoming systems (Needham et al. 2015). As a result, landmasses that are more exposed to the open ocean, such as Madagascar's eastern coast and northern Mozambique, experience landfall more frequently (as seen in Figure 2.3). This explains why the concave Sofala bay area is less likely to be struck unless the storm has high translational momentum or unusually strong steering currents, producing a lower yearly arrival rate than its northern neighbouring convex coastline, as seen in Figure 2.2.

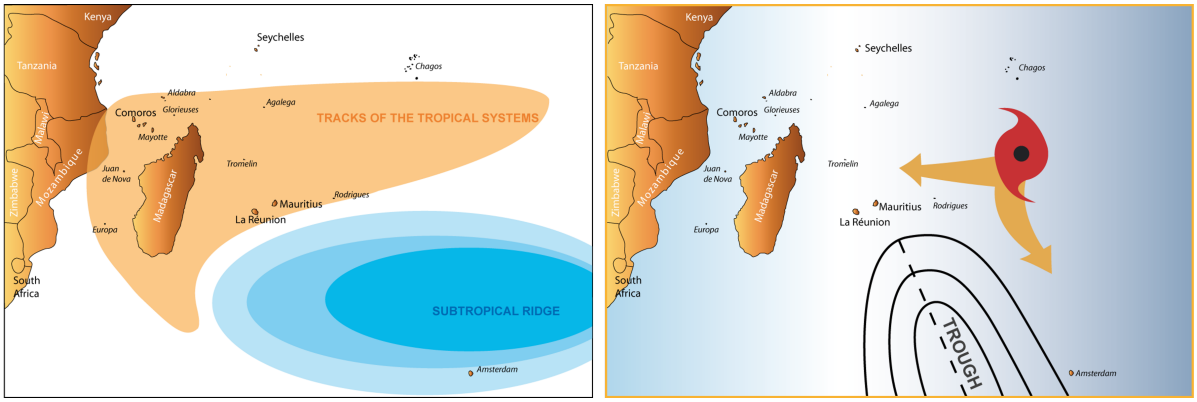

Figure 2.7: The Left figure shows the zone of the tropical system in the South Indian Ocean basin, and where the subtropical ridge supplies winds to translate the tropical cyclone track westward. The right figure illustrates how the TC track might shift poleward as the ridge is weakened due to a trough in the ridge's jet stream. (Météo-France 2025)

Tropical cyclone track genesis and movement data have been documented worldwide in the past decades and archived in the International Best Track Archive for Climate Stewardship (IBTrACS; Knapp et al. (2010)). This data typically includes time-stamped reports of cyclone eye position and best-track maximum wind speed estimates. Cyclonic systems are typically referred to in terms of tropical depression, tropical storm, or tropical cyclone status, based on their one-minute mean surface wind speed. To further describe the cyclones' strength, the Saffir–Simpson scale is typically employed, categorising tropical cyclones in five classes on the basis of maximum sustained winds. Whereas this categorisation is well established worldwide, it is recognised that in different regions, various regional scales might be applied. Table 2.1 presents the Saffir–Simpson scale, corresponding wind speed thresholds, and typical associated wind damages to buildings, electricity and utilities.

Table 2.1: Classification of tropical depressions, storms, and cyclones according to wind speeds based on the Saffir-Simpson scale, and their associated potential impacts to homes, buildings, electricity and utilities (NOAA 2019).

Storm class	Wind speed m/s (km/h)	Consequences
Tropical depression	<17 (<62)	-
Tropical storm	18–32 (63–118)	-
TC category 1	33–42 (119–153)	Very dangerous winds will produce some damage
TC category 2	43–49 (154–177)	Extremely dangerous winds will cause extensive damage
TC category 3	50–58 (178–208)	Devastating damage will occur
TC category 4	58–70 (208–251)	Catastrophic damage will occur
TC category 5	>70 (>252)	Catastrophic damage will occur

2.2.2. TC-induced Surge

Generation and intensification of tropical cyclone storm surges are regulated by a mixture of TC-induced dynamic meteorological forcing and coastal environments, either at deep water or shallow water (see Figure 2.8). With cyclones approaching the coast, storm surge amplitude is regulated predominantly by wind stress over the sea surface, which exerts a quadratically growing force with increasing wind speed. This mechanism is said to produce 80–85% of the total surge height for the majority of events (Kurian et al. 2009). However, surge behaviour is also affected by variables such as central pressure, forward speed, cyclone radius, angle of approach, and coastal geometry (Harris 1963; Rego et al. 2009; Wang et al. 2021). Wind speed profiles pre-landfall may exert a greater influence on peak surge than wind speed at landfall, especially for storms of long duration (Needham et al. 2015). Shallow bathymetry greatly enhances the development of surge because the slower-moving water over shallow shelves cannot spread out and thus piles up along the coast (Rappaport et al. 1995). Deltaic environments and estuary systems, like those in Sofala Bay (see Figure 2.5) and the Mississippi River delta, are most vulnerable to high-magnitude surges caused by fine sediment deposits, wide continental shelves, and geographical borders.

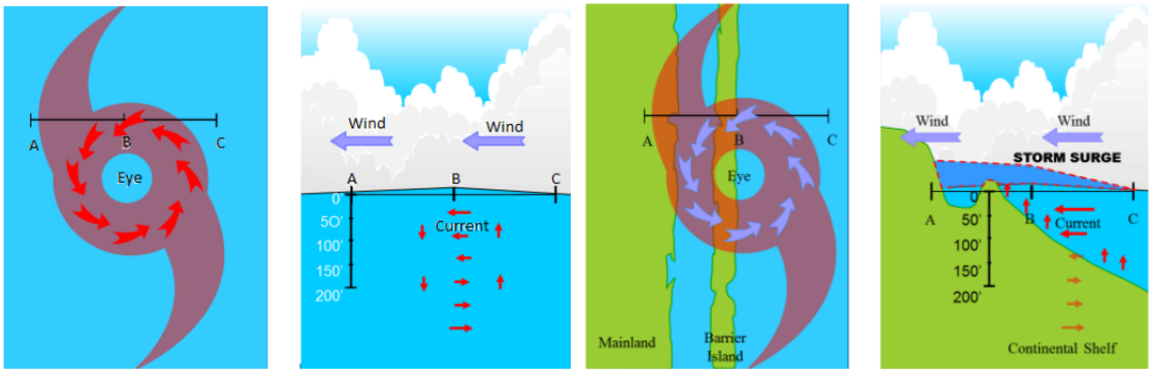

Figure 2.8: TC-induced storm surge generation and transformation in deep water (a) and as it reaches shallow water (b) (NOAA 2008)

As an initial approximation, a basic linear steady-state equation can be used to estimate how wind-driven storm surges are influenced by water depth and the width of the continental shelf (Resio et al. 2008):

$$\zeta \propto \left(\frac{\tau_s}{\rho g h}\right) W \tag{2.1}$$

where ζ is the surge height at the coast, τ_s the wind stress, ρ the density of seawater, g gravitational acceleration, h the water depth, and W the shelf width. This illustrates that wider and shallower shelves generate greater surge heights than steeper, narrower ones. In the real world, the geometric complexity of the coastal zone—e.g., river deltas, barrier islands, reef channels, and artificial features such as levees—imposes highly variable local surge behaviour. The importance of correctly resolving bathymetric and geomorphic variability in storm surge modelling is thus strongly illustrated in complex environments like Mozambique's Sofala coastline, where shallow embayments and estuarine networks would have a deep effect on cyclone-induced surge impacts.

2.2.3. TC-induced Wave

The elaboration of the TC-induced wave in this subsection is anchored on the schematic diagram by (Young 2017) presented in Figure 2.9. Please note that this illustration is based on TC in the Northern Hemisphere, and hence the TC anti-clockwise rotation. The physical mechanisms driving wave generation and asymmetry in such storms are summarised in the following discussion.

Firstly, TC winds force waves in a highly asymmetric way and in a completely different pattern than the wind itself (Uhlhorn et al. 2014). Because the cyclonic circulation of the storm translates (moves), the right-hand (ahead) side winds of the track blow in nearly the same direction as the TC motion, so the newly formed waves are subject to continuous strong forcing for an "extended" or even "trapped" fetch (Bowyer et al. 2005). This allows energy to build up for considerably longer than in ordinary fetch-limited development, generating wave heights and a JONSWAP-type spectrum whose most important frequency continuously changes downwards under the effect of nonlinear wave–wave interactions (Young 1998; Young 2006). At the left (rear) side of the storm, winds are counter to the moving direction; the effective fetch is short, waves quickly outrun the storm, and heights are lower. The asymmetry of effective fetch consequently produces a wave field wider than, and more asymmetric than, the accompanying wind vortex (Young 2017).

The dashed-circle drawing in Figure 2.9 illustrates this physics (Young 2017): the concentric rings represent increasing distance from the tranquil eye, and the thick curved arrows represent the anticlockwise wind field. Grey lobes mark the zones of peak winds just outside the eyewall. In the front-right quadrant, waves thus formed travel with the storm, possess the largest fetch, and propagate outward as long-period swell (black straight arrows). In contrast, waves that form in the rear-left quadrant travel opposite to the direction of the storm, exit the wind area early, and therefore are shorter and steeper.

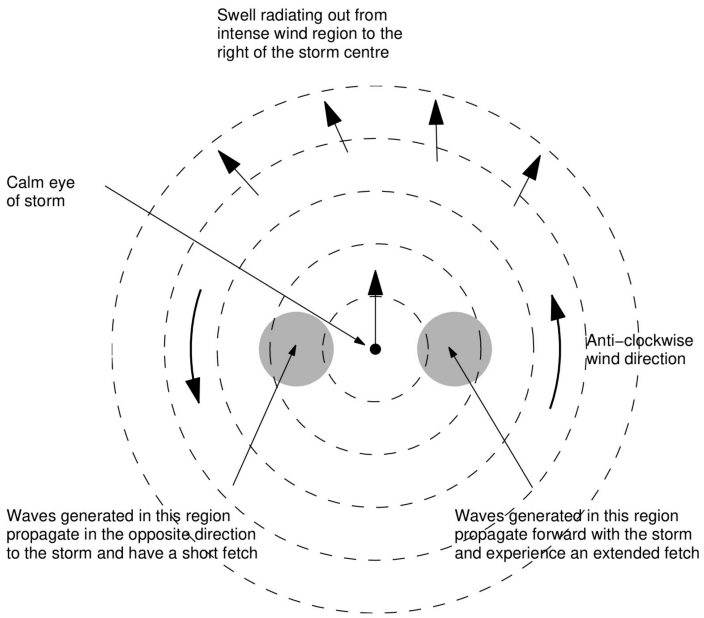

Figure 2.9: A schematic diagram by Young (2017) depicting wave generation within a tropical cyclone in the northern hemisphere that is translating. The arrow at the center of the storm indicates that the tropical cyclone is translating "up the page". The wave field is distinguished by (i) swell ahead of the storm, radiating out from the intense wind region to the right of the storm center, and (ii) significant asymmetry caused by higher winds and an extended translating fetch to the right of the storm center.

The result is a highly directional spectrum with strong right-of-track swell and a strong left–right asymmetry that must be resolved by any surge or coastal-impact model.

2.2.4. Tropical Cyclone under Climate Change

Though a theory that predicts the number of tropical cyclones (TCs) based on climate is yet to be constructed, a number of known physical processes describe how a warming climate can lead to increased or decreased TC numbers and intensity (Walsh et al. 2016). Increased sea-surface temperatures, along with a colder tropical tropopause, amplify the reservoir of thermodynamic energy available to develop storms, thereby raising the theoretical limit of cyclone wind speed (Vecchi et al. 2007; Emanuel et al. 2013). Conversely, the majority of greenhouse-warming experiments conducted with climate models anticipate a modest reduction in the mean upward mass flux in the tropics; this reduction in ambient ascent decreases the likelihood that low-level disturbances will mature into TC vortices (Walsh et al. 2015). Climate change also changes environmental wind shear and mid-tropospheric humidity: higher shear or drier mid-levels ventilate nascent vortices more effectively, preventing their development from disorganised convection to full-blown cyclones (Kim et al. 2014). Collectively, these mechanisms create a global-scale vision of the future in which the number of TCs overall may not actually increase, and might actually decrease, while the proportion of the most intense, highest-energy storms will rise.

A study by Bloemendaal et al. (2022) utilised HighResMIP in the STORM algorithm to predict global changes in TC genesis (1980-2017 versus 2015-2050). As shown in Figure 2.10, across the entire South Indian basin, it is expected that the average TC per year will decrease from 12.3 (based on IBTrACS) to 10.4-11.7 (with CMCC being the lowest and CNRM being the highest), with a predicted increase in arrival rate of TC category two or above, and a decrease arrival on category one and tropical storm. Looking into a finer regional scale, recent-past HighResMIP high-resolution simulations indicate that future tropical-cyclone activity in the South-West Indian Ocean will increasingly be spatially focused, intensity-wise, in the Mozambique Channel (Pall et al. 2024). Across the multi-model ensemble, tropical-storm and cyclone numbers, and basin-wide accumulated-cyclone energy decrease for 2020-2050 versus 1980-2010, but models all show an east-to-west track-density shift: storms that historically peaked east of Madagascar move westward, causing local track-density increases and 99th-percentile near-surface wind increases in the Mozambique Channel (Pall et al. 2024). This trend

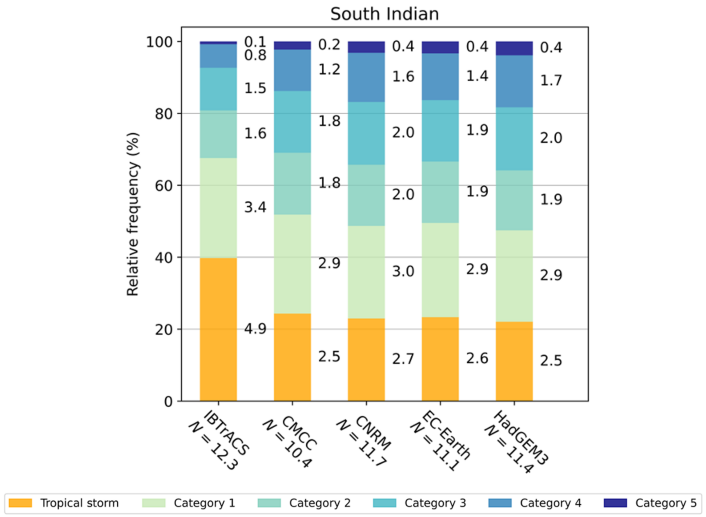

Figure 2.10: Figure by Bloemendaal et al. (2022). Each of the four HighResMIP GCMs' relative and absolute frequency of the various tropical storm (TC) categories (categories 1 through 5) for 10,000 years of baseline climate STORM-B data and 10,000 years of future-climate STORM-C data. The height of the colored bar chart indicates relative numbers, while the right side of each colored bar chart shows the absolute frequency (as an average per year) for each TC category and input dataset. In the x axis label, N stands for the total number of cyclone formations.

implies that, while Mozambique may get fewer cyclones in total, the potential for direct interactions (and associated high winds, waves and surge) within the Channel is projected to grow, underscoring the role of region-specific coastal-risk analyses.

2.3. Rationale of TC-Induced Wind, Wave and Surge Model

This section will elaborate on the state-of-the-art modelling steps of TC-induced hydrodynamics, mainly to produce surge and wave components. Known options, descriptions, and limitations are discussed before a specific procedure is decided on, along with its justification.

2.3.1. Synthetic tropical cyclone tracks

Tropical cyclone track records, such as IBTrACS, usually consist of parameters such as eye coordinates, maximum sustained winds, pressure drops, TC radius, etc (Knapp et al. 2010). These track records are typically very limited regarding the number of events per location due to their low yearly arrival rate and scarce recorded data. This limitation hinders risk analysis or engineering design, which typically requires an extensive dataset to derive an extreme value, either based on a non-parametric empirical approach or a parametric distribution fitting (Nederhoff et al. 2021). To address this issue, the current state of the art usually involves generating synthetic cyclones by conducting a Monte Carlo random sampling from probability distributions based on historical TC characteristics (James et al. 2005). This approach allows thousands of synthetic years to be modelled under the assumption that each event is an independent realisation of a common stochastic process, thus enabling estimation of extreme TC conditions for long (or longer) return periods.

One instance of applying this fully probabilistic approach is presented by Bloemendaal et al. (2020a), the STORM dataset (see Figure 2.11), which is the backbone of this study (elaboration on this dataset will take place in Section 3.1.1). Other notable variations of this approach, which incorporate explicit dynamical simulations in a statistical-dynamical framework, are the MIT model (Emanuel et al. 2006; Emanuel 2008) and the Columbia HAZard model (CHAZ) (Lee et al. 2018). Aside from using random seeding techniques, the similarity between these three datasets is also the use of the ERA5 climate dataset, either directly, as in STORM, or undergoing a physical TC and large-scale environment variables relationship model first, as in the MIT and CHAZ models (Meiler et al. 2022). By the time this study is written, these three datasets are the only ones that produce synthetic tracks for both historical and future climates by applying the variables from GCMs. However, since the STORM dataset provides

both fully open-source code and datasets and is still undergoing constant update and refinement, this study focuses only on using this dataset for general applicability. Detailed description on this dataset is presented in Subsection 3.1.1.

2.3.2. Spatial tropical cyclone wind field

A hydrodynamic numerical model, either wave or flow, usually requires a temporal and spatially variable wind time series as input. Since track datasets like IBTrACS or synthetic datasets like STORM include only limited storm structure data (the cyclone track, central pressure, maximum wind speed, and the radius of maximum winds), parametric wind field models are typically utilised to infer the full spatial wind field. Kinematic wind analysis approaches, steady-state slab Planetary Boundary Layer models, a mix of both, or mesoscale weather models are some of the complex and computationally demanding techniques that have been developed to predict the spatial wind field (Cardone et al. 2013). Still, parametric models such as *Holland1980* (Holland 1980) and *Holland2010* (Holland et al. 2010), remain the most common approach used due to their easy applicability and less demanding variable input. These two models are founded on an axisymmetric cyclone framework derived from modifications of the Rankine combined vortex profile, where wind speeds increase with decreasing pressure toward a maximum at the eyewall, then decline sharply toward the calm centre of the eye and more gradually toward the outer region, following the underlying exponential pressure gradient. Holland1980 requires three inputs: maximum wind speed (Vmax), central pressure (p), and the radius of maximum winds (Rmax), while Holland2010 requires additional wind radii (e.g. R35, R64, R100) to yield more precise profiles.

Actual TCs are not symmetric, however, such as what is previously explained in Subsection 2.2.3, and their asymmetry depends on a number of factors beyond storm motion (Knaff et al. 2003). The Holland model does generate some asymmetry by incorporating a fraction of the translational motion, but studies such as Lin et al. (2012) recommend altering this input, taking 55% of the motion vector and rotating it 20° counter-clockwise, for more realistic winds. Additionally, an inflow angle of 22.6° (Zhang et al. 2012) is typically included to model the inward spiralling of winds. Although the symmetry assumption has little effect on peak surge near the eyewall, it can lead to an underestimation of surge impacts at greater distances from the storm centre (Emanuel et al. 2011; Lin et al. 2012). Although more complex representations of the winds are available to correct for this (Chavas et al. 2015), they cannot appropriately be introduced here since the STORM dataset is stylised and lacks the structural detail to make such refinements worthwhile. That being said, the Holland1980 is the only feasible approach that can be used alongside STORM. An instance of the Holland1980 application for TC Idai is shown in Figure 2.12. The pressure and wind field based on Holland1980 model are given by:

$$P(r) = P_c + \Delta P \exp\left[-\left(R_m/r\right)^B\right] \tag{2.2}$$

$$V(r) = \sqrt{\left(R_m/r\right)^B V_{\max}^2 \exp\left(1 - \left(R_m/r\right)^B + r^2 f^2/4\right)} - rf/2 \tag{2.3}$$

Where $P(r)$ represents the atmospheric pressure at a radial distance r, $\Delta P = P_n - P_c$ denotes the pressure difference, with P_c as the cyclone's central pressure, P_n as the ambient or environmental pressure, $V_{\max}$ denotes the maximum wind speed, and f represents the Coriolis parameter. R_m refers to the radius of maximum wind (RMW), and B is the hurricane's shape parameter, which may be derived from empirical formulas or assumed constant. In this study, the values used are $P_n = 1013.25$ mbar and $B = 1.563$. Given the tropical cyclone parameters ΔP and R_m, the corresponding wind and pressure fields are computed and applied using a polar grid resembling a 'spiderweb' structure.

2.3.3. Hydrodynamic model

There is a range of options in simulating the hydrodynamics of TC-induced surge and wave, starting from a parametric approach: e.g., a parametric TC surge model by Jakobsen et al. (2004) or a parametric TC ocean wave model by Grossmann-Matheson et al. (2025), a data-driven approach (Wei et al. 2020; Lee et al. 2021), or a conventional numerical hydrodynamic model. Unlike in deep-water areas,

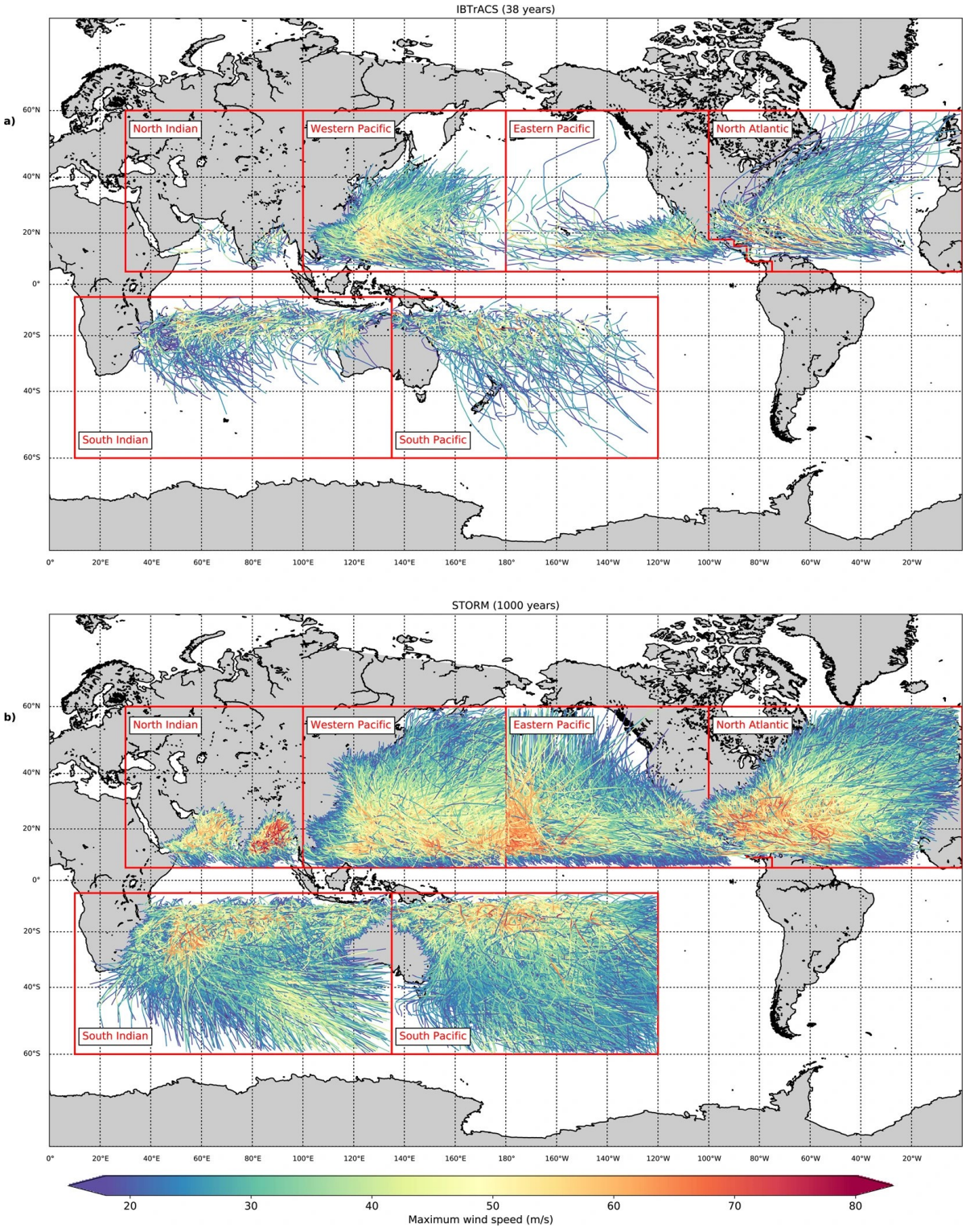

Figure 2.11: From Bloemendaal et al. (2020b); Overview of tropical cyclone tracks in IBTrACS and the STORM dataset. The top panel represents 38 years (1980–2018) of tracks in the IBTrACS dataset (a), and the bottom panel represents a random period of 1,000 years of tropical cyclone tracks in the STORM dataset (b). Colours indicate the maximum wind speed of the tropical cyclone.

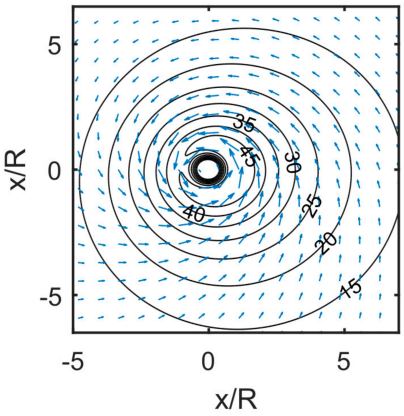

Figure 2.12: Visualisation by (Young 2017) of Holland1980 spatial wind field model. The contour indicates wind speed, while the blue arrow indicates the wind vector direction.

nearshore conditions have complex bathymetry and non-linear processes like shallow water wave dispersion. This makes general parametric models and data-driven methods less reliable, necessitating the use of a conventional numerical hydrodynamic model. For the hydrodynamic numerical model, a distinction can be made between whether coupled wave-water level non-linear interaction is to be simulated explicitly (e.g., coupled Delft3D-SWAN, or ADCIRC-SWAN) or separately. By coupling the wave and flow models, wave setup can be calculated dynamically; ignoring these processes might lead to an underestimation of the water level. The magnitude of wave setup is highly sensitive to the coastal characteristics of the study area, especially to topography and bathymetry conditions. Lin et al. (2012) demonstrated that in New York harbour, the effect of wave setup only amounted to 1.5% of surge. In contrast, at the coast of Beira, a study by Deltares (2021) reveals that the relative contribution of wave setup can be around 20-30% of non-tidal residual.

Accuracy, however, is not the only constraint on whether wave setup needs to be modelled explicitly. The computational demand of coupling the conventional spectral wave model into a flow model is said to increase computational time exponentially (Lin et al. 2012). On the other hand, resorting to a simplified empirical relation of wave setup, such as 0.2 *Hs* (USACE 2002) or (Stockdon et al. 2006), is often proven to inaccurately represent the water level at the coast (Leijnse et al. 2025). This is especially challenging for studies that rely on simulating thousands of synthetic events. In this research, such simulations form the core methodology used to achieve Objective A. Thus, a computationally feasible alternative approach to understand the change in TC-induced surge and wave is to focus on the significant wave height itself rather than the wave-induced water level component. This approach is previously displayed in Leijnse et al. (2022) and Marcos et al. (2019), which models TC-induced water level and spectral wave evolution separately, taking a deep water wave observation location to extract the wave height time series, and continues with statistical analysis to visualize the changes in extreme tail distribution under future climate condition. However, since this computational limitation is less of a hindrance for the storyline approach in Objective B, the coupled wave-water level dynamics will be simulated explicitly (more detail on this is presented in the Methodology section). For simulating surge and wave to achieve objective A, Delft3D-FM and HurryWave are used. Meanwhile, storyline scenarios will be simulated using a coupled SFINCS-Snapwave model. A brief description of these models is presented below:

Delft3D-FM

The Delft3D-Flexible Mesh is a model system that is versatile and advanced enough to simulate the complex dynamics of tropical cyclones, tsunamis, and storm surges. Delft3D-FM is based on the Navier–Stokes equations for incompressible flow with 2D (depth-averaged) and 3D formulations on the nonlinear shallow water approximation (Kernkamp et al. 2011). The full model implemented in Delft3D-FM comprises a comprehensive set of partial differential equations covering processes such as hydrodynamics, matter transport, 3D flow modelling, heat transfer, wind forcing, hydraulic structures, bedforms, and vegetation dynamics. Depending on the case study, certain processes may be

excluded to better suit specific conditions and to reduce computational costs. In this thesis, the model configuration focuses on 2D hydrodynamics and wind forcing.

To accurately resolve hydrodynamic equations in topographically complex areas, while maintaining computational efficiency, it is sometimes desirable to refine the computational grid locally. Delft3D FM enables this by allowing the use of unstructured grids and automatically generating a refinement degree based on the bathymetry depth, based on user-defined largest and smallest resolutions (Kernkamp et al. 2011). To make the computation even more efficient, Delft3D-FM also facilitates multiple processing (Message Passing Interface; MPI), in which computation can be parallelly divided over multiple cores. This model has proven its capability to accurately and efficiently produce TC-induced surges based on thousands of years of TC dataset at a large spatial scale, for the East Coast of Africa (Benito et al. 2024) or even a global scale Dullaart et al. (2021).

Hurrywave

HurryWave is a phase-averaged spectral wave model designed with an emphasis on basin-scale, hurricane-driven sea states (Deltares 2024b). As such, this model is developed with the sole purpose of prioritising computational speed through a reduced-complexity formulation. It is based on the same wave–action formulation as in other current models such as Wave Watch III (Tolman 2009) and SWAN (Booij et al. 1999), but employs an explicit first-order upwind discretisation with an emphasis on deep-water applications. The wave action balances solved by HurryWave are as follows:

$$\frac{\partial N(\sigma,\theta)}{\partial t} + \nabla\left[c_g N(\sigma,\theta)\right] + \frac{\partial c_g N(\sigma,\theta)}{\partial \sigma} + \frac{\partial c_\theta N(\sigma,\theta)}{\partial \theta} = \frac{S_{\text{wind}}}{\sigma} + \frac{S_{\text{diss.}}}{\sigma} + \frac{S_{nl4}}{\sigma} \tag{2.4}$$

The model advances the wave-action density $N = E/\sigma$ (E is the wave energy, σ is the radial frequency) forward in time and geographic, frequency, and directional space by integrating the action-balance equation, in which advection by the group velocity c_g and refraction by the directional celerity c_θ are balanced against source and sink processes. These are wind input (S_{wind}), dissipation (S_{diss}) and non-linear quadruplet interactions (S_{nl4}); the triad interactions that dominate in shallow water and any interaction with currents are deliberately omitted in the interests of efficiency. Although not always written explicitly, the wave-action density N is a function of time, and thus its partial derivative with respect to time reflects its temporal evolution under the influence of these physical processes.

Several physical processes are therefore unresolved. Water levels are assumed spatially uniform and constant, which is a reasonable simplification for the intended deep-water application. On the other hand, it necessitates bed-level corrections when the model is applied in nearshore applications where water-level gradients matter. Similarly, the absence of a wave–current interaction module precludes simulations over spatially inhomogeneous current fields. Finally, it is crucial to note that HurryWave is only appropriate for time-varying problems (non-stationary model). In its validation cases, HurryWave has demonstrated its capability to produce accurate model predictions when compared against wave buoy measurements for the Hurricane Idalia and Hurricane Fiona cases (Deltares 2024b).

SFINCS-Snapwave

The SFINCS model (Leijnse et al. 2021) is a reduced-complexity flood solver that includes advection and wind-drag terms in the Local-Inertial Equations, thereby solving the Simplified Shallow-Water Equations (SSWE). The inclusion enables the explicit resolution of rapid transients such as infragravity run-up without compromising the computational efficiency of the original formulation. The most recent version of SFINCS facilitates a quadtree grid. Thus, it allows spatially varying friction, infiltration, precipitation and a weakly-reflective generating–absorbing boundary so that fluvial, pluvial, tidal, wind- and wave-driven mechanisms can all be included within a single depth-averaged framework. Comparison against analytical solutions, benchmark experiments and wave-driven inundation cases shows that the SSWE model (SFINCS-SSWE) replicates shock propagation and long-wave run-up far more accurately than the advection-free LIE version at a moderate (typically < 20%) run-time. Eilander et al. (2023a) evaluated the performance of SFINCS using a case study in Mozambique, and it showed that it outperformed the catchment-based -macro-scale CaMa-Flood model (Yamazaki et al. 2013) in terms of overall accuracy.

SnapWave (Roelvink et al. 2025) is a fast, stationary wave-transformation engine that propagates offshore sea states to the nearshore on unstructured grids. It resolves an implicit 2-D wave-energy balance (refraction, shoaling, bottom friction and depth-limited breaking) for a single representative frequency and an explicitly resolved directional spectrum. It is solved by quadrant sweeping and converges in a few iterations, providing a very fast run-time, even on standard hardware without parallel processing. SnapWave is designed to be lightweight, serving as the near-shore wave module for shoreline evolution tools (ShorelineS), morphodynamic models (XBeach, Delft3D-FM) and flood models such as SFINCS, with good skill (> 0.9) for diverse open-coast, island and reef test cases, and simple to apply anywhere in the world.

Coupling SnapWave into the SFINCS quadtree grid (Leijnse et al. 2024; Leijnse et al. 2025) allows the system to compute dynamic wave-induced setup and associated infragravity wave height by (i) converting wave-breaking dissipation into forces raising mean sea levels, and (ii) optionally passing infragravity-wave data to a near-shore ”wavemaker” boundary; both are calculated at user-defined stationary time steps, so wave propagation is resolved within SFINCS. Moreover, the SFINCS' infragravity driver, if activated, introduces long-period waves at a specified surf-zone contour, and SSWE advection to propagate run-up over complex topography. Leijnse et al. (2025) shows that SnapWave coupling adds up to only 5–15% to total runtime. In their case study for Hurricane Florence (2018) hindcast, the coupled model is shown to be able to produce open-coast dynamic water levels, significant wave height, and infragravity wave height at a comparable magnitude to the full-physics XBeach simulation, with an estimated >1000 times faster computation speed.

2.4. Statistical Analysis Rationale

This section elaborates on the steps taken in the extreme value analysis of hydrodynamic modelling results on TC-induced surge and wave. Known options, descriptions, and the justification for the chosen procedure will be addressed.

2.4.1. Marginal extreme value analysis using POT and GPD

For the marginal extreme value analysis, two methods (see Figure 2.13) are commonly considered in metocean and coastal engineering studies: 1) the annual block maxima-generalised extreme value distribution (AM-GEV), which typically uses a single highest observation per year and 2) the peak over threshold-Generalised Pareto Distribution (POT-GPD), which could consider more than a single observation per year, so long as it exceeds a certain user-defined threshold. (Caires 2016) argued that the flexibility and more intense data usage in POT-GPD are proven to be advantageous, especially for a short data record. Considering that the STORM dataset may include more than one storm per year, the POT-GPD method aligns better with this study, as also employed in many TC-related studies (Leijnse et al. 2022; Gori et al. 2022; Marsooli et al. 2019; Lin et al. 2012). Elaboration and theoretical practice of the POT-GPD approach are presented below:

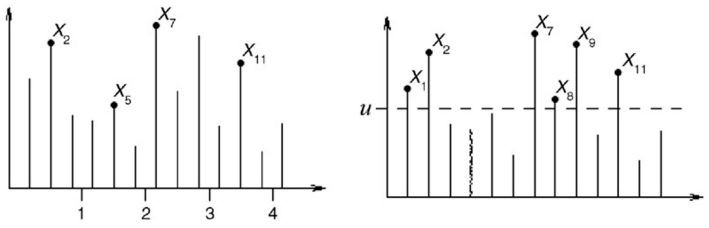

Figure 2.13: Block maxima (left) and peak over threshold method (right). Visualization by (Bhattacharyya et al. 2008)

Peak-over-Threshold (POT)

Extreme events are extracted with the POT approach by first declustering the time series into quasi-independent storm peaks and then retaining only those peaks that exceed a sufficiently high threshold u. Let $Y = X - u > 0$ denote the threshold excess. For a broad class of underlying parent distributions, the distribution of Y converges to the *generalized Pareto distribution* (GPD) as $u \to \infty$:

$$F_u(y) = \Pr(Y \le y) = 1 - \left(1 + \xi \frac{y}{\tilde{\sigma}}\right)^{-1/\xi}, \qquad y > 0,\ 1 + \xi\, y/\tilde{\sigma} > 0, \tag{2.5}$$

where $\tilde{\sigma} > 0$ is a threshold-specific scale and ξ is the tail (shape) parameter. Because every storm that crosses u supplies one observation, POT exploits far more data than the annual-maxima/GEV technique, resulting in more efficient and less biased estimates of low exceedance probabilities. Commonly, declustering windows must also be selected so that residual pairs are approximately independent, thereby justifying the Poisson assumption (independent and identically distributed) for the times of joint exceedances. However, this declustering step is not required in this context, as each tropical cyclone (TC) event is naturally independent due to the physical separation and distinct genesis mechanisms and timing of individual storms.

Generalized Pareto Distribution

The GPD in Eq. (2.5) encompasses three limiting tail forms: heavy-tailed Pareto ($\xi > 0$), exponential ($\xi = 0$) and bounded ($\xi < 0$), so the single parameter ξ fully determines tail heaviness and hence the extrapolated return levels (see Figure 2.14). Threshold stability implies that if the GPD holds for one high threshold, it remains valid for any higher threshold, with a linear adjustment $\tilde{\sigma}_{u_2} = \tilde{\sigma}_{u_1} + \xi(u_2 - u_1)$. This property underlies diagnostic plots (mean-residual-life and parameter-stability curves) that guide threshold selection and provide a check on the asymptotic assumption.

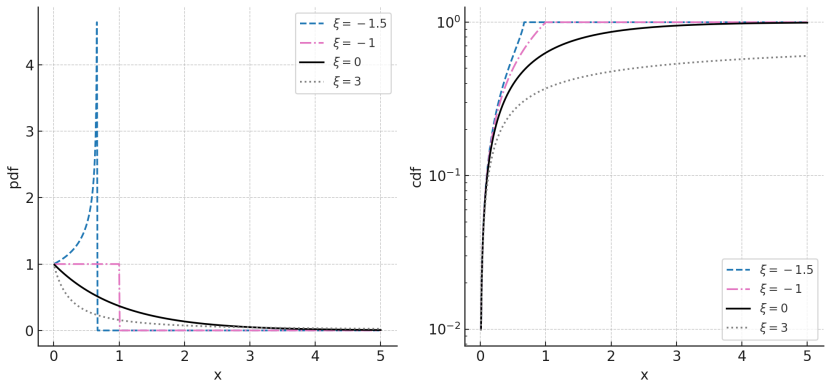

Figure 2.14: GPD probability density function (left) and cumulative density function (right) influenced by different shape parameters

Define κ_u as the mean number of threshold-exceeding peaks per year. For a return period m years, the GPD return level is

$$z_m = u + \frac{\tilde{\sigma}}{\xi}\left[(\kappa_u m)^{\xi} - 1\right] \quad (\xi \neq 0), \qquad z_m = u + \tilde{\sigma}\ln(\kappa_u m) \quad (\xi = 0). \tag{2.6}$$

Maximum-likelihood, probability-weighted moments (method of moments) and Bayesian schemes are commonly used to estimate $(\tilde{\sigma}, \xi)$. Asymptotically, these parameters are tied to those of the GEV fitted to block maxima, ensuring theoretical consistency between POT and annual-maxima analyses while often delivering narrower confidence intervals in practice.

2.4.2. Bivariate extreme value analysis using threshold-excess method and bivariate GPD

As the coastal water level along the coastline of the study area is driven by two central components —TC-induced surge and TC-induced wave —the joint extreme and dependence between these two drivers can be further analysed. Following the use of POT-GPD for marginal extreme value analysis, three representations of the joint extreme values method can be distinguished: 1) threshold-excess method (Resnick 1987), 2) point process method (Coles et al. 1994), and 3) conditional method (Heffernan et al. 2004) (see Figure 2.15).

Suppose that surge is X and wave is Y, thresholds for these two parameters have previously been determined in the POT-GPD analysis, (u_x and u_y). The threshold excess method (left plot) describes the dependence for extremes that simultaneously exceed both thresholds. Contrastingly, both the point process method (middle plot) and the conditional method (right plot) can handle joint extreme events even when only a single marginal threshold is exceeded. However, considering that the same

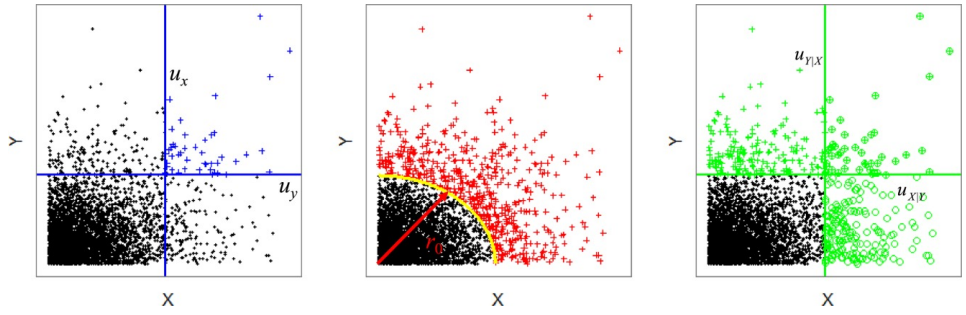

Figure 2.15: Visualisation (by Zheng et al. (2014)) of bivariate threshold excess method (left), point process method (middle), and conditional method (right)

TC-induced winds drive surge and waves, it is highly unlikely that such a situation, where extreme surge coincides with low waves or vice versa, would occur. Still, it does not mean that both the TC-induced surge and wave are entirely dependent. Through this logic, more parameterised and advanced approaches, such as the point process method and the conditional method, are unnecessary for this study. For this reason, the threshold excess method is employed in this study, in conjunction with the underlying logistic model, as also used in the joint TC-induced surge-rainfall analysis by Gori et al. (2022). The theoretical elaboration of this method is elaborated below:

Bivariate Threshold-Excess Method

For a surge–wave pair (X, Y) the marginal POT step transforms each component to a common scale—typically unit Fréchet, $X^* = -1/\ln F_X(X)$ and $Y^* = -1/\ln F_Y(Y)$. Joint extremes are then defined as (X^*, Y^*) entering the region $\mathcal{D} = \{x^* > u_x\} \cup \{y^* > u_y\}$. Within $\mathcal{D}$ the joint survivor is modelled by a bivariate GPD:

$$\Pr(X^* > x,\, Y^* > y) = \exp\{-V(x, y)\}\,, \qquad (x, y) \in \mathcal{D},$$

where the *exponent measure* $V(x, y)$ characterises extremal dependence. A censored likelihood treats points for which only one component exceeds its threshold as partially observed, while fully joint exceedances contribute through the mixed density $\partial^2 V/\partial x\, \partial y$. This formulation respects variable-specific thresholds yet yields consistent parameter estimates for the joint tail, a prerequisite for computing TC-induced compound surge–wave design events. Thresholds u_x and u_y are chosen by the same bias–variance trade-off as in the univariate case, guided by stability plots of the estimated dependence parameter(s).

Logistic Method

A widely used parametric form for $V(x, y)$ is the *logistic* model

$$G(x, y) = \exp\Big[-\left(x^{-1/\alpha} + y^{-1/\alpha}\right)^{\alpha}\Big]\,, \qquad 0 < \alpha \leq 1, \tag{2.7}$$

where α controls extremal dependence: $\alpha \to 0$ implies complete dependence, $\alpha = 1$ corresponds to asymptotic independence, and intermediate values represent varying strengths of tail association (see Figure 2.16). In the surge–wave context, empirical studies typically find $\alpha \in [0.4, 0.8]$, indicating moderate to strong dependence that intensifies design flood levels relative to independent assumptions.

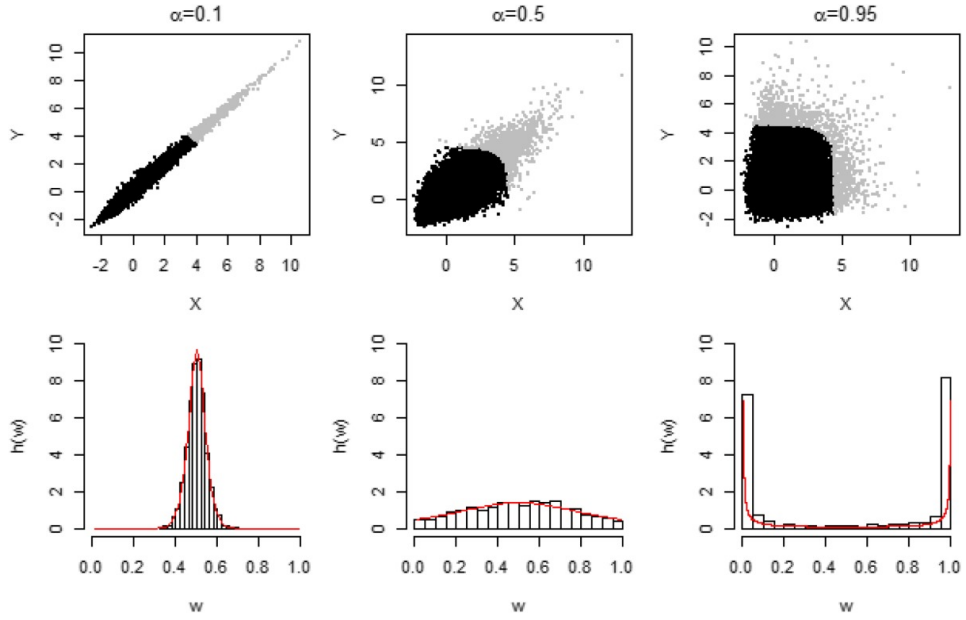

Figure 2.16: Illustration (by Zheng et al. (2014)) of the spectral density function, $h(w)$, for three datasets simulated using the bivariate logistic model with varying dependence levels ($\alpha = 0.1, 0.5$, and 0.95). **Top:** Scatterplots of each dataset, with extreme events highlighted in grey. **Bottom:** Histograms of the variable $w = \frac{x}{x+y}$ for the extreme events, with the corresponding spectral density functions $h(w)$ overlaid.

The logistic model is attractive because (i) it is closed-form and requires only one additional parameter beyond the marginal distribution parameters (threshold, exceedance frequency, shape and scale), (ii) it nests the independence limit, allowing formal hypothesis tests, and (iii) its likelihood is numerically stable even with modest sample sizes. When coupled with the bivariate threshold-excess likelihood, it yields nearly unbiased $\hat{\alpha}$ and lower root-mean-square error than alternative copula-based estimators for the dependence range typical of TC surge–wave pairs, while remaining computationally trivial to implement. Together, the univariate POT–GPD framework and the bivariate threshold-excess logistic model provide a theoretically consistent and empirically efficient toolkit for fitting TC-induced marginal and joint surge–wave extremes, enabling robust estimation of return levels and design contours required for coastal flood-risk assessments.

3

Data and Methodology

Building on the literature-informed rationale presented in the previous chapter, this chapter describes the datasets and modelling setups used to address the research objectives. The flowchart in Figure 3.1 above provides an overview of how all data, methods, and outputs are integrated within this study. The overall process is organised into four main parts for clarity, with a brief description as follows:

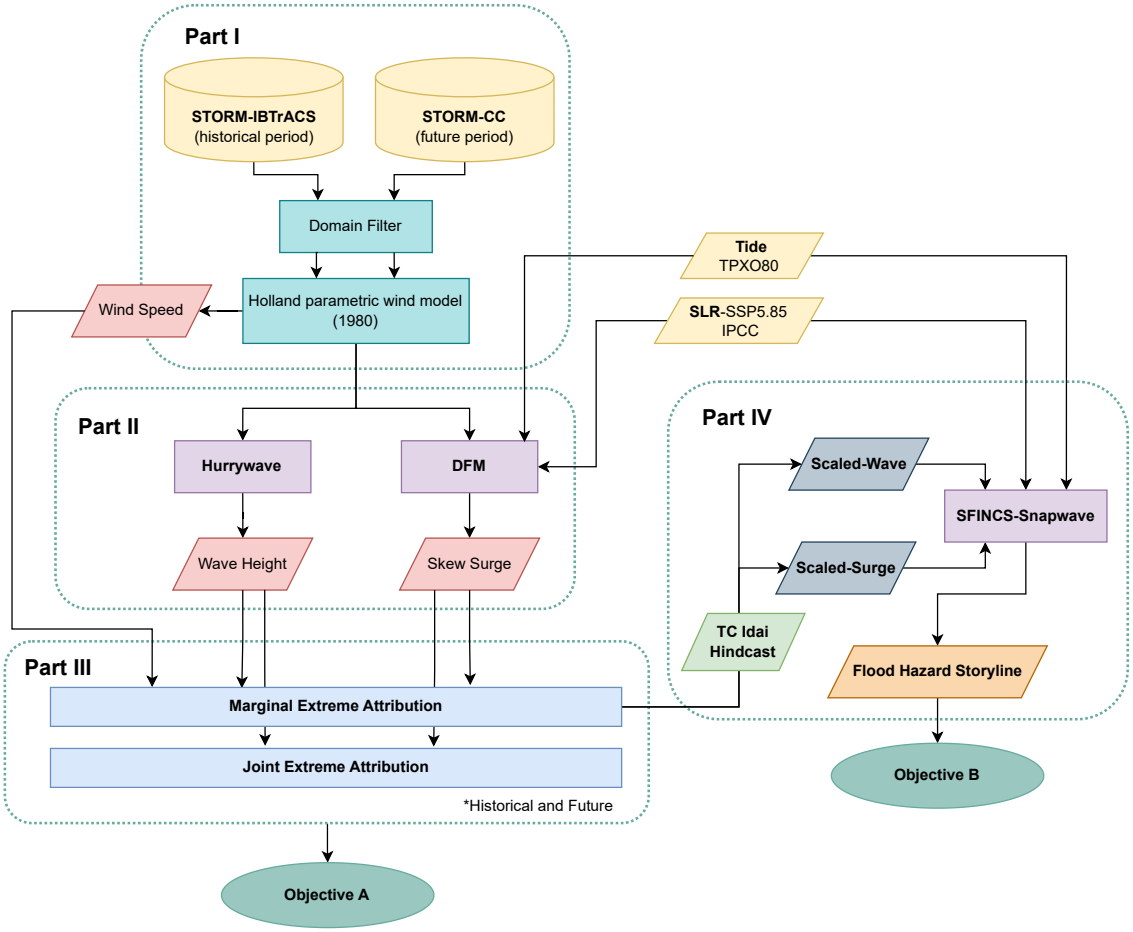

Figure 3.1: Modelling Flow Chart; left part focuses on the methodology that aims to achieve Objective A, meanwhile the right part focuses on Objective B

Methodology $Part\ I$, *"Domain Filter of STORM and Development of TC Wind Field"*, is based on the decision to use the STORM synthetic tropical cyclone tracks and the Holland (1980) wind model, as previously elaborated in Subsections 2.3.1 and 2.3.2. Starting from this step, two STORM distinctions are made: STORM-IBTrACS corresponds to the historical period, and STORM-CC represents the future climate condition, comprising four STORM-GCMs. One of the outputs of this methodological partition

is presented in Section 4.1, which summarises the general TC occurrences and intensity along the Mozambique channel. In the $Part\ II$ *"Surge and Wave Model of Filtered STORM Synthetic Tracks"*, utilising the STORM's TC Holland1980 wind field from the previous step, a water level (Delft3D-FM) and spectral wave evolution model (HurryWave) are conducted separately, following the rationale presented in Subsection 2.3.3. Furthermore, the chosen statistical procedure discussed in Subsection 2.4 underpins the steps, and extreme value attribution takes place in $Part\ III$ *"Marginal and Joint-Extreme Value Attribution"*. The concurring Holland1980 wind speed (from $Part\ I$), Delft3D-FM's surge, and Hurrywave's wave maxima (from $Part\ II$) will be used as input for this statistical procedure. The result of these attributions is what constitutes the answer to Objective A, which is presented in Section 4.2 and 4.3.

Lastly, in $Part\ IV$ *"Simulation of Future Climate Flood Hazard Storyline"*, as the name suggests, a future climate storyline of TC Idai will be developed and simulated. To achieve this step, a TC Idai surge and wave hindcast is first simulated, using a setup similar to that in $Part\ II$. The future scaled surge and wave are then derived based on the hindcasted STORM-IBTrACS return period, and reprojected into each STORM-GCMs' marginal distribution. These future scaled surges and waves represent what we previously referred to as "storminess change". These storminess changes, in addition to SLR, are then simulated more precisely using a coupled nearshore flow-wave model, SFINCS-SnapWave (see Subsection 2.3.3), producing the TC Idai flood hazard storyline in four different scenarios: historical, storminess change-only, SLR-only, and combined storminess change-SLR scenarios. The outcomes of this flood hazard storyline will directly address Objective B, and are presented in Sections 4.4. The following sections will delve deeper into the datasets used, as well as the detailed setups and analyses applied in each methodological part.

3.1. Dataset

3.1.1. STORM Datasets

Because tropical cyclones (TCs) are relatively rare and typically affect only small geographic areas, conducting extreme value analysis to estimate metrics in the upper tail distribution, like the 1-in-100-year return period, with reasonable confidence requires long-term records or modelled data. As previously elaborated in Section 2.3.1, one way to overcome this issue is to use a synthetic tropical cyclone tracks database. In this study, the synthetic tropical cyclone tracks databases, STORM-IBTrACS (Bloemendaal et al. 2020c) and STORM-CC (Bloemendaal et al. 2021), are employed. Five different scenarios are distinguished: 1) IBTrACS, which corresponds to the current climate (1980-2017), and 2) CMCC, 3) EC-Earth, 4) HadGEM, and 5) CNRM, which represent the future climate scenarios (2015-2050). Since this study focuses on comparing the upper-tail distribution of wind, wave, and surge characteristics under current and future climate conditions—specifically for events with a 100-year return period—using the first 5,000 years of the 10,000-year STORM dataset is considered sufficient (Grossmann-Matheson et al. 2023; Leijnse et al. 2022). As noted by Bloemendaal et al. (2020b), the full 10,000-year dataset is generated by repeating 1,000-year realisations based on the same statistical distribution ten times. Therefore, analysing just the first 5,000 years is expected to yield representative results that are statistically consistent with those obtained from the full dataset. Details on both STORM-IBTrACS and STORM-CC are presented below.

STORM-IBTrACS

The STORM-IBTrACS (Bloemendaal et al. 2020c) dataset is a 10,000-year global synthetic tropical cyclone (TC) archive generated using the Synthetic Tropical cyclOne geneRation Model (STORM) developed by Bloemendaal et al. (2020b). This dataset extends the observational record of TC activity based on 38 years (1980–2018) of historical best-track data from the International Best Track Archive for Climate Stewardship (IBTrACS) (Knapp et al. 2010), as shown in Figure 2.11. STORM uses a Monte-Carlo algorithm to resample and simulate TC genesis, tracks, intensities, and sizes to produce a long-term synthetic realisation database that preserves the statistical properties of the original IBTrACS dataset. The model accounts for spatial and seasonal distributions of genesis, environmental constraints such as maximum potential intensity, and post-landfall decay.

STORM-IBTrACS includes key cyclone properties at 3-hourly intervals, such as minimum central pressure, maximum 10-m wind speed, radius to maximum winds (Rmax), landfall flags, and distance to

coast. It offers statistically consistent coverage in historically data-scarce regions and allows for robust estimation of return periods for extreme TCs. The dataset is especially valuable for applications in coastal flood modelling, wind damage assessments, and probabilistic risk analysis. Unlike climate model output, STORM-IBTrACS reflects present-day climate conditions only and does not account for long-term climate variability or change.

STORM-CC
The STORM-CC dataset (Bloemendaal et al. 2021) is used to project tropical cyclone (TC) behaviour over the future period of 2015 to 2050. It was developed by Bloemendaal et al. (2022) using four out of the six high-resolution coupled ocean–atmosphere general circulation models (GCMS) that were affiliated with the High Resolution Model Intercomparison Project (HighResMIP). HighResMIP belongs to the broader Coupled Model Intercomparison Project Phase 6 (CMIP6) framework. The objective of HighResMIP was to examine how increasing model resolution, ranging from 25 km to 50 km, affects the simulation of climate variability and extremes, particularly tropical cyclones.

Four GCMs used in the STORM-CC development are: CMCC-CM2-VHR4 (Scoccimarro et al. 2017), EC-Earth3P-HR (E.-E.-Consortium 2018), HadGEM3-GC31-HM (Roberts 2017), and CNRM-CM6-1-HR (Voldoire 2019), all under the high-emission Shared Socioeconomic Pathway 585 (SSP585) scenario. The simulations cover the future period from 2015 to 2050. Bloemendaal et al. (2022) noted that up to 2050, the differences between SSP585 and lower-emission scenarios are relatively minor. Among the selected GCMS, only CMCC-CM2-VHR4 features the highest spatial resolution of 25 km $\times$ 25 km. The other three operate at 50 km $\times$ 50 km. While all models output data at 6-hour intervals, these were interpolated by Bloemendaal et al. (2022) to a temporal resolution of 3 hours for consistency and enhanced usability.

Despite their increased resolution, the GCMs still tend to underestimate TC intensity. Therefore, they cannot be used directly to forecast future TC characteristics. To address this, Bloemendaal et al. (2022) applied a method they referred to as the “delta” approach. In this technique, TC tracks are first identified in both historical and future GCM simulations using the method described by Roberts et al. (2020). Then, the statistical changes (absolute, relative or distribution shift)—or “deltas”—between the two periods are calculated for various TC parameters. These parameters include the number of storms per year, locations of genesis, latitude and longitude of tracks, and central pressure. The computed deltas are then imposed on the statistics from the STORM-IBTrACS dataset, which is itself designed to be statistically aligned with historical observations. The modified statistics are then resampled to produce projected future values. This entire process is carried out separately for each of the four GCMs, thereby generating synthetic future TC tracks for each model.

In typical climate change studies, it is common practice to compare GCM-predicted characteristics for historical periods with the ground-truth observation and further assess their biases. However, the formulation of STORM-CC does not use historical TC tracks generated by GCMs. Instead, it propagates the future changes in storm statistics directly to the STORM-IBTrACS dataset. This approach is based on the assumption that biases from baseline and future GCM scenarios are constant, negating the need for the standard bias correction approach. However, ignoring bias evaluation also means the inability to produce a performance-based weighted ensemble. Hence, in this study, we assume an ensemble median model combination.

3.1.2. Sea Level Rise Dataset

The NASA sea level projection tool, based on IPCC AR6 (Masson-Delmotte 2021), is used to determine the expected sea level rise along the Sofala coast in 2050. IPCC AR6 provides forecast data on total SLR and rise rate in different periods in the future under five different socioeconomic pathways (SSP1-1.9, SSP1-2.6, SSP2-4.5, SSP3-7.0, SSP5-8.5) with a resolution of 1°, as shown in Figure 3.2. To be consistent with the scenario used in the STORM-CC dataset, only the highest scenario, which is the SSP5-85 scenario, is considered in this study. In this emission scenario, the 5th-95th confidence interval of SLR by 2050 is 0.13–0.42 m with a median value of 0.25 m. This median value will later be used to superimpose water level boundary conditions under the future climate scenario.

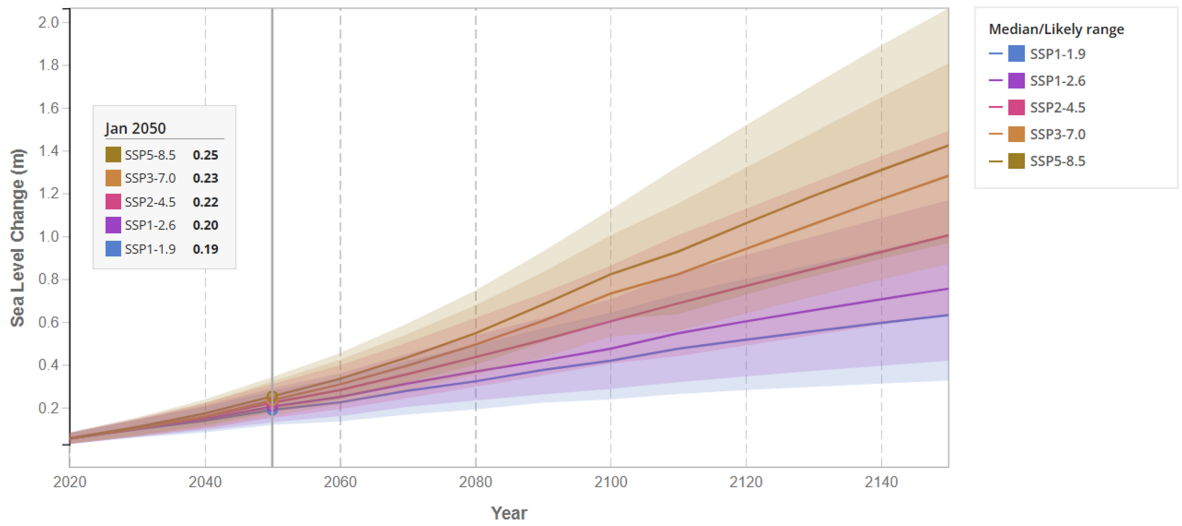

Figure 3.2: Values of SLR near Sofala Province according to IPCC AR6 Projection

3.1.3. Tide Dataset

Sea-surface elevation amplitudes for eight primary (M2, S2, N2, K2, K1, O1, P1, Q1), two long-period (Mf, Mm), and three non-linear (M4, MS4, MN4) harmonic constituents are calculated using the TPXO8.0 models (Egbert et al. 2002). This dataset is based on a data assimilation model integrating a numerical model with satellite altimetry. It provides data on tidal constituents at a 1/4° resolution at a global scale, which is helpful for a data-scarce region such as Sofala Province, Mozambique. Visualisation on M2 magnitude and phase variability near Sofala's coast has been presented before in Figure 2.4a. The extracted tidal constituents derived from this dataset will be constructed into a time series using a harmonic decomposition approach Codiga (2011). This time series will serve as a boundary condition along the open boundaries of the DFM model extent, later elaborated in Section 3.2.3.

3.1.4. Bathymetry, Topography, Land Cover and Population Dataset

This study employs the bathymetry dataset from GEBCO 2024 with a resolution of 15 arc seconds (~450 m), which is the most updated version of GEBCO, providing fewer discontinuities, especially where measured data is scarcely available, like in Sofala province (GEBCO Compilation Group 2024). Delta-DTM, an open CopernicusDEM-based digital terrain model (DTM) with a resolution of 1 arc-second (~30 m), is employed for the topography (Pronk et al. 2024). This DTM is intended explicitly for delta regions, especially in coastal inundation model applications using globally available datasets, such as in this study. Pronk et al. (2024) stated that this DTM might outperform other globally available datasets, such as MERIT. However, it is essential to note that this DTM only covers up to the elevation of +30 m above MSL and, therefore, is less suitable for studying river basin-scale flooding. Given the scope of this study, which focuses on coastal inundation only, Delta-DTM is still preferred with the hope of a more accurate depiction of overflowing processes. Both bathymetry and topography datasets are joined with CNES-CLS18 mean dynamic topography (MDT) correction for the MSL differences (Mulet et al. 2021). The resulting merged topography and bathymetry are presented in Figure 2.5. The Manning roughness coefficient from the ESA World Cover 2020 (Hammond et al. 2021) is used for the land area; meanwhile, the assumed uniform value of 0.02 (a default roughness for sea bed, representing a moderate level of bottom drag) is used for the sea, as no roughness dataset is available. This ESA World Cover 2020, alongside WorldPop population density dataset (CIESIN 2018), will also serve as a basis for exposure assessment in the $Part\ 4$ flood hazard storyline.

3.2. Methodology

3.2.1. Domain and Observation

Before delving into the detailed methodological steps involved in this study, it is important to distinguish the model domain used in each methodological part (I-V) and to identify the locations of the observation points. As shown in Figure 3.3, Parts I and II of the methodology focus on a scale larger than the Sofala region itself. The Delft3D-FM and HurryWave model domain is set more than ~ 500 km away from the most protruding part of Sofala's coast to ensure that the propagation of surge and wave from deeper water is considered. Meanwhile, the STORM domain filter is extended ~ 300 km inland to capture the tropical cyclone wind field that propagates beyond the landfall point. The Delft3D-FM and HurryWave model observation points along the Sofala coastline have spatial resolutions of 2 km and 5 km, respectively. The Delft3D-FM surge observation is set very close to the coastline, while the HurryWave's observation is set at more than -15 m depth to ensure deep water conditions. Time series of wind, waves, and surge are extracted at these points to allow for the joint and extreme value analyses in Methodology Part III. The SFINCS model in Part IV, which was used in the estimation of total water levels and coastal flooding within the storyline-based approach, is also configured along the same coastline. Details on how the model and analysis are set up and conducted in each part are shown in the following subsections.

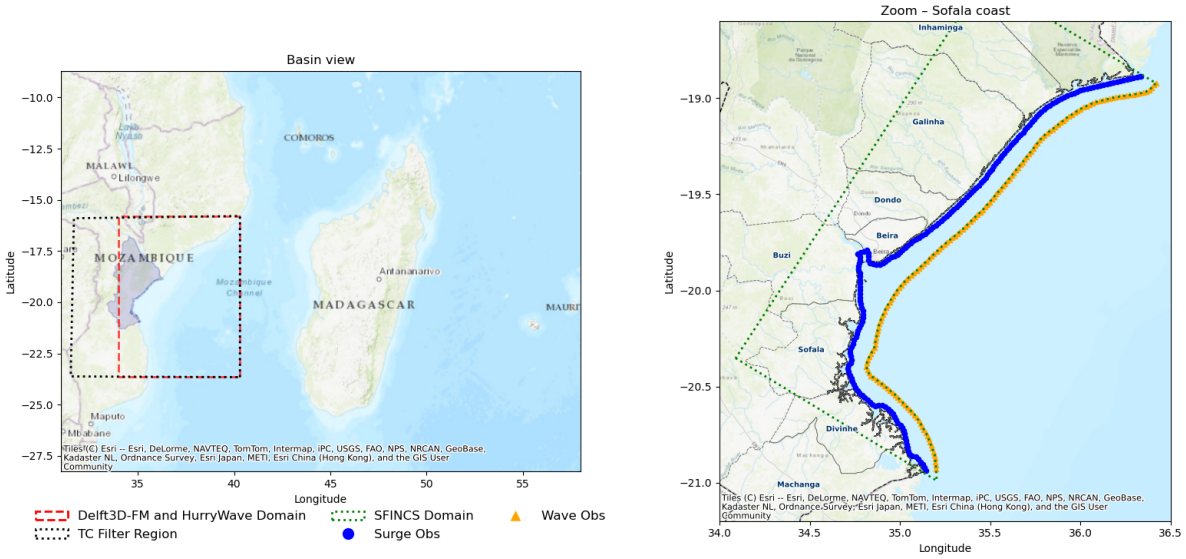

Figure 3.3: Left plot indicates the domain extent for STORM tracks filtering as well as Delft3D-FM and HurryWave extent (Methodology Part I and II, respectively). Meanwhile, the right plot indicates the observation points used to retrieve wind speed and wave height (yellow) as well as skew surge (blue) for Part III: marginal and joint extreme analysis. The green outline in the right plot represents the SFINCS domain, which is later used in Methodology Part IV.

3.2.2. Part I: Domain Filter of STORM and Development of TC Wind Field

The 5000 years sets of STORM-IBTrACS and STORM-CC first go through a domain filter process to make the later hydrodynamic simulation even more efficient. Aligning with the study region of Sofala province, only the South-Indian basin of this dataset is considered. Furthermore, we select only TC events with at least one point inside a 300 km radius from any point along Sofala's coastline. This distance is chosen based on the maximum recorded radius of 34-knot winds (R34) in the region, observed during TC Eloise (2021), which had an R34 of approximately 250 km based on IBTrACS (Knapp et al. 2010). The 300 km threshold includes a conservative buffer of 50 km to account for uncertainties in storm size, track, and impact range. R34 defines the radius at which sustained winds reach 34 knots (≈63 km/h), the threshold for tropical storm-force winds. Wind speeds below this threshold are generally classified as breezes, while those above 64 knots are considered hurricane-force (Knaff et al. 2007). Therefore, storms with all points beyond a 300 km radius are assumed to have a negligible influence on surge and wave conditions near Sofala. Furthermore, we cut the beginning or end part outside the hydrodynamic model domain (see Section 3.2.3 for each TC track, around 500 km seaward and 300

km landward.

In the second step, the tropical cyclone (TC) tracks from the STORM dataset are transformed into wind and pressure fields using the Holland1980 parametric model (Holland 1980) (see Section 2.3.2 for detail). The TC wind structure follows the methodology described in reference (Dullaart et al. 2021), employing a radial grid that extends up to 1000 km, with 375 grid points in the radial direction and 48 grid points in the angular direction. Background surface winds setup, such as surface wind reduction factor and a directional offset constant, is set following Benito et al. (2024), which employs the STORM-IBTrACS dataset for the east coast of Africa. An instance of the resulting Holland1980 wind field for TC Idai is presented in Figure 3.4.

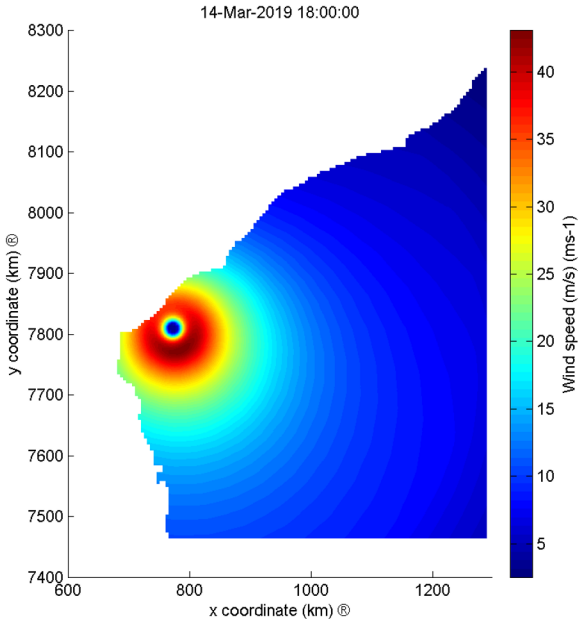

Figure 3.4: Visualisation of Holland1980 spatial wind field model applied to TC Idai. Warmer colour indicates higher wind speed.

3.2.3. Part II: Surge and Wave Model of Filtered STORM Synthetic Tracks

This section describes the hydrodynamic modelling approach used to simulate surge and wave for each filtered synthetic tropical cyclone (STC) wind field across all scenarios. Each surge and wave will be modelled independently, omitting interactions between waves, currents, and sea levels in shallow waters, equivalent to the approach employed in Marcos et al. (2019). This step will result in two key findings that are used for later steps: wind speed WS, significant wave height H_s, and skew surge SS maxima series that later will be used in extreme and joint extreme value analysis elaborated in Section 3.2.4.

Surge model in Delft3D-FM

For the surge, an observation point for every 2 km is set at sea very close to the coastline (not exactly at the coastline to avoid drying due to bathymetry averaging). The term 'surge' here refers to skew surge (later denoted as (SS) and not surge residual due to the following reasons: (1) a simple and unambiguous measure of the storm surge relevant to any predicted high water; (2) as Williams et al. (2016) demonstrated, there is negligible dependence between astronomical tide and skew surge, which simplifies the later development of TC Idai storyline's water level time series, as we can treat the tide and skew surge time series independently (if we generated time series of non-tidal residual, we would have to build an advanced approach to account for non-linear dependence between tide and the non-tidal residual).

The Delft3D-FM model (see Subsection 2.3.3) is used to model coastal tide and surge water levels. In this study, the configuration is constructed from scratch using the `dfm_tools` Python interface, meaning

that the computational domain, grid, bathymetry, boundary conditions, and forcing inputs are defined without relying on a pre-existing model setup (Deltares 2024a). This model spans from a latitude of 23.7°S to 15.8°S, and longitude from 34°E to 40.3°E, with the largest grid size set at 0.2 degrees and getting finer as it reaches lower depths on a staggered-unstructured grid, reaching 2 km resolution at the coastline. At the external boundary condition line (denoted by a red line in Figure 3.5), the TPXO8.0 tide timeseries is enforced (see Section 3.1.3), following a random year (1980-2017 for current climate scenario and 2015-2050 for future climate scenario), random day and hour at a specific month as detailed within each STORM's STC track. SLR offset is explicitly superimposed in this tide time series for the future climate scenarios to account for its effect on surge generation. Inside the Delft3D-FM domain, the previously developed TC wind field containing velocity components and atmospheric pressure is enforced as an internal boundary condition, representing surge generation along the TC tracks. Spinup time is set to 3 hours; meanwhile, a 24-hour tide-only simulation is employed to ensure proper tide propagation across all domains before it takes effect from the TC-induced wind field. A tide-only simulation without the TC wind field is also simulated. The difference between the TC-induced and tide-only time series is then used to form the basis for calculating the skew surge. This strategy is taken as some of the surge observation points lie outside the TPXO8.0 grid coverage.

To confirm that the tide distribution between each STORM variation is identical despite the differences in the number of STC tracks and random time selection, a validation is required. This validation is done by comparing the kernel density of the high-water tide that corresponds to each skew surge in every STC simulation, which is presented in Appendix A. Within the same kernel density plot (Figure A.1), the distribution of high-water tide from the nearest tide station, Beira IHO station, is also presented to confirm Delft3D-FM's performance in replicating the actual tide situation in the region through the use of TPXO8.0. Moreover, in the same appendix, the correlation plot between skew surge and tide is also presented (Figure A.2, validating the independence assumption previously discussed in the preceding paragraph.

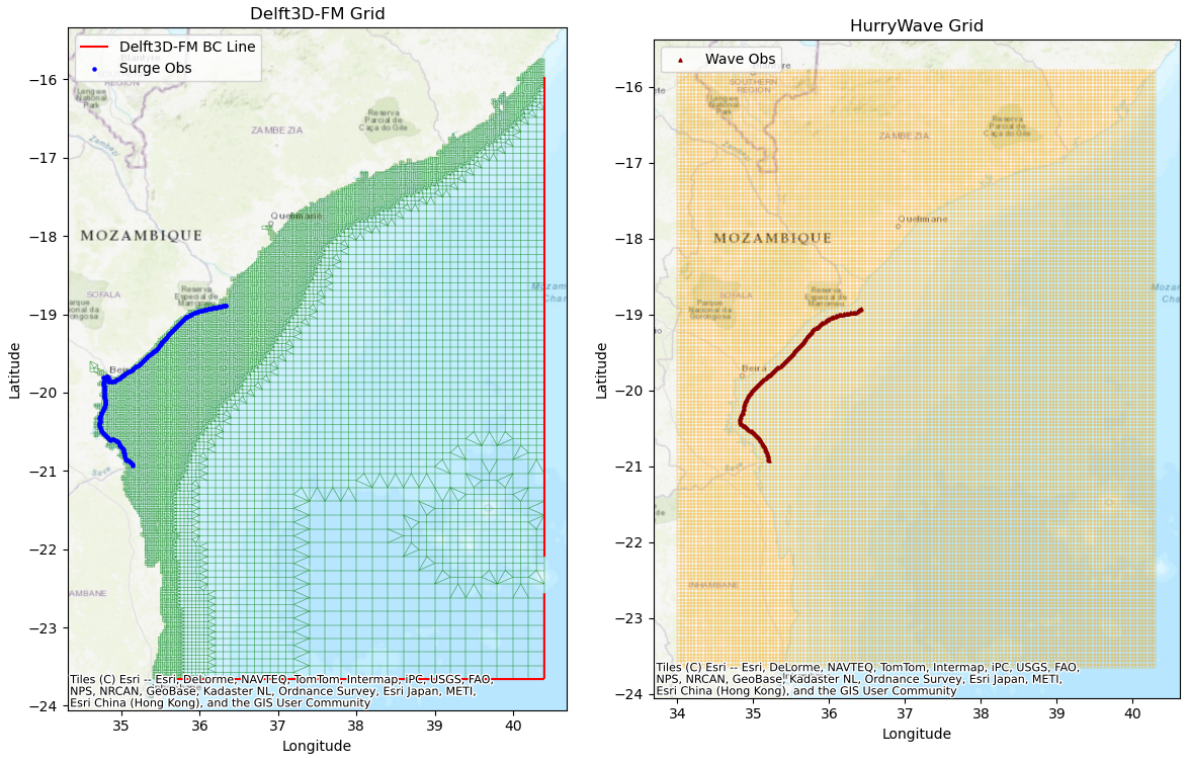

Figure 3.5: Delft3D-FM grid, boundary and observation setup (left) and HurryWave grid and observation setup (right). The grid resolution for the Delft3D-Fm model is set at 0.2° offshore and becomes increasingly finer near the coastline, with a resolution of 2 km. HurryWave grid is set at rectilinear uniform 5 km resolution.

Wave model in HurryWave

As for the wave, the HurryWave model (see Subsection 2.3.3 for details) is employed to model the TC-induced wave evolution. As in the Delft3D-FM setup, this model configuration is also constructed from scratch using the same GEBCO 2024 as a base bathymetry. The model extent is set similar to the Delft3D-FM model, with a uniform rectilinear grid resolution of 5 km as shown in Figure 3.5. A constant water level of 0 m is set across all simulations, neglecting tide and SLR, as we only focus on wave evolution under deep water conditions. Given that only the time-series for space-varying TC wind and pressure fields is considered, the spin-up time is set to 3 hours without any additional water level-only simulation like in the Delft3D-FM setup. Lastly, both Delft3D-FM and Hurrywave output timestep is set to 10-min to ensure peak skew surge and significant wave height can be appropriately captured without time-averaged decay. Furthermore, wind significant wave height (H_s) maxima (maximum 6-hour window from surge maxima) are derived at observation points that are set at around -15 m elevation every 5 km offshore of Sofala's coastline. This location is used to ensure the deep water wave condition.

3.2.4. Part III: Marginal and Joint-Extreme Value Attribution

Building on the theoretical background presented in Section 2.4, this section outlines the practical implementation of marginal and joint-extreme value analyses using the skew surge (SS) from Delft3D-FM output as well as wind speed (WS) and significant wave height (H_s) from HurryWave model outputs. Specifically, the univariate peak-over-threshold (POT) method with a Generalised Pareto Distribution (GPD) is applied for marginal extremes, and a bivariate threshold excess method with a logistic model is used for assessing compound surge–wave hazards.

Marginal Return Period

The marginal behaviour of TC-induced wind speed (WS), significant wave height (H_s) and skew surge (SS) is modelled using the Peak-Over-Threshold (POT) approach with the Generalized Pareto Distribution (GPD), following the theoretical foundation outlined in Subsection 2.4.1. Given the heavy-tailed nature of both variables, the POT-GPD method is well suited for extrapolating low-probability extremes from tropical cyclone events.

Thresholds are selected for each location using diagnostic tools of root mean square error (RMSE) between empirical and fitted quantiles, ensuring a balance between bias and variance (following the approach of Lin et al. (2012) and Marsooli et al. (2019)). Parameter estimation is performed using maximum likelihood. Return levels corresponding to desired return periods (e.g., 20-, 50-, 100-year) are then computed using the GPD formula introduced in Equation (2.6).

Joint Return Period

The dependence between H_s and SS is modelled using the bivariate threshold-excess method combined with the logistic model, as introduced in Subsection 2.4.2. The marginal distributions are first transformed to unit Fréchet space using the fitted GPDs, after which the joint cumulative distribution function (CDF) is evaluated using the logistic form (Equation (2.7)). This approach enables consistent estimation of joint exceedance probabilities. Model fitting is carried out via censored maximum likelihood, using only those tropical cyclone events where both variables exceed their respective thresholds. These thresholds are the same as those selected in the marginal analysis. The logistic dependence parameter α is estimated per site, allowing the characterisation of tail dependence from near-independence to near-perfect dependence (see Figure 2.16).

To evaluate the frequency of compound extremes, we compute the joint return period (JRP), defined as the expected time between events in which both H_s and SS exceed their marginal 100-year return levels x_T and y_T. Assuming tropical cyclone arrivals follow a Poisson process with rate λ, the JRP is calculated as:

$$\mathrm{JRP} = \frac{1}{1 - e^{-\lambda P}}, \tag{3.1}$$

where P is the joint exceedance probability, given by:

$$P = 1 - \Pr(X \leq x_T) - \Pr(Y \leq y_T) + G(x_T, y_T), \tag{3.2}$$

and $G(x_T, y_T)$ is the joint CDF from the logistic model. The arrival rate λ is derived from the number of tropical cyclone events identified per scenario within a 300 km radius (see Section 3.2.2) divided by the total 5000-year simulation period. For this JRP analysis, we took inspiration from Gori et al. (2022)'s R script and turned it into a Python script. This R script is originally used to analyse the joint return period of TC-induced rainfall and storm tide under climate change, with a case study in the US.

Attribution of changes in marginal hazards

To evaluate how climate change affects the extremes of individual and compound hazards, attribution is performed on both the marginal return period curves of H_s and SS, as well as their joint behaviour. For this research, the 100-year return period will be the benchmark for attributing the marginal (and later also joint) extreme shifts due to its common use in coastal protection design and risk analysis.

For the marginal case, the analysis focuses on two diagnostic metrics: the change in hazard magnitude (Δ, illustrated in Figure 3.6) and the effective return period (*Eff-RP*, illustrated in Figure 3.7) under future climate scenarios. The change in hazard magnitude is defined as the absolute difference between the future and historical values of a given return period:

$$\Delta_{RP} = z_{RP}^{\text{future}} - z_{RP}^{\text{historical}}, \tag{3.3}$$

where z_{RP} denotes the hazard level (either H_s or SS) associated with a specific return period RP.

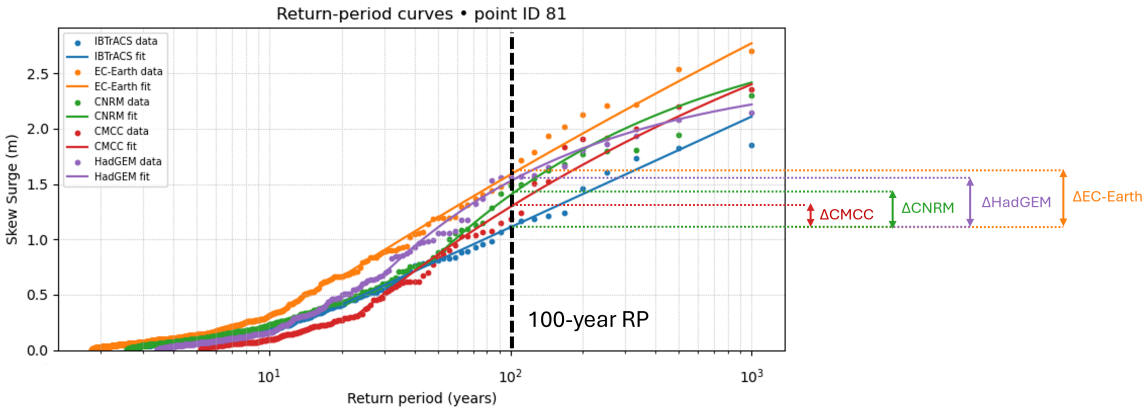

Figure 3.6: Visualisation of $\Delta_{100\text{yr RP}}$. The black bold dashed vertical line marks the 100-year return period. Each coloured vertical arrow represents the change in the 100-year return level between future and current climate simulations for a specific model. These differences, denoted as $\Delta_{100\text{yr RP}}$, quantify the projected increase in skew surge under future climate conditions across various STORM-CC's GCMs.

The effective return period in the future climate (*Eff-RP*) is obtained by determining the future return period corresponding to the historical 100-year hazard level:

$$\text{Eff-RP}_{100} = \frac{1}{1 - F^{\text{future}}(z_{100}^{\text{historical}})}, \tag{3.4}$$

where F^{future} is the cumulative distribution function under future conditions.

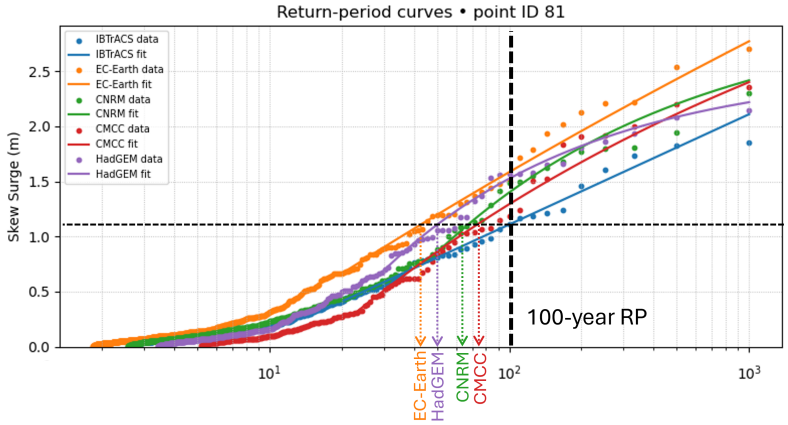

Figure 3.7: Visualisation of $\mathrm{Eff\text{-}RP}_{100}$. The black bold horizontal dashed line marks the 100-year skew surge level under the current climate (STORM-IBTrACS) fit. Each coloured downward arrow indicates the effective return period of that surge level under future climate projections from different STORM-CC's GCMs. The position of each arrow along the x-axis reflects how frequently the historical 100-year event is expected to occur in a future climate, with lower return periods indicating an increase in frequency.

Frequency vs Intensity sensitivity in marginal hazards

To gain a deeper understanding of the drivers behind changes in extreme event hazard under future climate scenarios, we decomposed the change in the 100-year return level (Δz_{100}) into two distinct components: *frequency* and *intensity*. This approach is based on the Generalised Pareto Distribution (GPD) fitted to exceedances over a fixed threshold (here, the CMCC threshold is used, as it is the lowest), using parameters estimated separately for the baseline (IBTrACS) and future GCM scenarios. The frequency component represents changes in the rate of exceedances, denoted by the parameter λ, which captures how often the threshold is crossed. The intensity component refers to changes in the distribution of exceedance magnitudes, governed by the GPD scale (σ) and shape (ξ) parameters.

We isolate each contribution by computing the return level in three configurations:

- Baseline: $z_{\text{historical}} = z_{100}(\lambda_{\text{historical}}, \sigma_{\text{historical}}, \xi_{\text{historical}})$
- Frequency-only: $z_{\text{freq}} = z_{100}(\lambda_{\text{future}}, \sigma_{\text{historical}}, \xi_{\text{historical}})$
- Intensity-only: $z_{\text{int}} = z_{100}(\lambda_{\text{historical}}, \sigma_{\text{future}}, \xi_{\text{future}})$

From these, the absolute contributions are defined as:

$$\Delta z_{\text{freq}} = z_{\text{freq}} - z_{\text{historical}}$$
$$\Delta z_{\text{int}} = z_{\text{int}} - z_{\text{historical}}$$

To allow consistent comparison, we compute the magnitude-normalised fractions:

$$\text{Frequency Fraction} = \frac{|\Delta z_{\text{freq}}|}{|\Delta z_{\text{freq}}| + |\Delta z_{\text{int}}|}$$
$$\text{Intensity Fraction} = \frac{|\Delta z_{\text{int}}|}{|\Delta z_{\text{freq}}| + |\Delta z_{\text{int}}|}$$

This decomposition allows an attribution of observed return level changes to either an increased occurrence of exceedance events or a shift in the tail heaviness of their magnitude distribution.

Attribution of changes in joint hazards

For compound hazard attribution, changes in the joint distribution are assessed by computing the future return period associated with a joint extreme event, defined as the co-occurrence of both H_s and SS exceeding their respective historical 100-year levels (also known AND scenario). This joint event corresponds to the baseline joint return period. The corresponding future return period, referred to as the

effective 100-year joint return period (*Eff-100yr-JRP*, illustrated in Figure 3.8), is calculated using the same historical thresholds (x_T, y_T), but evaluated with the joint distribution derived from future storm simulations.

This attribution framework allows for the disaggregation of future hazard changes into interpretable shifts in hazard magnitude and frequency, facilitating a clearer understanding of climate-driven shifts in both univariate and joint extreme behaviour. While this study centres on the 100-year threshold in the main results, return periods of 20, 50, and 200 years are similarly evaluated and provided in the Appendix.

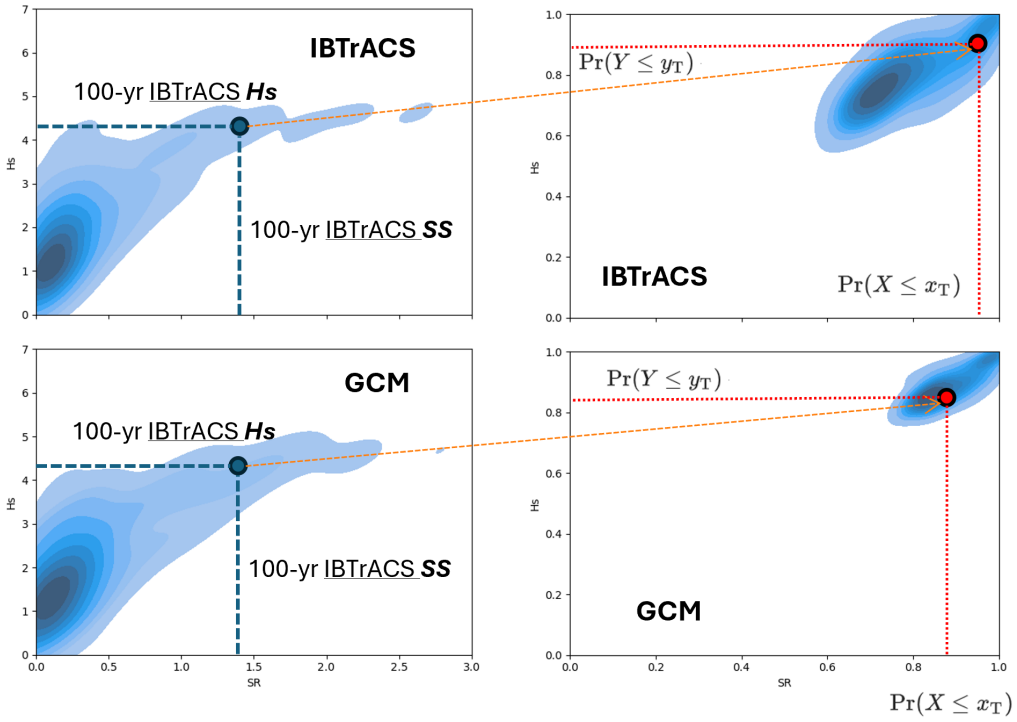

Figure 3.8: Visualisation of joint extreme value attribution. The left panels show the joint distribution of surge and wave height in real values, while the right panels present the same data in cumulative distribution function (CDF) space. The top row corresponds to the current climate distribution, and the bottom row to the future climate distribution. Blue dots indicate the 100-year return period (RP) surge-wave point under the current climate, while red dots show its position in CDF space under both the current and future distributions.

3.2.5. Part IV: Simulation of Future Climate Flood Hazard Storyline

The storyline for Tropical Cyclone (TC) Idai time series was developed using a structured three-step approach to simulate both surge and wave characteristics under future climate scenarios:

TC Idai Hindcast

As no observation data is present during the TC Idai event, the skew surge (SS) and significant wave height (H_s) hindcast time seriesis acquired through explicit simulation of surge and wave using the same exact setup of Delft3D-FM and HurryWave elaborated earlier in Section 3.2.3. The wind field used in this model is developed based on historical best-track data (IBTrACS) (not STORM-IBTrACS). The extracted time series of near-coastline surge and offshore wave (see Figure 3.3) from this hindcast will serve as a basis for return period mapping and scaling elaborated in the following Subsection. Additionally, an extra water level time series is also extracted at the wave observation points, which will later be used as an offshore boundary condition for the SFINCS-SnapWave model.

Return Period Mapping and Scaling

At each near-coastline surge and offshore wave observation location (see Figure 3.3), the return periods of Idai's simulated SS and H_s were estimated using fitted historical marginal distributions from the calculation in Section 3.2.4. These return periods were then mapped to corresponding hazard magnitudes under future climate conditions, based on marginal distributions derived from each STORM-CC's GCM. A scaling methodology (see Figure 4.12) was applied to adjust the historical time series, such that the future scenario preserves the same return period as the historical event while reflecting GCM-specific water level and wave progression. Especially for wave, the wave period time series is estimated such that the future climate storyline exhibits the same wave steepness as the historical one. Other wave parameters, such as wave direction and directional spreading, are kept consistent with historical values. In the main body of this research, we only take the historical and STORM-GCMs' ensemble median scaled water level and wave time series to feed into the nearshore SFINCS-SnapWave model discussed in the following Subsection.

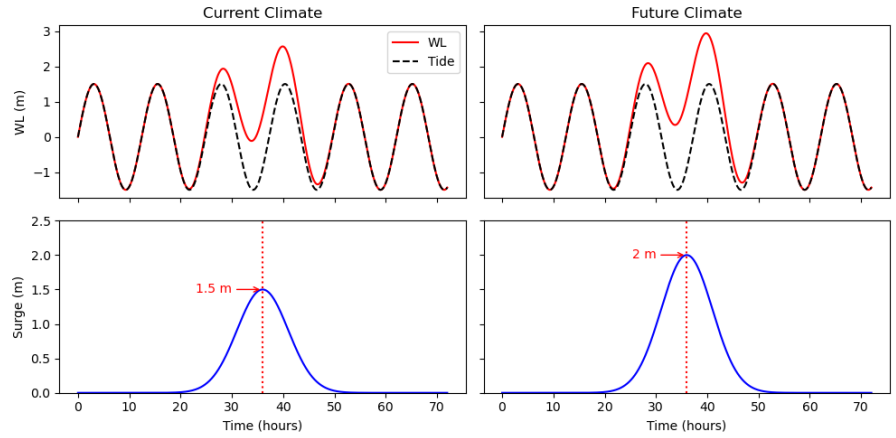

(a)

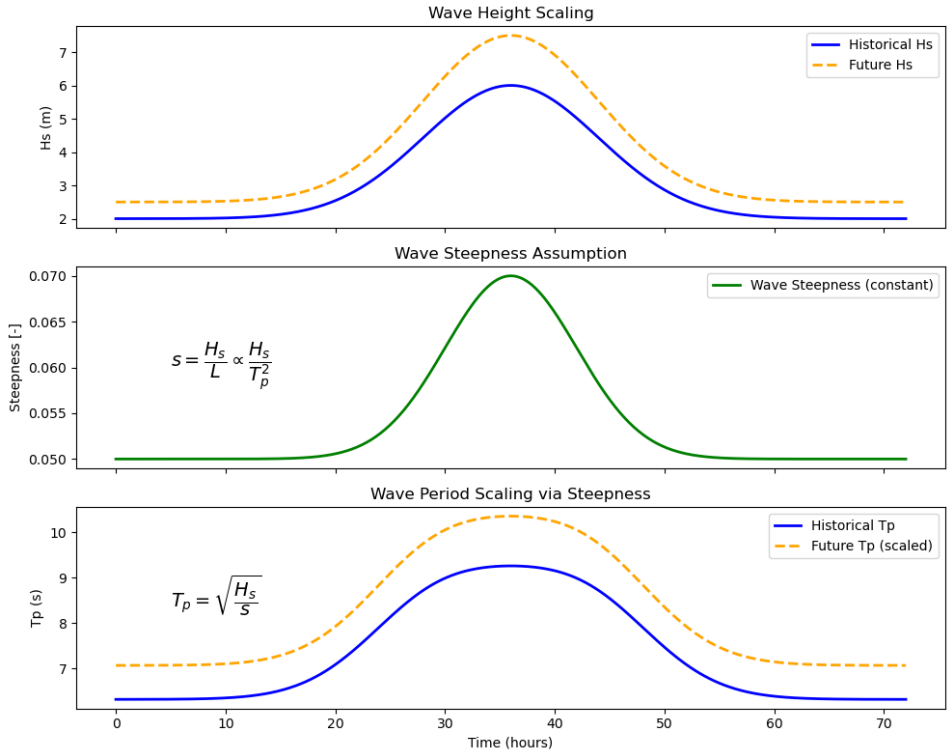

(b)

Figure 3.9: Scaling water level (a) and wave (b) timeseries for future climate storyline

Nearshore Re-simulation Using Scaled Inputs

To evaluate the impact of historical and future TC Idai storyline on coastal inundation, a two-iteration modelling strategy is employed. This dual approach serves two purposes: the first iteration quantifies the dynamic wave-induced components (i.e., setup and infragravity swash) at the shoreline, while the second iteration translates these effects, superimposing with the skew surge and SLR counterfactuals, into inundation impacts using a physically consistent, coastline-forced boundary. The first iteration thus utilises a complete SFINCS-SnapWave model setup (see Subsection 2.3.3 for a detailed description of the SFINCS-SnapWave model). In contrast, a faster SFINCS-only model is employed for the second iteration, as it focuses solely on simulating the superposition of near-coastline water levels due to tide, skew surge, wave setup, infragravity swash, and SLR. The grid resolution in both iterations is developed using the same three quadtree refinement levels, from 960×960 m at most offshore locations to 30×30 m nearshore (see Figure 3.10). This fine resolution, especially near the coastline, allowed for high-resolution representation of surge-wave interaction, accommodating both wave setup and infragravity wave-driven dynamic swash motion. This model employed bathymetry, MDT correction, and topography as stated in Section 3.1.4.

First Iteration: Offshore-forced wave-induced decomposition

The first iteration focuses on capturing wave-induced water level components using offshore boundary forcing. The external boundary for both wave and water level input is placed along the offshore HurryWave observation points indicated by the yellow line in Figure 3.10. Wind forcing is applied as a surface boundary condition using the spider-web wind and pressure field representation of historical TC Idai, spatially varying across the entire model domain rather than being limited to the external boundaries, as in the previous Delft3D-FM hindcast model. For each simulation, the model is driven by either the historical or the ensemble-median scaled future wave time series, while maintaining the same historical water level time series at the offshore boundary. This approach avoids inconsistencies that would arise from applying scaled surge values—originally derived at nearshore locations—at offshore boundaries, where the surge amplification is significantly lower. Using nearshore-scaled values at an offshore boundary would introduce unrealistic gradients and compromise the physical reliability of the tide and surge propagation.

To isolate wave-induced contributions at the coastline surge observation location, a transect is defined perpendicular to the coastline at each surge observation point. Along this transect, the following three model variations are executed:

1. *SnapWave & IG Wave Paddle* – includes both short-wave and long-wave (infragravity) forcing.
2. *SnapWave-only* – includes only short-wave forcing.
3. *Water level-only* – includes no wave forcing (tide and surge only).

The time series extracted along the transect are then differenced to isolate the contributions of various wave-induced components:

- *Wave setup* = SnapWave-only − Water level-only.
- *Infragravity (IG) swash* = SnapWave & IG Paddle − SnapWave-only.
- *Total wave runup* = SnapWave & IG Paddle − Water level-only.

The wave setup and IG swash time series are retained for diagnostic interpretation, helping to quantify the magnitude of wave-induced contributions at the coast. Meanwhile, the resulting wave runup time series is used as boundary input for the second iteration.

Second Iteration: Coastline-forced inundation simulation

The second iteration focuses on simulating coastal inundation using coastline boundary forcing, as indicated by the green line in Figure 3.10. The SnapWave module is deactivated, and the model is forced at the surge observation location using a composite total water level time series, defined as:

- Historical or scaled future tide–surge water level (as in Figure 3.9a), and
- Wave runup time series derived from the first iteration.

This modelling approach enables a consistent and physically robust simulation of compound flooding from tide, surge, and wave runup under both historical and future climate scenarios. By decoupling offshore wave dynamics and using derived runup as a boundary input, this iteration focuses computational resources on inundation processes without loss of physical accuracy.

Within this inundation model, exposure of land cover and population is assessed through a spatial overlay technique, where the simulated flood extent is intersected with static datasets from ESA WorldCover and WorldPop, as previously described in Subsection 3.1.4. Lastly, it is important to iterate that no flood depth threshold is set within this exposure analysis, meaning that all areas within the inundation footprint are considered exposed, regardless of depth.

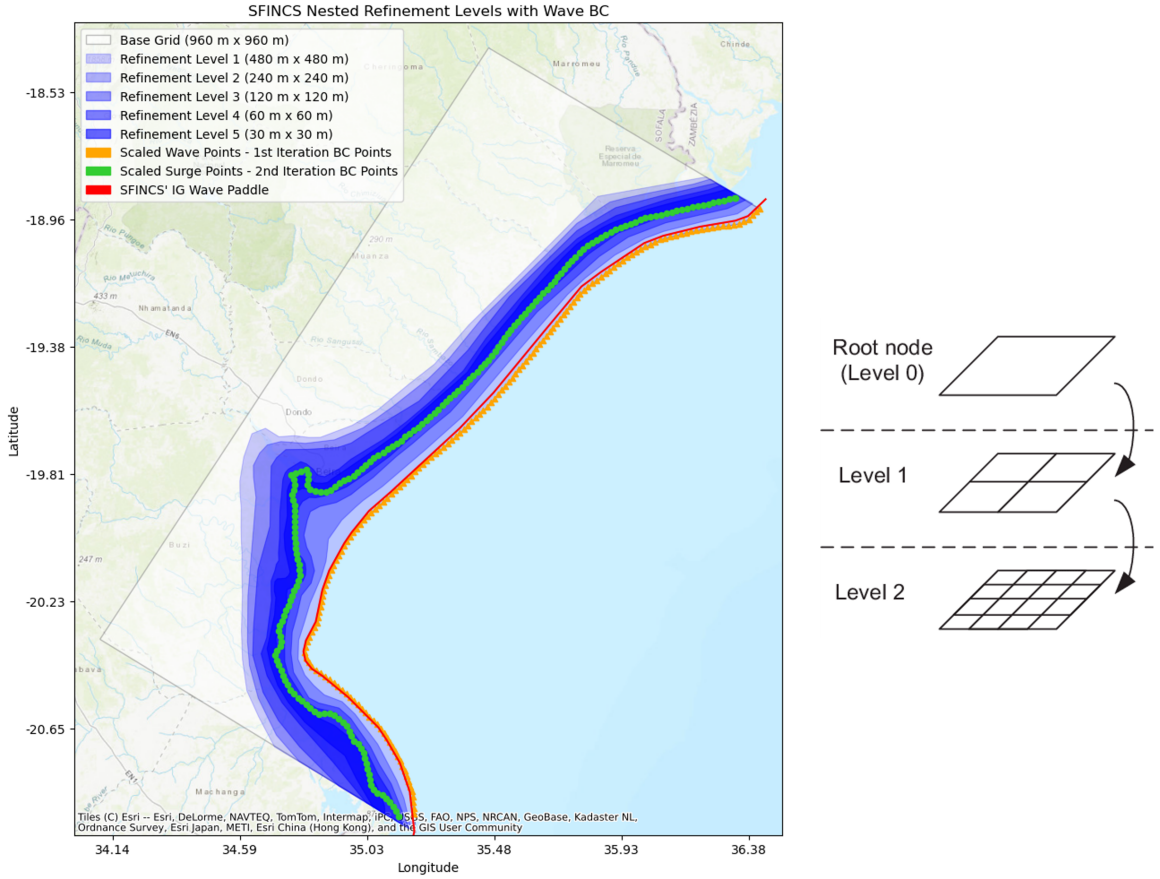

Figure 3.10: The left map shows SFINCS' grid, IG wave paddle and boundary condition setup for 1st (yellow line) and 2nd iteration (green line). The grid consists of three quadtree refinement levels, ranging from the base grid of 960 x 30 m to 960 x 30 m. The right figure shows what quadtree refinement looks like (original visualisation by Richter et al. (2013)).

4

Results

In this chapter, the results will be interpreted, and a takeaway will be drawn at the end of each section. This takeaway, along with its implications (Section 5.1), will serve as a basis to answer research questions in the Conclusion chapter. More specifically, Section 4.2 addresses marginal extreme attribution, and Section 4.3 addresses joint extreme attribution, both of which will be explored concerning research questions in Objective A. However, before that, a brief built-up discussion on overall TC behaviour in the Mozambique channel is presented in Section 4.1. Lastly, Objective B's research questions will be covered in Section 4.4, which focuses on TC Idai hindcast and future climate storyline.

4.1. TC Occurrences and Intensity in Mozambique Channel

This section presents the result of Methodology $Part\ I$, "Domain Filter of STORM and Development of TC Wind Field", specifically the domain filter step elaborated in Subsection 3.2.2.

We begin our results discussion by first looking at the filtered STC tracks within each STORM scenario, which is the output from the methodology Part I (Subsection 3.2.2). Figure 4.1 shows TC yearly occurrence probability within a 200 km vicinity per 10 km grid cell based on STORM-IBTrACS and its differences to STORM-GCMs. It is notable that, according to STORM-IBTrACS, the yearly occurrences in the deep waters of the Mozambique Channel off the coast of Sofala are approximately 0.3, whereas along the coastline, they are around 0.1. These values are twice as much as we saw before in Figure 2.2 (or more clearly shown in Figure B.1), which is based on the actual IBTrACS record. This discrepancy is due to the rate estimation being based solely on historical tracks (1980–2020, in the case of Figure 2.2), which contains very few events over a relatively short period, and may introduce inaccuracy as it does not fully capture the possibility of TC arrival across a sufficient portion of the region. As opposed to that, the Monte Carlo random sampling approach used in STORM (as elaborated upon in Subsection 2.3.1) yields a significantly larger number and a well-spread set of samples, covering almost every possible track within the region. This finding of higher TC occurrences when using synthetic TC datasets compared to strictly on historical tracks is also demonstrated in similar studies (Deltares 2021; Nederhoff et al. 2021).

Within Figure 4.1, we can also observe that among the STORM-GCMs ensembles, only STORM–EC-Earth produces a higher annual TC occurrence (0.667/year) than STORM–IBTrACS (0.507/year), followed closely by STORM–CNRM with a comparable rate of ~0.5/year. STORM-HadGEM and CMCC produce the least amount of tracks within the domain, with only ~0.4 and ~0.3, respectively. However, upon closer examination of the spatial variability, we found that despite a decrease in overall domain-wide TC probability, STORM-HadGEM still manages to sustain the number of occurrences in the nearshore region, with almost no difference in TC probability compared to STORM-IBTrACS. On the other hand, STORM-CMCC's TC probability dropped by around 0.05 nearshore, in contrast to STORM-CNRM and EC-Earth, which show ~0.05 and ~0.1 jumps, respectively. These findings indicate the importance of TC movement patterns, in the sense that, even with fewer total number of TC events, the spatial distribution of TCs significantly influences the likelihood of storms reaching the coast or even making landfall.

Furthermore, Figure 4.2 highlights the spatial variability of STORM's TC intensity over the Mozambique channel based on 5000 years of simulation each. This figure visually represents a gradient of increas-

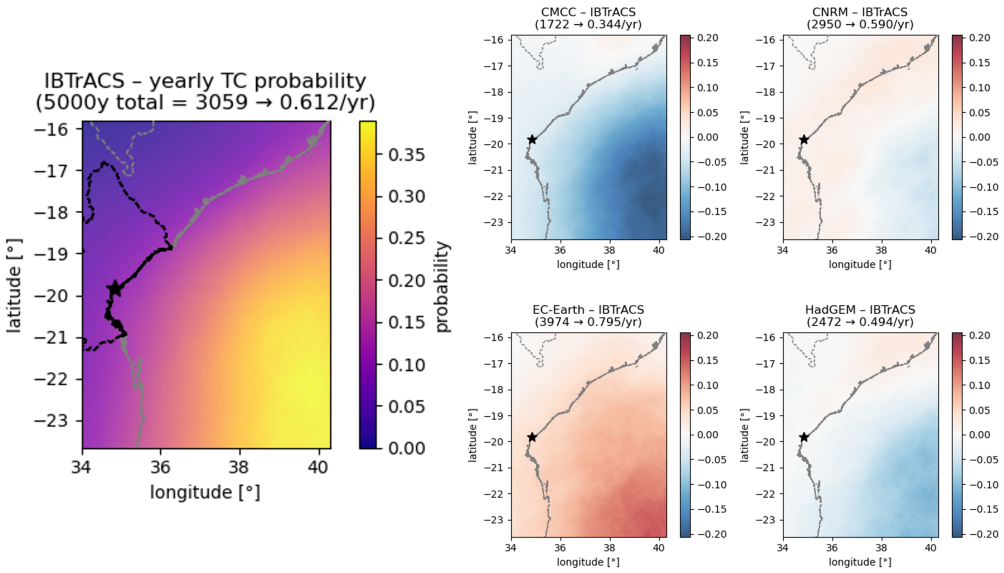

Figure 4.1: Left figure shows TC yearly occurrences probability within 200 km vicinity per 10 km grid cell in Mozambique channel based on domain-filtered STORM-IBTrACS. Meanwhile, the four collage plots on the right illustrate the differences compared to STORM-CC; blue indicates less frequent occurrences, and red represents higher occurrences. Above each plot, the number of filtered TC tracks from the first 5000 years of each STORM dataset is indicated, along with its mean occurrence per year for the entire domain. The dashed black line represents the administrative land border of Sofala, with a star symbol indicating Beira's coordinates, and the grey line depicts Mozambique's administrative boundary.

ing TC maximum 10-min sustained wind speed, with warmer colours (reds) indicating higher intensity along the track segments. Orange-ish colour or around 40 m/s indicates around TC category 2 (see Table 2.1). Compared to the IBTrACS reference, STORM CNRM, HadGEM and EC-Earth demonstrated notably more intense and widespread high-wind track segments. In contrast, STORM CMCC exhibits a comparable yet slightly higher overall intensity pattern to IBTrACS. The bottom-right bar plot quantitatively supports this observation, showing that while the majority of storms fall within the TD–Cat 2 category, HadGEM yields the highest proportion of Category 3–5 tracks (~6.7%), followed by EC-Earth and CNRM. It is also interesting to note that STORM-IBTrACS is found to produce the highest ratio of tropical depression tracks, at least around 10% higher than those of the STORM-GCMs ensemble, leading to a lower ratio of more intense TC categories. These results suggest that while track occurrences and movement vary across ensembles, the intensity distribution, particularly the presence of extreme wind events, also becomes a key differentiator among the STORM datasets.

***Takeaway** for Section "TC Occurrences and Intensity in Mozambique Channel":*

In a nutshell, an examination of the STORM datasets across the Mozambique Channel off Sofala's coast illustrates that both the occurrence and intensity of tropical cyclones exhibit high spatial and inter-model variability. While the synthetic datasets generate more frequent TCs compared to historical records, their spatial distributions, especially the nearshore occurrences probability and intensity, vary significantly across GCM ensembles. Notably, EC-Earth and CNRM both have elevated nearshore occurrences and more intense wind profiles, whereas CMCC has reduced occurrences and lower nearshore intensities. On the other hand, HadGEM exhibits an opposite pattern: with a lower annual domain-wide TC probability overall, it has nearshore occurrence rates comparable to STORM–IBTrACS but displays the strongest evidence of a shift towards increased wind intensity, with the greatest proportion of Category 3–5 events. The following section builds on this information by examining more closely how these variations in TC occurrences and intensity influence the spatial distribution of extreme values in wind speed, along with their resulting skew surge, and wave height along Sofala's coast.

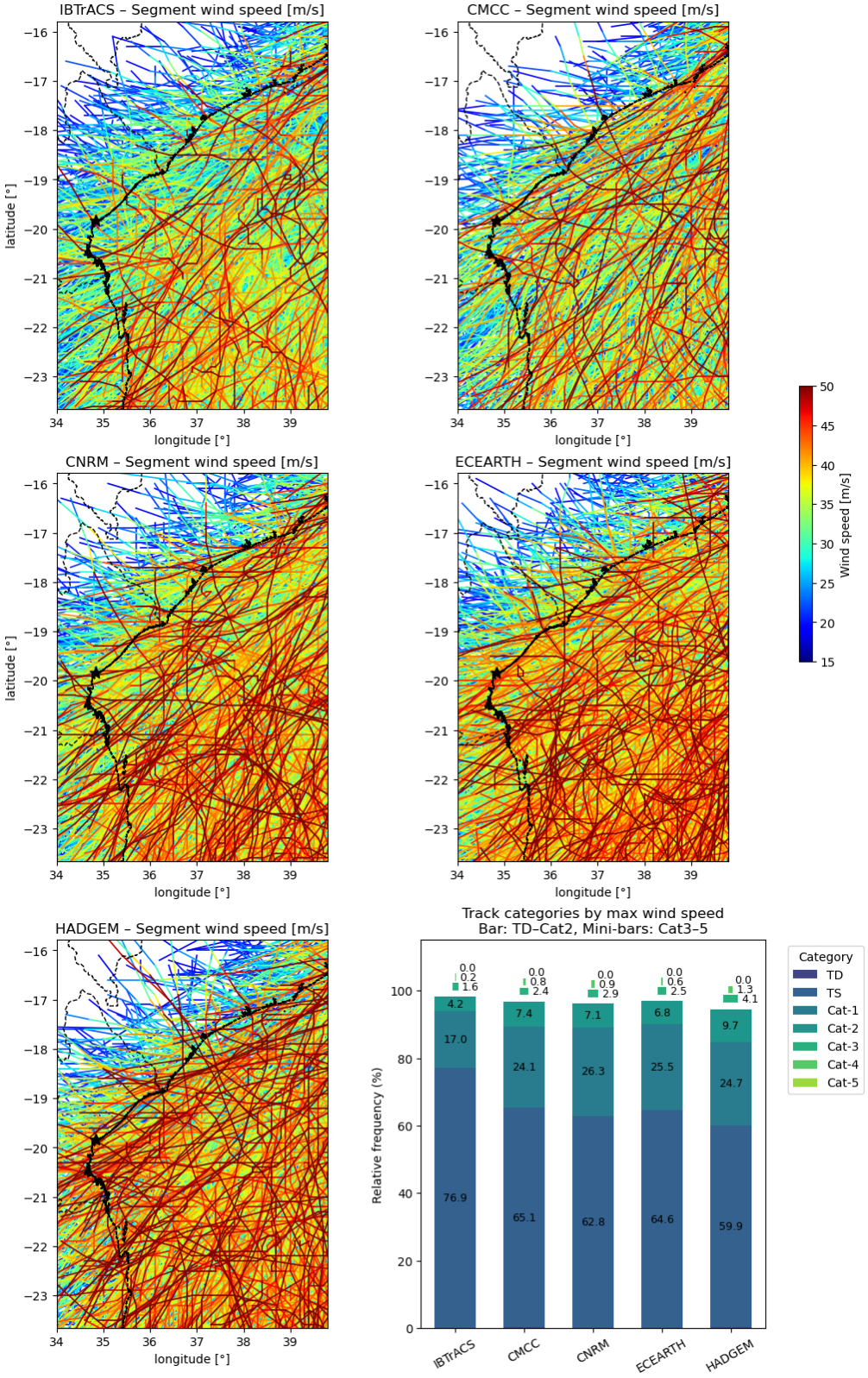

Figure 4.2: 5000 years of STORM TC track's eye maximum wind speed intensity in Mozambique channel, in order from top left to bottom left: IBTrACS, CMCC, CNRM, EC-Earth, and HadGEM. The segment order is arranged so that the track with higher wind speeds is displayed above the track with less pronounced intensity, with warmer colours indicating higher wind speed. Same as the previous figure, the dashed black line represents the administrative land border of Sofala, with a star symbol indicating Beira's coordinates. The bottom-right plot shows the relative occurrences of each TC track's highest category within the domain for each STORM variation. Lighter colours represent higher catastrophic category, from Tropical Depression (TD), Tropical Storm (TS) to Cyclone Category 5 (Cat 5).

4.2. Attribution of Changes in Marginal Extreme TC-Induced Wind, Surge and Wave along Sofala's coast

This section presents one of the results of Methodology $Part\ III$ "Marginal and Joint-Extreme Value Attribution", with emphasis on the marginal attribution as elaborated in Subsection 3.2.4.

4.2.1. Sensitivity to exceedance frequency vs intensity in extreme upper tail distribution

Building upon the differences in tropical cyclone occurrence and intensity across the STORM datasets (Figures 4.1 and 4.2), we further investigate how these differences translate into changes in extreme TC-induced coastal hazards. Specifically, we first aim to distinguish whether the increase (or decrease) in the 100-year return levels of wind speed, skew surge, and significant wave height is more strongly influenced by changes in *exceedance frequency* (i.e., how often extremes occur) or *exceedance intensity* (i.e., how extreme they are when they occur). This attribution is achieved through a statistical decomposition based on the Generalised Pareto Distribution (GPD), where return level shifts are recomputed by isolating contributions from the rate of exceedance (λ) and from the GPD shape and scale parameters (ξ, σ). By normalising the absolute contributions of each component, we obtain magnitude-based fractions that reflect the relative influence of frequency and intensity on the total change in hazard severity. See the Methodology Subsection 3.2.4 for a more detailed description.

As shown in Figure 4.3, frequency emerges as the dominant driver of change across all hazard types and GCM scenarios. In most cases, frequency accounts for more than 75% of the absolute change in the 100-year return level, especially in EC-Earth and CNRM ensembles, which aligns with their elevated nearshore TC occurrence probabilities. Even in HadGEM, where the intensity distribution appears to shift towards higher wind categories (cf. Figure 4.2), the frequency component still contributes a greater share of the return level increase for both surge and waves. CMCC is the only scenario where intensity plays a more comparable role, likely due to both a reduced overall TC rate and a more moderate intensity profile. These findings reiterate that, for most cases, the projected changes (increase or decrease, depending on the STORM-GCMs variation) in coastal hazard are more attributable to more frequent threshold exceedances rather than to heavier-tailed extremes. This distinction may become critical for risk-informed design, as more frequent but moderate extremes may lead to greater cumulative impacts than rare, intense events alone.

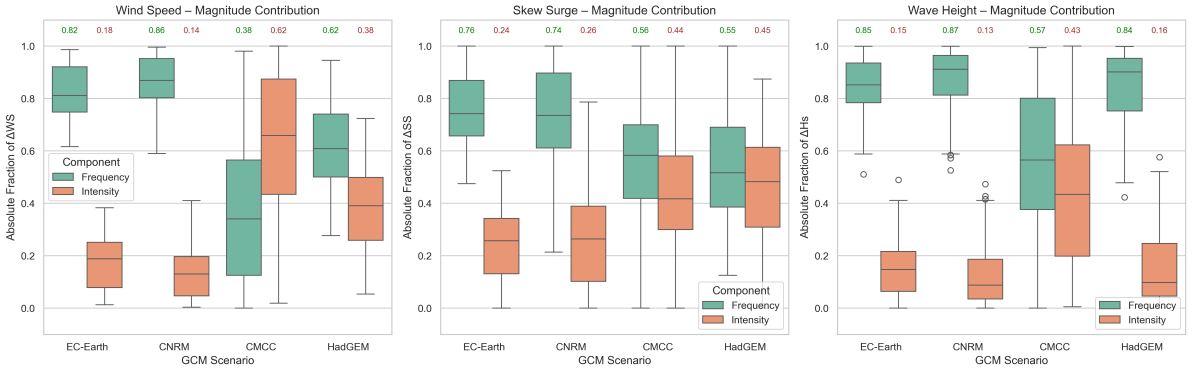

Figure 4.3: Boxplots of magnitude-normalised contributions of frequency and intensity to changes in the 100-year return level (Δz_{100}) for wind speed (WS), skew surge (SS), and significant wave height (Hs), across all GCM scenarios. Each bar represents the absolute fractional contribution of each component, computed from GPD-based tail extrapolation under fixed-threshold analysis. Values above the boxes indicate the mean contribution across all spatial points. Across most scenarios and variables, frequency dominates the change in return level, particularly in EC-Earth and CNRM, while CMCC shows a more balanced influence of frequency and intensity.

4.2.2. Shift in marginal extreme TC-induced wind, surge and wave

This subsection will elaborate on the shifts in marginal extremes based on fitted GPD distribution parameters. Unlike previous sensitivity analyses where the threshold is fixed, the result in this figure is based on an optimum threshold-RMSE fit method previously stated in Section 3.2.4. One instance of a fitted return period curve at a coastal location in Beira is presented in Figure 4.4. As elaborated in

the methodology before (see illustration in Figure 3.6), Δ is defined as the difference between STORM-GCMs' and STORM-IBTrACS magnitude at a specific return period. From this figure, we can infer the variability of the pattern across different return periods. Within the skew surge plot, for example, there is a crossover point where STORM-IBTrACS overtakes EC-Earth and CNRM magnitude once it reaches above the 2000-year return period. In contrast, the gap between each STORM variation's significant wave height is shown to be almost undistinguishable once it reaches a 200-year return period, or around 4.8 m of significant wave height, denoting depth-limited wave height in this part of the coast (deep water assumption no longer holds, and thus denotes as a limitation of this research). Although this variability is proven to be important across different return periods, for the main part of this research, the 100-year return period will still be the benchmark for attributing marginal (and later also joint) extreme shifts due to its common use in coastal protection design and risk analysis.

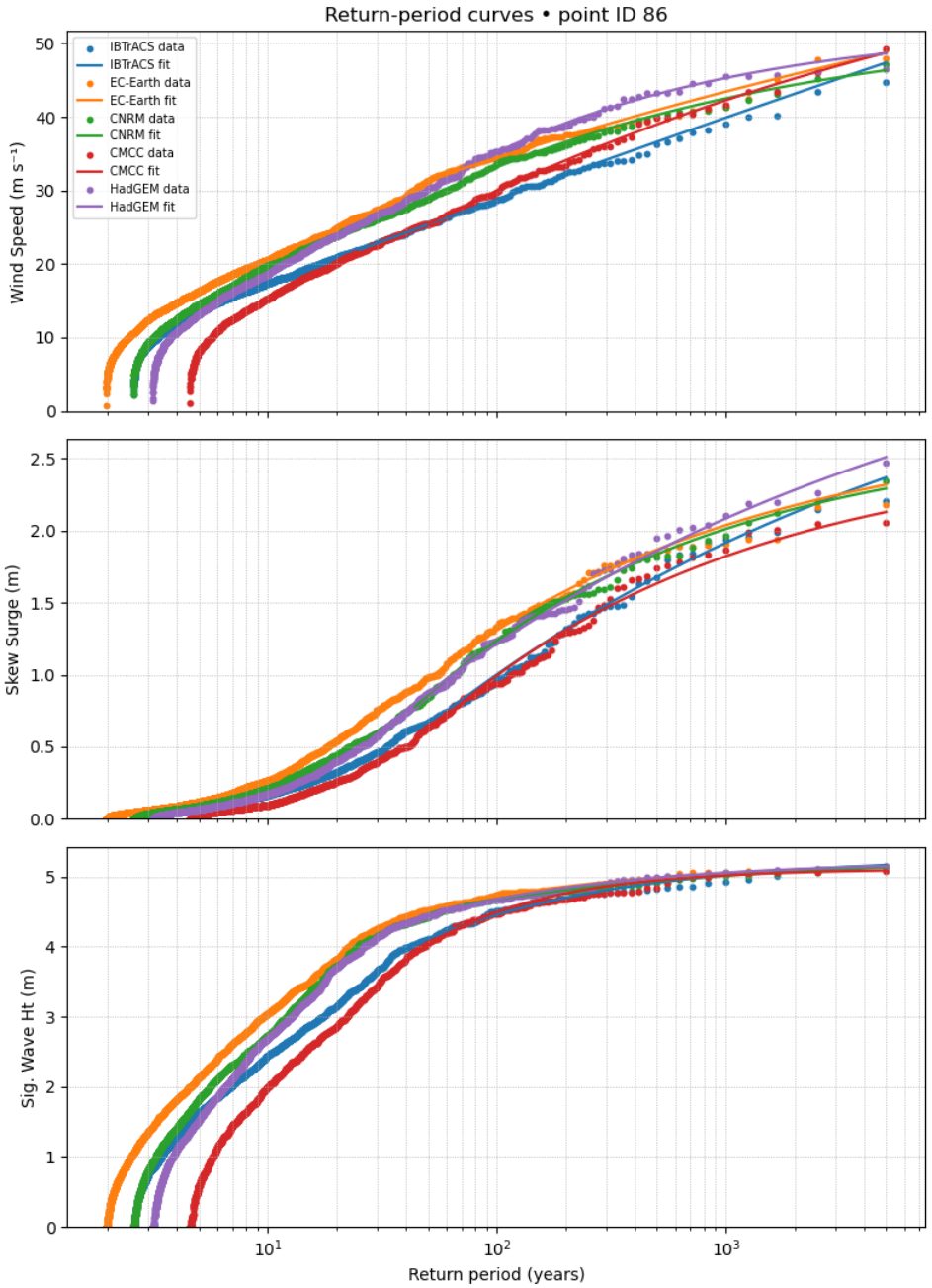

Figure 4.4: Example of fitted return period curve across each WS (top), SS (middle) and Hs (bottom) parameters at one of Beira's coastal points.

Figure 4.5 illustrates the spatial distribution and ensemble variability in the 100-year return levels difference (Δz_{100}) for wind speed, skew surge, and wave height along Sofala's coastline. The left panel maps display the ensemble median Δz_{100} at every coastal location, and the right panel plots the distribution of such values in the spatial domain as empirical kernel density estimates (KDE) for every GCM ensemble and for the combined ensemble median. Interestingly, wind speed produces greater and more spatially consistent increases than skew surge and significant wave height. The results show that the most increased wind speed extremes are found close to the central coastal areas bordering Dondo, Beira and Buzi, with ΔWS_{100} values larger than 5 m/s for the ensemble median. This finding is a reflection of higher occurrences of more intense wind speed tracks under STORM-GCMs in this specific stretch of coast, as previously shown in Figure 4.2 (from blue and green-ish colour to orange and red-ish colour), aided also by the identified dominance contribution of exceedance frequency in determining changes in extreme upper tail magnitude (Figure 4.3).

Furthermore, to explain the spatial variability of ensemble median ΔSS_{100} and ΔHs_{100} absolute magnitude, we can refer back to the physics of TC-induced surge and wave related to the bathymetric condition along the coastline (Literature review Subsection 2.2.2 and 2.2.3). As previously shown in the bathymetric map shown in Figure 2.5 and nearshore slope in 2.6, the coastal area south of Beira up to Sofala district is shallower with significantly gentler nearshore slope compared to its northern counterpart in Dondo to Marromeu and southern counterpart in Divinhe and Machanga districts. This characteristic is owing to the sediment deposition brought by the Pungwe and Buzi rivers. The effect of this characteristic is twofold: first, as the magnitude of the wind-induced surge is inversely proportional to water depth (see Equation 2.1), hence overall surge is higher in this shallow region even when forced with the same intensity of wind; secondly, the gentle slope greatly enhances the development of surge because the slower-moving water over shallow shelves cannot spread out and thus piles up along the coast. As opposed to that, the shallow bathymetry imposes a depth-limited effect on wave height, leading to a reduction in ΔHs, especially as waves near their maximum possible height for that depth. These explanations form the basis for why ΔSS tends to be higher where ΔHs is less and vice versa, as depicted in the left spatial map of Figure 4.5.

The KDE plots on the right highlight spatial inter-model variability in the projected return level changes. HadGEM, EC-Earth, and CNRM always remain at the higher end of the distribution, reflecting larger hazard shifts under these GCMs, while CMCC reflects minimal or even negative change in some places. HadGEM, despite an overall highest density at the higher end of ΔWS_{100}, still produces lower overall ΔSS_{100} and ΔHs_{100} compared to EC-Earth, likely due to less spatially distributed TC occurrences, as shown in Figure 4.1. Notably, the ensemble medians (black dashed curves) reflect a clear coast-wide increase in all three hazard metrics, although the exact magnitude differs. These spatial and probabilistic indications validate that, irrespective of the hazard attribution mechanism (wind speed, surge or wave), the Sofala coastline is projected to experience an upward shift in extreme TC-elicited storminess under future climates. This result is further supported by the ensemble-median effective return period maps in Figure 4.6, which denotes a significant forward shift in hazard: what was once a 100-year event could become as regular as probabilistically every 46 years for wind speed, 59 years for surge, and 57 years for wave height (median of ensemble median effective return period over the whole coastal points). The spatial variability of these marginal effective return periods, on the other hand, may range from 40 to 60 years for wind speed, 50 to 75 years for surge, and 35 to 75 years for wave height.

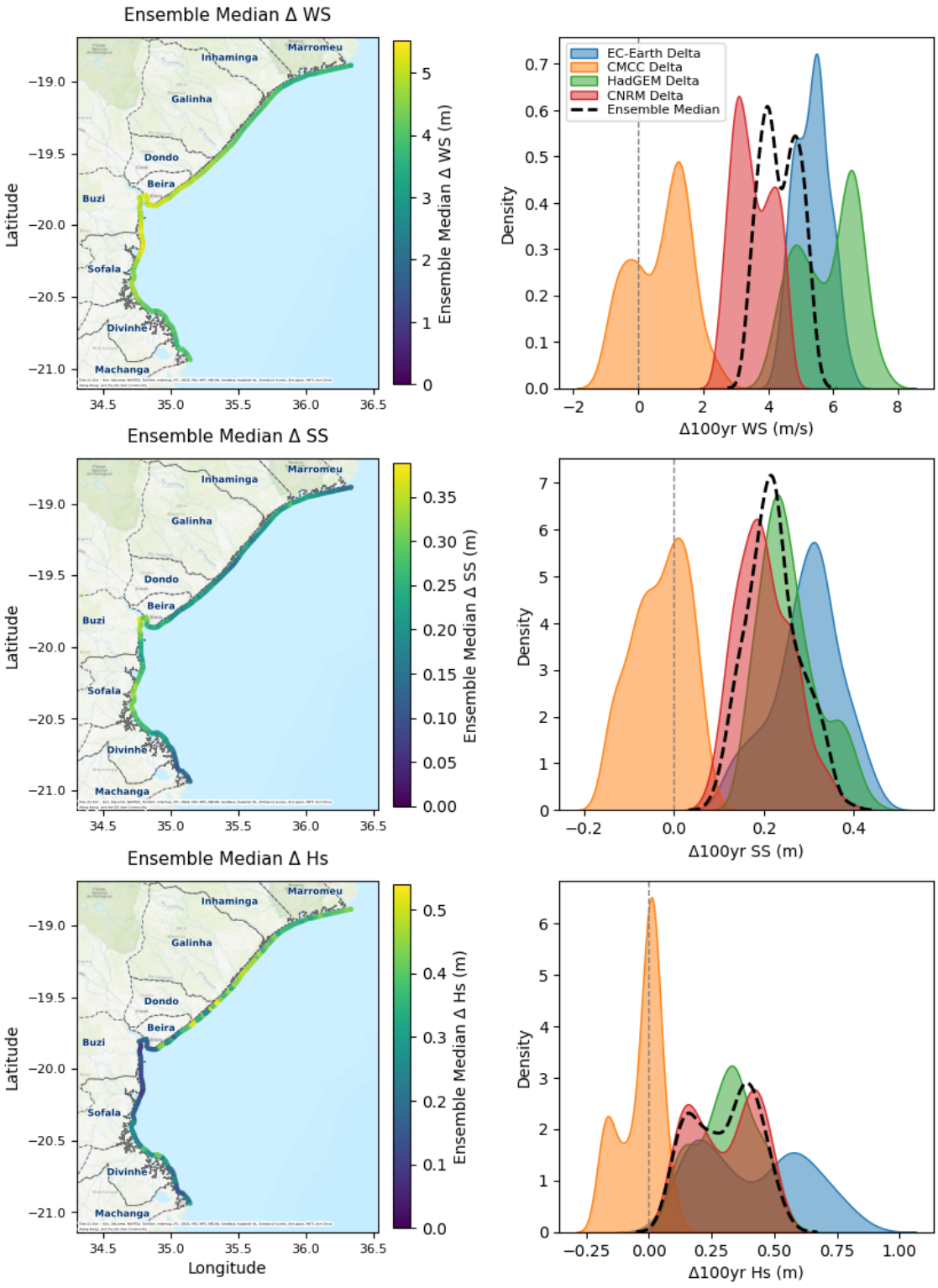

Figure 4.5: Spatial distribution (left) and ensemble kernel density estimates (right) of the change in 100-year return levels (Δz_{100}) for wind speed, skew surge, and significant wave height. Maps represent ensemble median values per coastal location, while the KDE plots show the spatial distribution of Δz_{100} across all coastal points for each GCM. Dashed black lines indicate the median across the GCM ensemble.

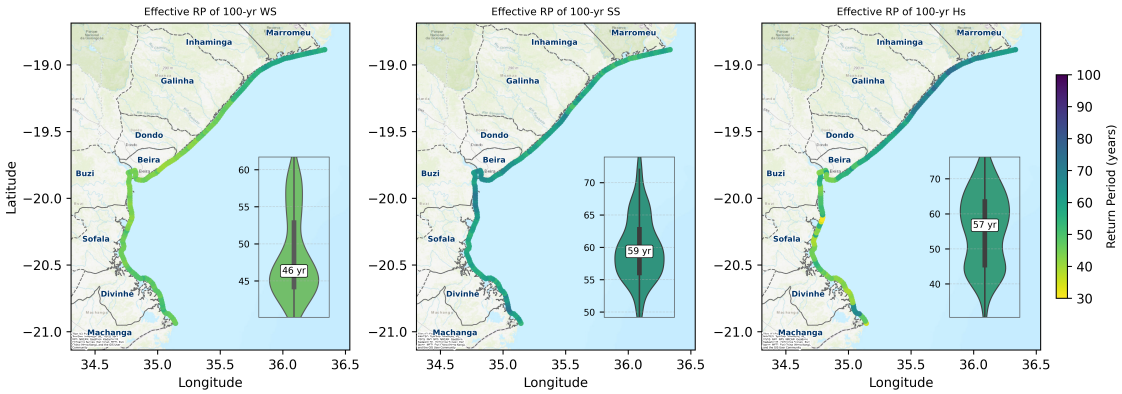

Figure 4.6: Ensemble-median effective return period (RP) maps under future climate scenarios, evaluated for historical 100-year thresholds of wind speed (left), skew surge (middle), and significant wave height (right). Insets show the ensemble distribution of the effective RP across all coastal locations.

Takeaway *for Section "Attribution of Changes in Marginal Extreme TC-Induced Wind, Surge and Wave along Sofala's coast":*
In summary, the attribution of changes in marginal extremes highlights a consistent upward shift in the 100-year return levels of TC-induced wind speed, skew surge, and wave height along the Sofala coastline, mainly driven by an increased frequency of threshold exceedances rather than by the intensity of those exceedances. This shift is most pronounced in regions exposed to higher TC occurrence under future climate scenarios, and, especially for surge and wave, is also modulated by local bathymetric conditions (higher surge yet more limited wave height at a shallower depth). Across most GCMs, wind speed exhibits the strongest and most spatially consistent increases, followed by surge and wave height, with CMCC standing out as the least impactful scenario. The ensemble-median effective return period maps also highlight the increasing risk, where future conditions will make events of a historical 100-year occurrence much more frequent, reaching a median of 45 to 60-year effective return period for each hazard. The results present strong indication that TC-induced marginal hazard extremes might become more frequent under future climate conditions. The subsequent section expands upon this description, accounting for how these changes operate against each other: the compounding behaviour of surge and wave extremes by way of bivariate attribution frameworks.

4.3. Attribution of Changes in Joint Extreme TC-Induced Surge and Wave along Sofala's coast

This section presents one of the results of Methodology $Part\ III$ "Marginal and Joint-Extreme Value Attribution", with emphasis on the joint attribution as elaborated in Subsection 3.2.4.

In addition to marginal extremes, the joint behaviour of storm surge and wave height is critical for understanding compound flooding risk along Sofala's coastline. Compound events, where both variables reach extreme values simultaneously, often lead to disproportionately higher impacts compared to isolated extremes. Although both surge and wave are similarly driven by wind, their occurrence can not be simply represented as fully dependent variables. To assess this, we analysed the pairwise dependence structure between skew surge and significant wave height using the logistic extreme value framework. This method is previously elaborated in Subsection 3.2.4; meanwhile, the theoretical basis is discussed in Subsection 2.4.2. Figure 4.7 shows an example of a bivariate threshold excess fit for a coastal point in Beira across all STORM variations. It is shown that the theoretical logistic model (denoted by coloured $h(w)$ line), driven by the fitted α value, produced a satisfactory alignment compared to the empirical angular variable density. Still, it is highly evident in most of the presented STORM variations that the theoretical fit can not fully represent the asymmetrical behaviour of the empirical density, with notable underestimation at a certain angular variable range. This finding denotes the limitation of applying a simplistic logistic model, which is characterised by a strict symmetric spectral distribution.

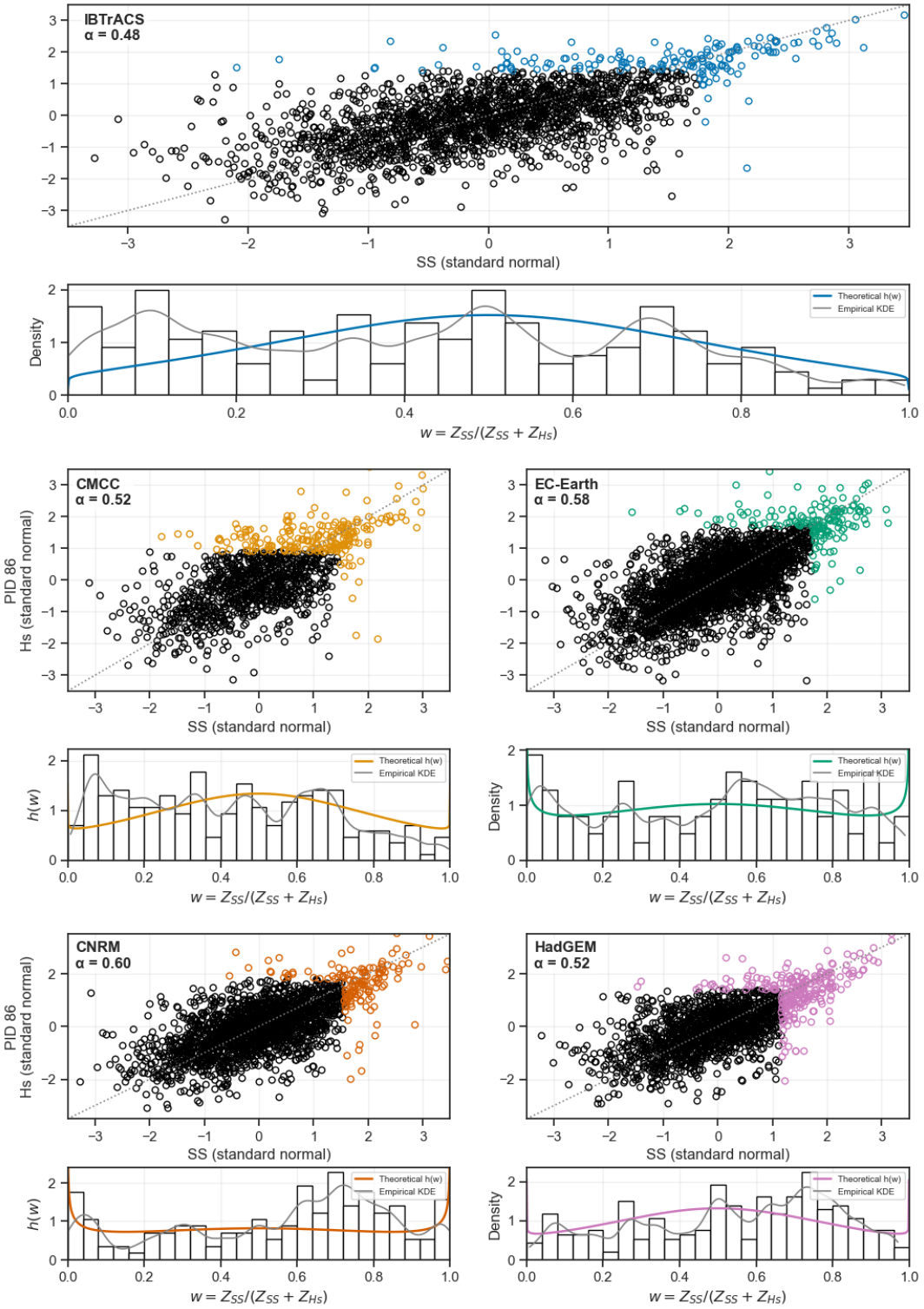

Figure 4.7: Joint–tail behaviour of skew surge (SS) and significant wave height (Hs) at one point along the Beira coastline. For each STORM variation, the upper panel displays a scatter of SS versus Hs after both variables have been transformed to standard–normal margins. Black circles denote bulk storms, whereas coloured open circles highlight *extremes*, defined as events in which *either* SS or Hs exceeds its own POT threshold on the original scale. A grey dotted line indicates the $1{:}1$ reference. The same colour is reused in the panel immediately below, which shows (i) a histogram of the angular variable $w = Z_{\mathrm{SS}}/(Z_{\mathrm{SS}} + Z_{\mathrm{Hs}})$, where $Z = 1/[-\ln(U)]$ is the unit-Fréchet transform of each marginal exceedance; (ii) a grey, data-driven kernel–density estimate; and (iii) the coloured spectral density $h(w;\alpha)$ of the fitted *logistic* model. The fitted dependence parameter α is printed in bold inside each scatter panel; smaller values of α indicate a stronger SS–Hs tail association.

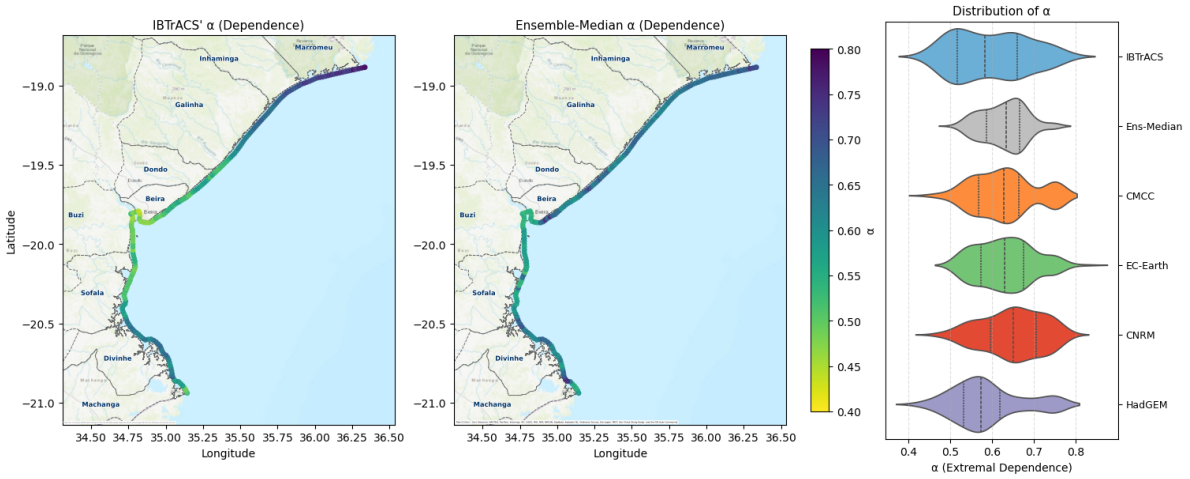

Figure 4.8: Spatial and ensemble distribution of the estimated extremal dependence parameter α between skew surge and significant wave height. Lower α values (lighter colours) indicate stronger tail dependence in the joint tail, meaning surge and wave extremes are more likely to co-occur. The left panel shows the historical baseline derived from STORM–IBTrACS, while the middle panel depicts the ensemble-median projection under future climate scenarios. The violin plots on the right summarise the spatial distribution of α values across models, highlighting variation among GCMs and shifts relative to the historical baseline. The dotted line in the violin plots denotes the quartile range 25-75 percentile, while the middle dashed line denotes the median.

Figure 4.8 presents the spatial distribution of the fitted extremal dependence parameter α, where lower values indicate stronger tail dependence—i.e., a greater tendency for extremes in both variables to co-occur. There are likely two mechanisms that drive most of the α to be no less than 0.4, or in other words, not fully dependent. Firstly, the different responses towards depth, as previously elaborated, surges are likely to accumulate in shallower regions where wave heights become more limited. Secondly, the contrasting spatial structures of wind-induced surge and wave fields likely contribute to this effect. TC-induced surge tends to exhibit a broader spatial distribution, influenced by large-scale pressure gradients and wind stress over extended areas. In contrast, TC-induced waves are more tightly coupled to the wind field structure, with the highest wave heights concentrated around the eyewall, minimal heights near the eye, and rapid decay beyond the core wind zone. This mismatch in spatial patterns limits their full dependence.

The results show a general increase in α between surge and wave height across most of the Sofala coastline (except Inhaminga and Marromeu districts), evidenced by the darker shading in the ensemble-median map, and the rightward shift in the overall density of the violin plot for most GCMs. In particular, EC-Earth, CNRM, and CMCC exhibit overall higher α than the IBTrACS baseline. Interestingly, HadGEM demonstrates a somewhat concentrated dependence around 0.5-0.6 and produces a slightly lower overall α quartile range compared to IBTrACS. Still, when we consider the ensemble median of each of the points, it becomes clear that the tail dependence of surge and wave is expected to decrease (higher α) under the future climate conditions. Spatially, the central coast around Beira, including Sofala, Buzi, Dondo, and Beira itself, exhibits the most pronounced decrease in tail dependence. This lessening of joint behaviour implies that extreme surge and wave height compound events are projected to become less synchronised.

From a physical perspective, the decrease in tail dependence under the future climate scenario can likely be associated with the depth-limited effect of wave generation. That is, as the TC wind speed becomes increasingly intense under future climate scenarios (as seen in Figure 4.2), the surge could become increasingly higher, whereas the wave height is limited to a certain height, producing less correlated surge-wave magnitude pairs. Nevertheless, this does not fully account for why the STORM-HadGEM scenario, which generates the most intense wind speeds overall, also exhibits the highest level of dependence. Other physical factors, such as TC translation speed, angle, and landfall location, as well as the fact that this analysis derives surge and wave height magnitudes from different observation locations (near the coastline for surge and in deep water for wave), may have influenced these results. Further investigation is thus needed to understand this behaviour, which is beyond the scope of this study.

Figure 4.9 further compares the historical joint return period (JRP) of 100-year storm surge and wave height with their corresponding effective JRP under future climate scenarios. The left panel illustrates the spatial distribution of historical JRPs derived from STORM–IBTrACS, showing an increasing pattern of JRP as it moves further from the Pungwe River mouth in Beira. The lowest JRP of around 150 years, as found around Buzi and Beira, indicates a more frequent co-occurrence of historical 100-year storm surges and wave heights, compared to those on Marromau's coast, which has a JRP of around 400 years. The fact that no coastal point demonstrated a JRP of exactly or at least close to 100 years implies that the TC-induced surge and wave height in this region are indeed not fully dependent, as previously explained.

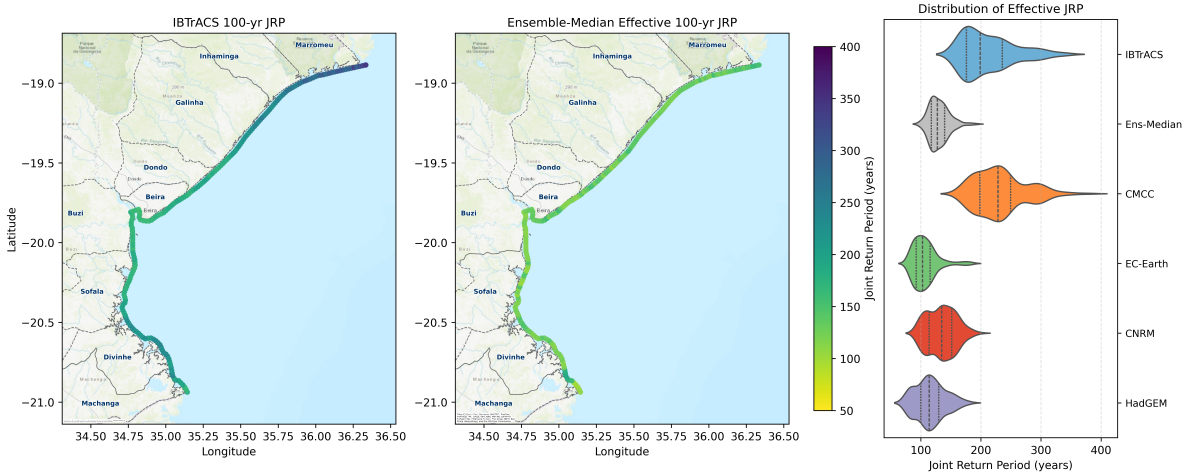

Figure 4.9: Effective joint return period (JRP) of historical 100-year skew surge and wave height extremes under future climate scenarios. The left map shows the historical JRP baseline, while the middle map presents the ensemble-median future JRP values; the right violin plots illustrate the distribution of effective JRPs across GCMs. The dotted lines within the violin show the interquartile range, while the dashed line denotes the median. Lower JRPs (lighter colour on the spatial map) indicate increased likelihood of co-occurring extremes, driven by both marginal increases and changes in dependence.

Furthermore, the ensemble-median future JRP map (middle panel) reveals a pronounced reduction in joint return periods along the entire Sofala coastline, resulting in the JRP being almost uniformly reduced to around 120 years. Notable differences are found along the northern coast, particularly in the districts of Galinha, Inhaminga, and Marromeu, where the effective JRPs plunge from 200 to 350 years to around 120 years. This indicates that what was previously considered a 1-in-100-year joint surge-wave hazard may become twice to three times as likely in the future at this stretch of coastline. The JRP changes are the least severe around Beira, with a shift from around 200 years JRP to around 120 years.

The rightmost violin plots further summarise the spatial pattern across different GCM scenarios. All future models show a distinct shift toward lower JRPs compared to the historical reference, including their ensemble median. Among them, HadGEM and EC-Earth produce the lowest ensemble medians, with some coastal locations exhibiting effective JRPs as low as 50–60 years. CNRM also demonstrates a considerable shift, though its interquartile range remains slightly broader, which suggests greater spatial variability in joint risk. In contrast, CMCC remains the least conservative scenario, with several locations retaining JRPs near the baseline IBTrACS and an overall higher interquartile range.

From these findings, an interesting notion arises. That is, despite an overall pattern of reduced joint tail dependence, we instead find an overall trend of decreasing extreme surge and wave joint return periods, which theoretically should have been the inverse of that. The contradictory trend between dependence and effective JRP, as shown in HadGEM (higher tail dependence yet lower effective JRP) and CMCC (lower tail dependence, yet still higher effective JRP), demonstrates this behaviour more specifically. To understand this, we need to refer back to the parameters that constitute the JRP in the first place, which are: extremal dependence (α), TC arrival rate (λ), as well as marginal surge and wave cumulative distribution functions (CDFs) (see Equation 3.1 and 3.2). Here, λ only acts as a normalising factor; hence, it should not be taken into consideration in JRP sensitivity. On the other

hand, the surge and wave CDFs are the result of CDF-mapping based on fitted marginal surge and wave distributions, which, as previously discussed in Subsection 4.2.1, is predominantly constituted by marginal exceedance frequency, followed by exceedance intensity. Thus, we can infer that, while dependence plays a role, the exceedance frequency and intensity shifts in the marginal surge and wave extremes remain the primary drivers of changes in compound hazard likelihood under future climate scenarios.

Takeaway *for Section "Attribution of Changes in Joint Extreme TC-Induced Surge and Wave along Sofala's coast":*

To summarise, the found ensemble-median decrease in surge–wave upper tail dependence, combined with the consistent reduction in effective joint return periods relative to the IBTrACS, consolidates the major tendency observed across all GCMs. These findings provide evidence that the likelihood of compound surge–wave extremes co-occurrence is projected to rise significantly (from around 200 years to around 120 years JRP) across most segments of the Sofala coastline, primarily due to a shift in each marginal extreme surge and wave itself, rather than their dependence structure. Due to the significant decrease in JRP, it can also be concluded that the future coastal hazard landscape in this region is shaped not only by the shift in marginal extreme surge and wave, but also by their enhanced co-occurrence. In order to easily contextualise how such compound risk escalation translates into tangible coastal impacts, the next section revisits the case of Tropical Cyclone Idai by developing a future climate storyline scenario, while preserving the actual co-occurring pattern of surge and wave.

4.4. Importance of Storminess Change and SLR in TC Idai Future Climate Storyline

As previously elaborated in the Introduction chapter, a storyline approach is conducted as a means to communicate the possible shifts of coastal flood hazard effectively. Here, TC Idai is taken as a case study given its severe presence and implications for the Sofala region. Given that no measurements of water level and wave height are available in this region, we begin the discussion of this chapter with a brief elaboration on the TC Idai hindcast results. Based on this hindcast, a probabilistically scaled future magnitude can be acquired using the fitted distribution parameters found during the marginal extreme fit (POT and GPD). By explicitly simulating both historical and future surge and wave scenarios in the SFINCS-SnapWave model, we can obtain the ΔWL (water level differences) as well as flood extent driven by shifts in future surge and wave extremes (changes in storminess) and how they compare to SLR-only and combined SLR-storminess change scenarios. Details on how this analysis is conducted are presented in Subsection 3.2.5.

4.4.1. TC Idai hindcast and scaled future surge and wave

Historical skew surge and significant wave height from TC Idai, indicated by the black line, are shown in Figure 4.10, with observation points as defined in Figure 3.5. This hindcast is produced by Delft3D-FM and HurryWave model, as previously elaborated in 3.2.5. A full spatial map of the hindcasted water level and wave is presented in Figure C.1. It can be noted from the spatial figure on the left that TC Idai track (black dashed line) made landfall at the central coast of the Beira district and caused a skew surge centred around the Pungwe River mouth, just at the southern border of the district, and decayed the further it gets from this location (also indicated by the black line in the middle plot). Inside the river mouth, the skew surge is even more pronounced, exceeding 2.5 m, which is likely due to the surge amplification effect imposed by the funnel-shaped river mouth. It is also interesting to note that, from a spatial perspective, the skew surge magnitude declined significantly at the northern Sofala's coastline compared to the southern side. This behaviour can be related to the bathymetric condition in this region, in which the nearshore slope at Dondo, Galinha, and Inhaminga is significantly steeper compared to those districts located south of Beira (see Figure 2.6 for details on nearshore slope), hence produces less surge that are piling up to the coast.

In contrast, from the bottom row plots, we can infer that the higher range of significant wave height is

instead found 1-1.5°away from the TC Idai eye-track and landfall point, which is inversely correlated to the surge spatial trend. There are at least three mechanisms involved in producing this result: the TC spatial wind field characteristic, the depth-limited effect of wave generation and the TC translation path. Firstly, as wave height is proportional to TC-induced wind speed, the spatial pattern of the TC wind field will dictate how wave height generation is distributed spatially. The spatial wind field distribution following Holland (1980) (Figure 2.12) as well as the TC-induced wave schematization (Figure 2.9) best describe this behaviour. In both, the maximum wind speed, and consequently the highest wave heights, are located at the eyewall, gradually decreasing with distance from the cyclone's eye and even markedly calmer inside the eyewall itself. Secondly, the depth-limited effect on wave generation also plays a significant role in limiting wave height at each local observation location, despite the extremely high wind speed at that location. Since the wave observation points are located at varying depths, this may slightly reduce wave height generation, particularly near the Buzi and Pungwe river mouths, close to the TC Idai landfall area, where depths are closer to -15 m MSL compared to the deeper northern points around -20 m MSL. Lastly and probably most importantly, the spatial pattern of maximum wave heights is also shaped by wave propagation and the cyclone's translation path. Since the plot reflects peak Hs regardless of timing, these maxima may have been generated earlier along the storm track and propagated away from the eye. This explains why locations slightly offset from the track, particularly in the forward right quadrant, can experience the highest Hs even without extreme local wind or bathymetric conditions.

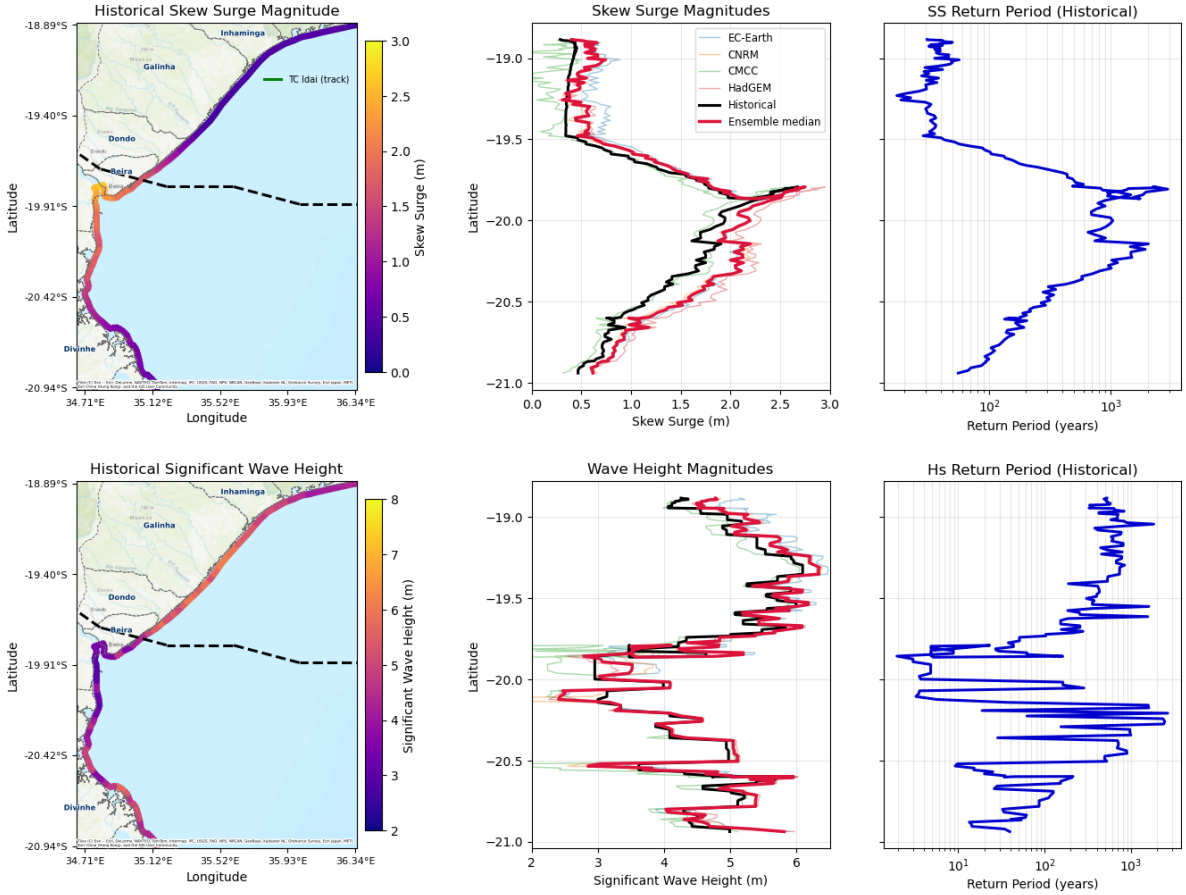

Figure 4.10: Spatial and latitudinal distribution of historical and ensemble future projections of TC Idai-induced coastal hazards along the Sofala coastline. **Top row:** (Left) Historical skew surge magnitudes mapped along coastal locations, with TC Idai's track overlaid in green. (Middle) Latitude profiles of skew surge showing historical values (black), ensemble-median future projections (red), and individual GCM members (faint lines). (Right) Log-scaled return periods (years) associated with historical skew surge magnitudes. **Bottom row:** (Left) Same as the top row, except it is now based on TC-induced significant wave height.

In terms of future projections, the red, bold line in the surge and wave panels indicates the ensemble

median of scaled TC Idai skew surge and wave height magnitude. The faint-coloured lines, on the other hand, represent each STORM-GCM scaled magnitude, which has been derived through the return period scaling of each STORM-GCM's GPD-fitted parameter. The return period at each of the coastal points is represented in the blue line in the right-most plot. From the return period plot, we can also infer that at some locations, the surge and significant wave height exceed a 1000-year return period, denoting the severity of this event. It can be noted that the ensemble median, compared to the historical case (black line), projects an overall increase in skew surge and significant wave height along the Sofala coast. This scaled magnitude is thus translated into a scaled water level and significant wave height time series along the coastline using the approach previously illustrated in Figure 4.12. One instance of the scaled time series of water level and wave height at the location in Beira where the highest surge was estimated is shown in Figure 4.11.

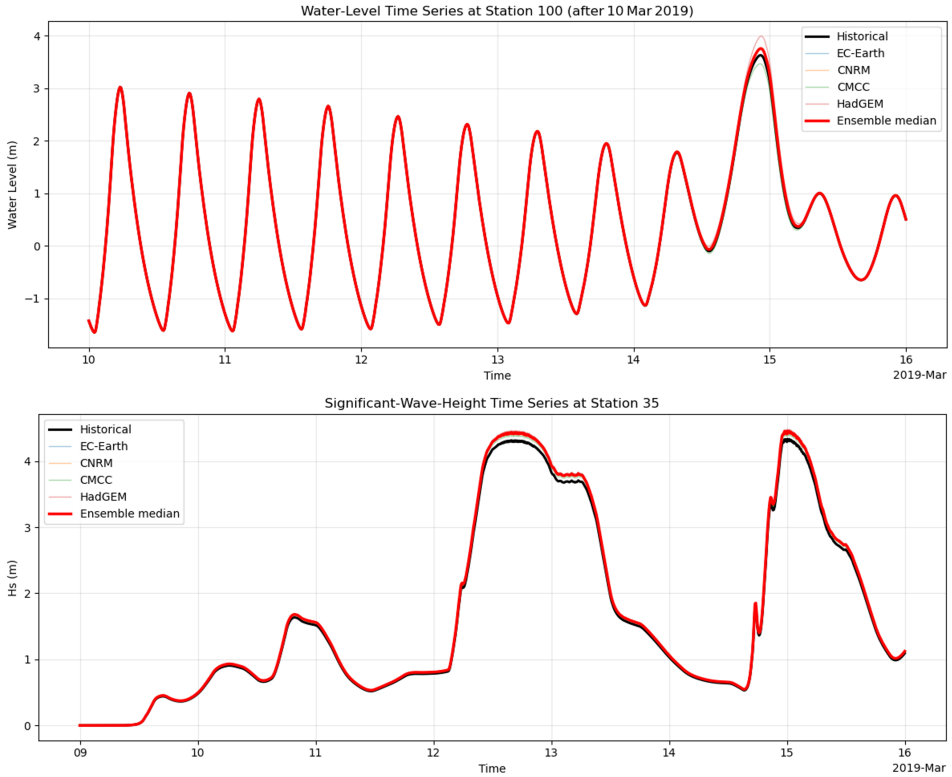

Figure 4.11: Example of scaled water level and significant wave height time series at one of the stations near Beira. The black bold solid line shows the hindcast time series, while the red one shows the scaled time series based on ensemble-median future projections. The scaled time series based on individual STORM-GCMs' statistics is shown in faint colored lines. It is important to note that SLR will be later superimposed for the future scenario's time series.

Major increases in surge are found along the districts south of Beira, specifically the Buzi and Sofala districts. Around Beira, the projected skew surge increase is limited to approximately 0.1–0.2 metres. This modest rise is attributed to the relatively small gap between the extreme tail magnitudes (exceeding 1000-year return periods) of STORM-IBTrACS and those of the STORM-GCM ensemble. In contrast to the spatial variability observed in skew surge differences, significant wave height increases are almost uniformly insignificant along the coastline, with maximum growth of around 0.5 m. It should be noted that, in the main body of this report, only the ensemble median future scenario is considered for the coming contribution analysis of storminess change into total water level and flood hazard along the Sofala coastline (Subsection 4.4.2).

However, before moving on to that discussion, we must review how the hindcast significant wave height shown earlier translates into wave-induced setup, as well as infragravity (IG) wave swash, as shown in Figure 4.12a. This combination of wave-induced water level component, also known as wave runup, is based on the result of the SFINCS-Snapwave model (1st iteration) previously elaborated in Subsection

3.2.5. A full spatial map on the produced nearshore significant wave height and infragravity wave height is presented in Figure C.2. The equivalent result under the future ensemble median scenario is shown in Figure 4.12b. The ΔTWL's contribution, i.e. the difference between future and historical wave setup and IG swash, will be shown in the following Subsection.

As shown in the figure, the highest wave runup instead occurs away from the landfall point, specifically along Divinhe's coastline. At this location, there is some sort of barrier island protecting the main Divinhe's coast, exposed closer to the peak infragravity water level as depicted in Figure C.2. Around Pungwe's river mouth (around Beira), where skew surge is the highest, the wave runup contributes an extra 0.5-0.6 m to the total water level. When we look at the relative contribution of wave setup and IG swash, we can find that most of the wave-induced water level in this region is instead modulated by IG swash. The reason for this pattern is due to the very mild nearshore slope along this coastline, as shown in Figure 2.6, which significantly reduces the cross-shore radiation stress gradient caused by wave breaking. In contrast, this mild bed slope is argued to have an almost negligible effect on IG swash (Stockdon et al. 2006). Equivalently, the steeper coast at the southmost part of Sofala hence generated the highest wave setup due to more intense wave-breaking radiation stress gradient.

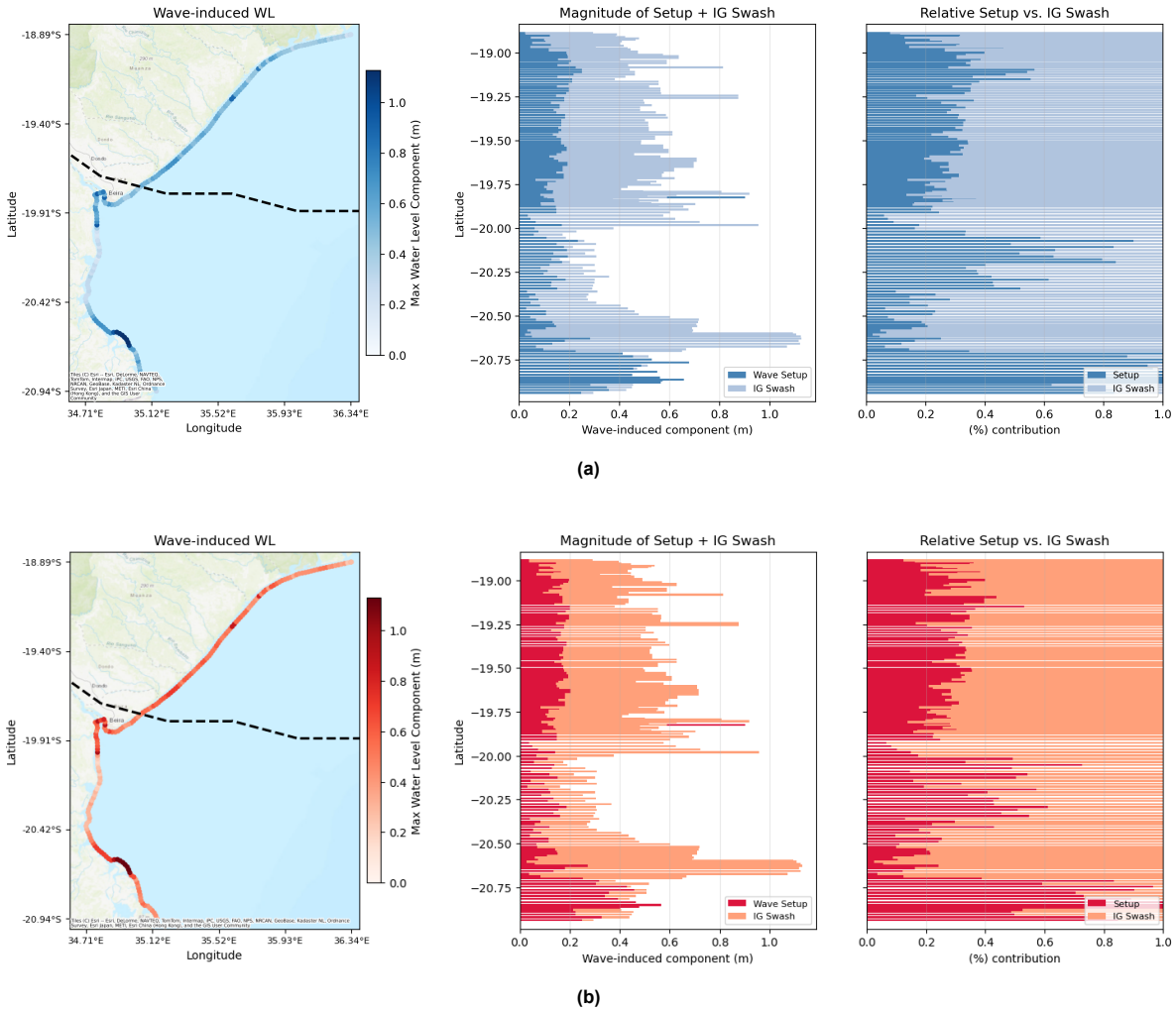

Figure 4.12: Hindcast (a) and ensemble future-scaled (b) spatial and latitudinal distribution of TC Idai hindcast's wave-induced water level along the Sofala coastline. The middle plot shows the absolute contribution of wave setup and IG swash in stacked horizontal bars, whereas the right plot shows their relative contribution.

4.4.2. Contribution of storminess change and SLR to TC Idai storyline's total water level (TWL) and flood exposure

TC Idai Storyline's ΔTWL

The total water level along the coastline comprises the combination of tide, surge, wave runup, and a sea level rise offset. Given that in this storyline scenario, the tide is assumed constant, hence, ΔTWL here refers to the sum of SLR as well as future climate skew surge and wave runup differences ($\Delta WaveRunup$ and $\Delta SkewSurge$). It is essential to note that SLR here refers to the SSP585 year 2050 magnitude, as previously elaborated in Subsection 3.1.2, with a magnitude of 0.24-0.26 m near Sofala's coastline. Figure 4.13 shows the absolute and relative contribution of each of these three components along the coast of Sofala's coastline under the TC Idai future climate storyline. From the leftmost spatial map, we can infer that the highest ΔTWL is instead found around Sofala and Divinhe district, with up to around 0.6 m difference, 0.2 meters higher than near the landfall area around Buzi and Beira districts.

In terms of contribution, it can be inferred that storminess-induced changes, represented by $\Delta WaveRunup$ and ΔSkew Surge, generally contribute less to the overall ΔTWL compared to sea-level rise (SLR), with an approximate spatial average ratio of 30:70. Overall, it can be inferred that ignoring storminess change may lead to 10-60% of the total ΔTWL. Although in certain locations storminess contributions can reach as high as 40–60%, their impact is notably lower in the most critical region—indicated by the blue dashed line—near Beira and Buzi. In this area, where the population is densest (see Figure 2.1) and skew surge reaches its peak (Figure 4.10), storminess change accounts for only about 10–40% of the total ΔTWL. At most coastal points, $\Delta WaveRunup$ is almost negligible, aligning well with the overall low magnitude of TC Idai's wave runup hindcast (as seen earlier in Figure **??**). The only region where $\Delta WaveRunup$ makes a notable contribution is in the Divinhe districts, the same area where IG swash hindcast is found to be the highest, which are characterised by a complex delta and barrier island with very sparse population.

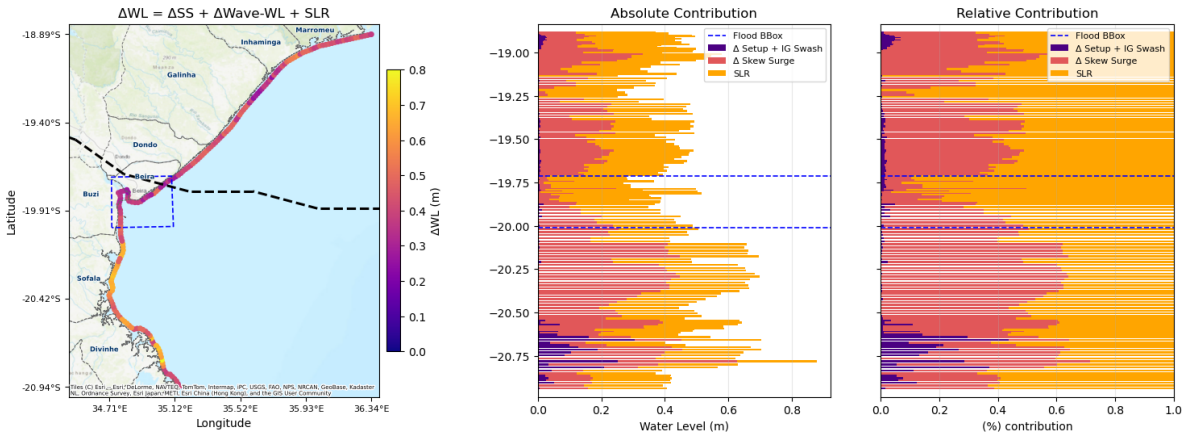

Figure 4.13: The left map shows the total ΔTWL along Sofala's coastline, meanwhile the middle and right plot (presented in stacked horizonatl bars) shows the absolute and relative $\Delta WaveRunup$ ($\Delta WaveSetup$ + $\Delta IGSwash$), $\Delta SkewSurge$ and SLR contribution to overall ΔTWL. The dashed blue box, as well as the dashed blue line border, indicate TC Idai's most impacted areas, which will be the focus of the Δ Flood hazard and Exposure discussion.

TC Idai Storyline's Δ Flood hazard and Exposure

The discussion on the importance of storminess change and SLR on shaping TC Idai's flood hazard and exposure will focus on the most impacted region around Beira and Buzi as highlighted by the blue dashed box and line in Figure 4.13. As shown in Figure 4.14, four flood hazard and exposure maps are distinguished in this discussion. Aside from the historical TC Idai flood hindcast, the other three scenarios represent isolated contributors to increased hazard: storminess change-only, SLR-only, and the total future change, which reflects the combined influence of both SLR and storminess change. The decomposition of this increase into individual contributors reveals that SLR has a more significant impact on future flood hazard expansion compared to the scenario that only considers storminess changes. In most regions, SLR-induced inundation depth gains exceed 0.3-0.5 m, whereas storminess-only re-

mains below 0.2 m. Notably, areas with significant increases due to both isolated SLR and storminess changes are localised around the inner delta and distributary mouths, as well as along Buzi's coastline. The inner delta area is historically a floodplain grassland, where tidal and surge amplification, due to a funnel-shaped river mouth, takes effect. However, it is worth noting that in the SLR-only scenario, this flooding extends even southward, covering the residential area near the highway (indicated by the dark grey line). Aside from that, flooding in the Chota area is also found to be absent in both historical and storminess change-only scenarios, in contrast to the SLR-only scenario. The total future change, on the other hand, exhibits a pattern of significantly enhanced depth and area compared to the SLR-only scenario. A notable increase in the flooded area is especially pronounced along Buzi's coastline, as well as in the inner delta of the Pungwe.

This enhanced flood hazard directly translates into elevated land-use and population exposure, as shown in Figure 4.15. The depth–area distribution (left panel) highlights that the total future scenario produces the most extensive inundation, particularly for flood depths between 0.5–1.5 metres. While SLR-only already drives a major shift from the historical case, it becomes evident that SLR alone still underestimates the full hazard. The total future curve, which includes both SLR and storminess change, consistently exceeds the SLR-only scenario across nearly all depth classes. This underestimation is further reflected in the exposure of land-use and population, in which the SLR-only scenario underestimates the flood-exposed area by up to 20 km². As seen in the middle panel, both SLR-only and total future scenarios cause a clear rise in exposed cropland and built-up area, but the total future case pushes these values even higher, particularly within the Beira district. The increased exposed area on Mangrove as well as grassland, on the other hand, is mainly comprised of the flooded area along the Buzi coastline. The same pattern holds for population exposure (right panel), where the number of flood-affected residents nearly triples under the total future scenario compared to the historical scenario, and is 50% higher than the SLR-only scenario. This population panel highlights once again that, while the storminess change-only scenario produces a minimal increase in exposed population, its effect is very apparent when it is combined with the SLR-only scenario.

Takeaway *for Section "Importance of Storminess Change and SLR in TC Idai Future Climate Storyline":*

The TC Idai hindcast highlights a surge-dominated flooding regime around Beira, where wave runup contributes minimally due to the region's very shallow and gently sloping nearshore bathymetry. Overall, the TC Idai future climate storyline reveals that sea-level rise (SLR) exerts a greater influence than storminess change in driving increases in total water level (TWL) and flood hazard across the Sofala coastline under the SSP585 2015–2050 scenario. However, the analysis clearly shows that storminess change should strictly not be overlooked: ignoring it leads to an underestimation of TWL by approximately 10–60% of the total ΔTWL, and significantly underestimates flood-exposed land use by up to 20 km² and population exposure by over 10,000 people, particularly in low-lying urban and peri-urban zones. In a broader context, the overall effect of climate change is shown to exacerbate TC Idai-like events, highlighting its significant presence that should be considered in future coastal protection design and risk mitigation.

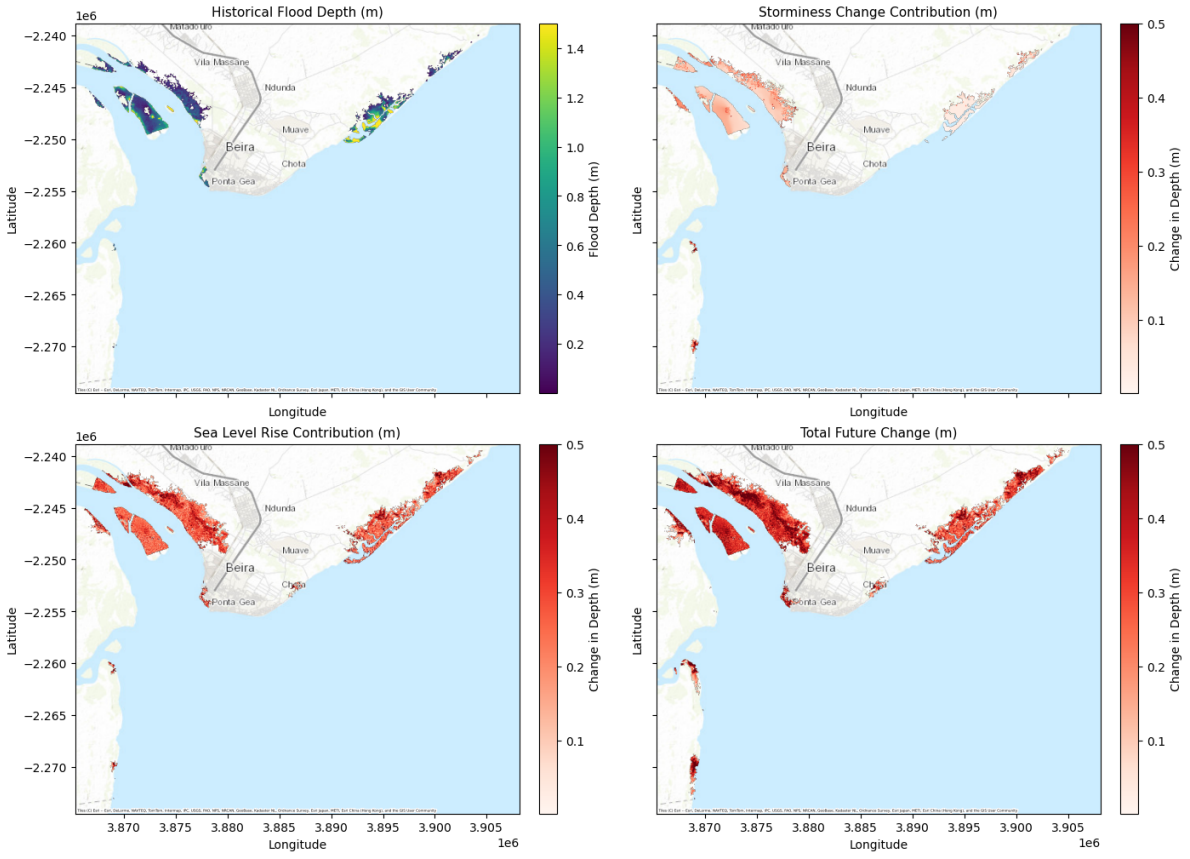

Figure 4.14: Spatial distribution of flood depth and component contributions under the TC Idai future climate storyline. The top-left panel shows the historical flood depth as simulated under present-day surge and wave forcing. The top-right panel isolates the flood depth change caused by storminess change alone (i.e., future skew surge and wave runup minus historical). The bottom-left panel shows flood depth changes driven solely by sea-level rise (SLR) under SSP585 2050 conditions. The bottom-right panel displays the total future change resulting from the combined influence of SLR and storminess change.

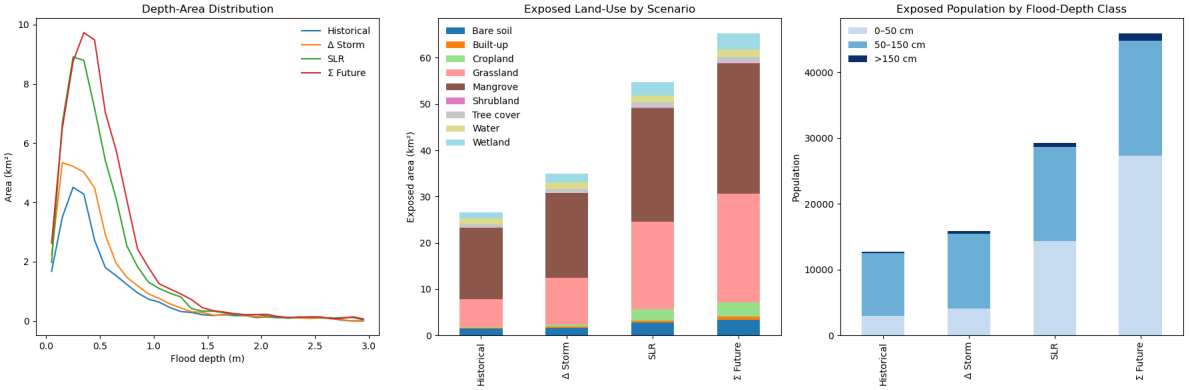

Figure 4.15: Projected change in flood exposure under TC Idai future climate storyline. The left panel shows the depth-area distribution curves for each scenario. The middle panel presents exposed land use by category. The right panel displays the population exposed by flood depth class.

5
Discussion

5.1. Research Implication

This section presents research implications derived from the key takeaway presented at each section of the previous chapter.

5.1.1. Implications of TC Occurrence and Intensity Variability in the Mozambique Channel

As elaborated in Section 4.1, the observed spatial and inter-model variability in synthetic TC occurrence and intensity across the Mozambique Channel presents a critical implication for regional risk assessment. Firstly, EC-Earth and CNRM show increased nearshore TC occurrences, while CMCC and HadGEM indicate lower or stable rates, highlighting the divides over future TC landfall trend estimates in the region. Still, when looking at TC intensities, it is clearly agreed that all future GCMs predicted a lower decrease in the tropical depression track, with a heightened relative frequency of tropical storms or higher category tracks. In the sense of general wind-induced hazards, these findings suggest that while the number of landfalling cyclones remains uncertain, the potential impact per event is expected to grow, with stronger storms becoming more common. This highlights the need for improving cyclone forecasts in the Mozambique Channel so that both the TC strength and landfall location (or TC movement in general) can be predicted more reliably to support early warning and disaster preparation.

5.1.2. Implications of Changes in Marginal Wind, Surge, and Wave Extremes

While the previous subsection focused on general changes in TC occurrence and intensity, the implications discussed here relate more specifically to the concept of reliability against extreme TC-induced wind, surge, and wave loads. This includes, for example, the structural reliability of buildings facing intense wind and the capacity of flood defences to withstand surge and wave impacts under a certain level. As discussed in Section 4.2, the projected increase in 100-year return levels for TC-induced wind speed, surge, and wave height implies that coastal infrastructure standards based on historical design thresholds may become outdated in the near future. Additionally, considering that the historical 100-year return levels are now effectively reduced to as low as a 45-60 year return period event, it necessitates an even greater need to update the design code based on future-facing EVA models. Moreover, the finding on how these return levels are more sensitive to *exceedance frequency* (i.e., how often extremes occur) than the *exceedance intensity* (i.e., how extreme they are when they occur) indicates how coastal infrastructure design should take into account structural integrity against more frequent but moderate extreme event, not just rare, extremely high magnitude event. Additionally, the spatially varying response, driven by local bathymetry, calls for site-specific design thresholds rather than uniform national or regional standards, especially in rapidly growing coastal areas like Beira.

5.1.3. Implications of Joint Surge–Wave Extremes under Future Climate Conditions

The decline in joint return periods for high wave and surge events (from around 200 years to around 120 years JRP), as elaborated in Section 4.3, implies that compound surge and wave extremes will be more frequent, posing a serious challenge to the design of infrastructure. Even when the tail depen-

dence between surge and wave is slightly weaker, the rise in joint extremes implies that structures built on the historical joint probabilities (or even isolating only to the marginal one) are under-designed. This emphasises the need to move beyond univariate levels of safety and incorporate future climate joint exceedance criteria into coastal defence codes. In port areas like Beira, for example, the breakwater design must consider a higher probability of combined surge and wave loading. Exclusion of these compound effects may result in overly conservative overtopping rates, greater structural fatigue, reduced stability, and reduced protection lifespans (Mares-Nasarre et al. 2024). Future-proofing coastal infrastructure, therefore, requires that joint hazard analysis, on the basis of bivariate return periods and probabilistic load combinations, be built into design and policy structures.

5.1.4. Implications of Storminess and Sea-Level Rise in Future TC Events

The TC Idai future climate storylines shown in Section 4.4 reveal that, while sea-level rise (SLR) is the dominant driver of increased total water level and flood hazard, storminess changes (more specifically, future climate-scaled surge and wave runup) also contribute significantly. The use of SLR projections alone is shown to underestimate flood risk, especially in densely populated locations like Beira, where a slight shift in dynamic water level induced by surge and wave runup significantly affects overall flood hazard and exposure. This finding has direct implications for flood risk mitigation strategies and the design of coastal infrastructure. Failure to consider the effects of storminess change can lead to a severe underestimation of flood exposure, which projects a false view of existing resilience, and potentially compromise the efficacy of coastal defences.

5.2. Research Contribution

To date, this study is the first to explore the effect of climate change on TC-induced surges and waves at a regional scale in Mozambique, specifically in the Sofala region. Grossmann-Matheson et al. (2024a) has previously presented global changes in TC-induced wave height under a future climate scenario; however, it focuses solely on the ocean's deep-water location. Muis et al. (2023) presented changes in extreme surge along the global coastline under future climate scenarios by employing CMIP6 HighResMIP explicitly; however, it has not yet taken into account more intense TC effects. Although these previous studies have suggested potential increases in surge and wave climate near the coast of Sofala under 2015-2050 climate conditions, this study confirms these trends more specifically by focusing on both TC-induced surge and wave changes at a more detailed regional scale. This study has showcased a better understanding towards the spatial variability of extreme wind, wave, and surge along Sofala's coastline by taking into account the compounded effects of intensity, frequency, dependence, and their interaction with local bathymetry.

Building upon Goulart et al. (2025)'s study, which has nicely demonstrated the potential severity of considering the SLR scenario in the TC Idai counterfactual storyline, this study doubles down on what if an additional future climate-scaled TC Idai surge and wave is considered. With this storyline medium, the contribution of each and combined storminess change and SLR to the total water level and resulting flood hazard can be distinguished. This approach is taken as an alternative to comparing SLR to an assumed 100-year return period surge differences presented by Marsooli et al. (2019)'s study. By preserving the statistical and physical coherence of the historical TC Idai, it provides a realistic event-based narrative that is easier for stakeholders and local decision-makers to understand.

As this study employed an open-source STORM dataset for both current and future climate, the methodology used in this study can thus be replicated elsewhere, especially in those locations where TC is abundant. It is essential to note, however, that the resulting message may vary from location to location. Unlike in tide-dominated Sofala's coast, storminess change may dominate over SLR or, in contrast, be so small that it becomes negligible. As a hypothetical example, in the Hernani coast in the Philippines, TC Haiyan's (2013) future climate storyline might reveal domination of storminess change over SLR, mainly driven by wave-runup, due to the wave-dominated landscape of the coastal area (Leijnse et al. 2021). Using a global-scale study, such as those presented by Grossmann-Matheson et al. (2024a) and Muis et al. (2023), is thus useful as a first-order estimate, especially when combined with knowledge of morphodynamic and hydrodynamic characteristics of the location of interest.

5.3. Research Limitation I: Climate Uncertainties

5.3.1. Uncertainties from different synthetic tropical cyclone models

In this study, the STORM dataset is employed as a basis for representing the current and future climate conditions of TC around the Mozambique Channel. However, as elaborated earlier in Subsection 2.3.1, other state-of-the-art global synthetic tropical datasets also exist: the MIT model (Emanuel et al. 2006; Emanuel 2008) and the Columbia HAZard model (CHAZ) (Lee et al. 2018). Aside from employing a comparable historical track-based (such as IBTrACS) Monte Carlo framework, both the MIT model (Emanuel et al. 2006; Emanuel 2008) and the Columbia HAZard model (CHAZ) (Lee et al. 2018) incorporate statistical-dynamical approaches that simulate storm structure and evolution using large-scale environmental inputs from ERA5 or GCMs. In contrast, the STORM model also uses ERA5 as input but follows a fully statistical approach, generating synthetic TCs by resampling and adjusting historical storm properties without explicitly modelling their dynamical evolution. Future climate scenarios in STORM, on the other hand, are constructed by applying delta changes derived from high-resolution GCM simulations to key storm variables such as intensity, frequency, and track characteristics. Well-known studies employing this statistical-dynamical MIT model for future TC-induced storm surge attribution are presented by the Princeton University research group (Lin et al. 2012; Marsooli et al. 2019; Gori et al. 2022).

Under current climate conditions, Meiler et al. (2022) demonstrated the uncertainties of these three global synthetic tropical cyclone datasets (STORM, MIT, and CHAZ) to wind-induced risk, revealing variable estimates in the upper tail distribution in the Southern Hemisphere region (including the South-west Indian Ocean and South-west Pacific Ocean). This variability is even more pronounced under future climate conditions, as demonstrated in Meiler et al. (2025)'s study. In this study, STORM exhibits the highest overall densities of increased risk under future climate conditions by 2050, indicating more frequent higher-to-moderate TC intensity events, while MIT shows a broader distribution, reflecting greater variability in intensity. It is currently unclear which of these three synthetic tropical cyclone models produced the most reliable estimate of current and future TC conditions, either globally or more regionally specific. Hence, one alternative is instead to embrace the uncertainties in the same way as intermodel variability introduced by different GCMs. These uncertainties have not yet been considered and thus should be viewed as recommendations for future direction following this research.

5.3.2. Uncertainties introduced by GCMs intermodel variability

As explained in the Subsection 3.1.1, the ensemble median of the intermodel GCMs approach is taken as a representative future climate condition. In a similar fashion, the median of the 2050 SLR uncertainty range (Figure 3.2) is used to represent future sea level rise, neglecting the range of uncertainty under the same SSP585 scenario. This procedure is motivated by the absence of historical TC tracks generated by each GCM in the STORM dataset, negating the possibility of a performance-based weighted ensemble approach as employed by Gori et al. (2022). The assumption used in this study is thus that all GCMs hold equal performance in representing the real-world behaviour of tropical cyclone genesis, occurrences, movement and intensity. Since the dataset includes only four HighRes-MIP GCMs, the spread of projected outcomes, thus the estimated uncertainty range, is likely less variable than it would be if a larger set of models were used. As shown in Figure 4.6 and 4.9, for example, the ensemble median will mostly closely resembles the higher EC-Earth, HadGEM, and CNRM scenario compared to lower-intensity CMCC, as if it acts like a negative outlier. Simulation of additional synthetic tropical cyclone datasets, such as MIT and CHAZ, which utilise a more variable number of GCM variations, is thus becoming increasingly necessary. Further study should therefore not only extend the same methodology using the MIT and CHAZ datasets, but also further develop a multi-method ensemble to assess the robustness and variability of different synthetic tropical cyclone methods across different GCMs, just as showcased in the community-driven framework of global wave climate scenarios (Morim et al. 2019).

5.3.3. Emission scenarios uncertainties

This study's limitation on under-representing future climate uncertainty does not end there. As noted in the research underlying the STORM-GCMs dataset (Bloemendaal et al. 2022), the difference in deviation between SSP5-85 and the lower emission scenarios is almost negligible before the 2050 period. However, how these small deviations impacted the difference in TC-induced surge and wave remains

a significant question mark. As the STORM source code is openly available, a synthetic tropical cyclone dataset covering other emission scenarios can be constructed and later used as input for an equivalent surge and wave modelling framework, introducing TC-induced surge and wave variability across multiple emission scenarios. The corresponding sea-level rise (SLR) rates under different emission scenarios, as shown in Figure 3.2, can likewise be incorporated into the hydrodynamic model to represent future climate conditions across emission scenarios.

5.3.4. Aleatory uncertainties in STORM dataset

As demonstrated in the Appendix D, specifically in Figure D.1, a different subset of the 1000-year STORM dataset is found to produce significantly variable 100-year WS, SS, and Hs return levels. This uncertainty is found to be very problematic, as the order of STORM variations that produce the higher or lower return level can be swapped between one 1000-year subset and another. This issue is also highlighted in a recent study by Meiler et al. (2025), denoting that a different sample of a 1000-year STORM subset could result in divergence of wind-induced risk. The cause of this is argued to be one of the consequences of the fully statistical approach used in STORM, which exhibits highly sensitive sampling that is unable to capture natural variability inherently. These uncertainties are found to be less evident in a statistical-dynamical synthetic tropical cyclone model, such as MIT and CHAZ (Meiler et al. 2025). In our study, it is thus decided to fully employ the first five out of the ten 1000-year subsets of STORM (the first 5000 years out of 10,000 years of STORM).

As presented in the Figure D.2, it has been shown that the 100-year WS, SS, and Hs return levels across all STORM variations have converged as more subsets are introduced. Still, due to time limitations, it is currently unknown how the remaining 5000 years of the set that are not simulated in this study will influence the return level uncertainty across various return periods. We expect that adding the remaining not-yet-simulated 5000 years subsets will not have a significant effect on the marginal and joint attribution that are performed in Section 4.2 and 4.3, as it is based on a 100-year return level that has been shown to converge. However, as depicted in the TC Idai hindcast (see Figure 4.10), the highest surge and wave are found to be associated with a more than 1000-year return period, which is shown in Figure D.3 not to be a converged return level. Thus, we acknowledge that unexplored aleatory uncertainty corresponds to this upper tail return level as one of the key limitations in the future scaling of TC Idai surge and wave maximum magnitude and timeseries.

5.4. Research Limitation II: Hydrodynamic Model Application

5.4.1. Absence of hydrodynamic model validation and the use of globally available digital elevation model

As stated earlier in the Research Scope (Section 1.5), this study does not incorporate hydrodynamic model calibration and validation using observation data (water level and wave time series) during a TC event, as such data are rarely available. Although the focus of this study lies on the relative shifts in patterns under near-future climate conditions rather than on precise magnitude estimates, the lack of validation may still affect the reliability of surge and wave outputs, especially in locations where local topographic or bathymetric features strongly influence hydrodynamic behaviour. While all scenarios are treated with the same non-validated model setup, thereby allowing relative differences between climate scenarios to be compared consistently, this approach still introduces uncertainty related to the range of unknown model configurations. Future work should either consider this uncertainty or include a greater effort in model validation, e.g., using an altimetry dataset for wave validation or consulting with local government.

Aligning with this limitation, the use of globally available GEBCO and Delta-DTM bathymetry also highlights the possible inaccuracy, especially in representing the TC Idai flood hazard storyline. As demonstrated by Parodi et al. (2020) in a small island developing state case study, the variation of globally available topography and bathymetry products could contribute to around 30% of total flood hazard epistemic uncertainties in this region. Epistemic uncertainties are uncertainties driven by imperfect knowledge or a lack of data (Uusitalo et al. 2015), which is also relevant to the Sofala case study in Mozambique. Future work should also ensure that this uncertainty doesn't affect the overall trend observed in both current and future climate conditions. One possible alternative is to adopt an already developed topobathy dataset, which combines direct measurement and an adjusted global topobathy

dataset, especially around Beira, used in Deltares (2021) report. Within the same report, an altimetry-based wave model validation is also presented, which may be replicated for HurryWave model calibration.

5.4.2. Ignored physicial parameters

For the probabilistic-based attribution component of this study (Objective A), surge and wave dynamics are modelled separately using Delft3D-FM and HurryWave, without simulating the non-linear interactions between wave, current, and water level (particularly important in shallow coastal areas). A similar approach is used in Marcos et al. (2019). This simplification neglects wave setup and other coupled processes that may significantly influence total water levels nearshore. Although this approach enables the simulation of thousands of synthetic TC events in a computationally efficient manner, as argued before in Subsection 2.3.3, it may lead to underestimation of peak water levels in areas where such interactions are known to be significant. In contrast, the storyline-based analysis (Objective B), which includes TC Idai hindcast and future climate storyline, incorporates these non-linear effects more explicitly using the coupled SFINCS-SnapWave model. Future work, especially those replicating the methodology used in this study in a wave-dominated region, could improve the accuracy of probabilistic surge and wave projections by incorporating dynamic coupling between water level and spectral wave models, or by applying calibrated surrogate models trained on fully coupled simulations to approximate wave–surge interactions at lower computational cost. A sanity test can be conducted to determine whether the wave can be fully decoupled or not by simulating samples of varying TC synthetic tracks using both coupled and separated water level–wave model setups, and subsequently comparing the two, as performed by Lin et al. (2012).

Moreover, as stated earlier in the Subsection 4.2.2 and illustrated in Figure 4.4, the HurryWave's observation points, which are assumed to always fall within deep water conditions, are instead showing an undesirable depth-limited effect, especially above the 200-year return period mark. As previously elaborated in Subsection 2.3.3, HurryWave is designed for deep-water applications, as it cannot incorporate non-stationary water levels into its simulations. When depth-limited effects occur, the wave transformation is no longer representative of true deep-water conditions, leading to potential underestimation of extreme wave heights. This limitation could affect the accuracy of climate attribution for extreme wave events beyond the 100-year return period, with no exception to the TC Idai storyline, which is showcased to exceed a 1000-year event in some locations (Figure 4.10). Bringing the wave observation to an even deeper location (e.g., -30 m) can be an alternative approach to overcoming this issue in future studies. Other notable simplifications of hydrodynamic physical parameters, especially within the application of SFINCS-SnapWave model in the storyline approach, include: 1) ignored morphological processes such as severe coastal dune erosion, which is stated to be present along the coast of Beira during the TC Idai event (Deltares 2021), 2) assumed zero river discharge, which causes underestimation in backwater effect, especially along the Buzi and Pungwe river, 3) assumed uniform friction over all the sea and water bodies, even though mangrove is found to be present on the edge of the Buzi and Pungwe river mouth.

5.4.3. Ignored pluvial, fluvial, and wind hazard

Lastly, it is imperative to note that the TC-induced hazard, especially around the Mozambique region, is often also characterised by torrential rain and, consequently, increased pluvial and fluvial hazard. TC Idai, which is used as a case study for the storyline approach, showcased these compound coastal-fluvial-pluvial hazard behaviours, with fluvial contributing to the largest flooded area, followed by coastal and pluvial forcing (Eilander et al. 2023a). Moreover, wind hazard, which might inherently damage buildings and crops, as demonstrated by Steinmann et al. (2023), should also not be ignored. All of these fluvial, pluvial and direct wind hazards are excluded in this study, which leaves a huge gap in the understanding of the full potential coastal flood hazard in the Sofala region under future climate conditions.

One alternative for bridging the fluvial and pluvial gap is to employ the Interagency Performance Evaluation Task Force Rainfall Analysis method (IPET 2006), which quantifies rainfall based on pressure deficit and spatial variability along the TC radius. Due to its simplicity, this approach is feasible for use alongside the STORM dataset (and Holland1980 wind model), although it assumes constant rainfall rates within the TC storm and ignores asymmetry or rainfall bands (Nederhoff et al. 2024). Another ap-

proach that is more physically sophisticated and complex is the Tropical Cyclone Rainfall (TCR) model developed by Zhu et al. (2013), which is designed to fit well within the MIT synthetic tropical models (Emanuel et al. 2006; Emanuel 2008). One study, which delves into the future joint rainfall-storm surge hazard, is presented by Gori et al. (2022). As for the direct wind hazard, a wind damage and risk model such as CLIMADA (CLIMate ADAptation) (Kropf et al. 2022) can be adopted. This model has previously been used for the TC Idai case study in Steinmann et al. (2023), and even at a greater regional and global extent as presented by Meiler et al. (2022).

Future studies may further extend the complexity of the model and the attribution of joint TC-induced surge and wave hazards under future climate scenarios presented in this study by also introducing pluvial and fluvial forcing while assessing direct wind damage. Incorporating these additional forcings would require a fully multivariate framework, but doing so would offer a more comprehensive understanding of TC-induced compound flood risks, although at the expense of increased computational demand.

6

Conclusion & Recommendation

6.1. Conclusion

Reducing flood hazard effectively depends on learning from past events to understand the risks and vulnerabilities involved; however, because conditions and hazard patterns can change over time, it is also crucial to consider how these hazards might evolve. These hazards, particularly in TC-prone coastal regions like Sofala province, involve TC-induced wind, surge and wave, or what is often summarised as storminess. Despite signals of changing TC-induced storm characteristics under future climate scenarios from various global-scale studies, no study to date has explicitly assessed how storminess changes would translate into future total water levels and flood hazard at a finer regional scale along the Sofala coastline. In contrast, studies that focus solely on SLR effects risk considerably underestimating future flood hazards by neglecting the dynamic contributions of storms. Utilising the STORM dataset, this study has revealed the extent of near-future (up to year 2050) storminess change in the Sofala region (*Objective A*) and its relative importance compared to sea level rise (*Objective B*). The key findings of this study are concluded below by directly addressing the formulated research questions.

Objective A:

To quantify the change in tropical cyclone-induced storminess—wind, surge, and wave—at a regional scale under future climate scenarios.

- **Q1. What are the marginal changes in wind, wave, and surge hazards in terms of intensity and frequency?**

  Projected ensemble median changes in tropical cyclone (TC)-induced hazards along the Sofala coast reveal a clear upward shift in the 100-year return levels for wind speed, skew surge, and significant wave height. Wind speed exhibits the most consistent and spatially extensive increase, as opposed to a more spatially variable surge and wave increase, owing to the non-linear interaction of surge and wave with the bathymetric condition. These upward shifts in storminess are found to be statistically driven mainly by exceedance frequency (i.e., how often extremes occur) rather than exceedance intensity (i.e., how extreme they are when they occur). As such, these projected hazard shifts significantly reduce the effective return periods of the current 100-year TC-induced wind, surge, and wave events to an average of 45-60 years. This finding thus exemplifies the need to ensure the reliability of coastal infrastructure design to withstand more frequent extreme events, rather than just rare, extremely high-magnitude ones.

- **Q2. What are the projected changes in joint wave–surge hazard under future climate conditions?**

  Joint surge–wave extremes are projected to become significantly more frequent under future climate scenarios. Despite a general slight decrease in upper tail dependence (i.e., weaker extremal co-occurrence), the effective joint return period (JRP) of historical 100-year surge and wave pairs decreases from around 200–400 years to 120 years on average. This statistical paradox arises because the primary drivers of JRP reduction are the shifts in frequency and magnitude of each marginal surge and wave distribution. Thus, even with reduced dependence, the compound hazard still becomes more likely. This emphasises the need to move beyond univariate marginal

levels of safety and incorporate future climate joint exceedance criteria into coastal infrastructure codes.

Objective B:

To assess the contribution of storminess changes, relative to SLR, to future TC-induced coastal flood hazard using a probabilistic-scaled future event and storyline-based approach.

- **Q1. To what extent do storminess changes amplify total water levels under future climate conditions, relative to sea level rise?**

  Using the TC Idai future climate storyline, the combined changes in storm-induced surge and wave runup result in a modest yet spatially variable increase in total water levels (TWL) along the Sofala coast. On average, sea-level rise (SLR) accounts for about 60–90% of the projected increase in TWL, while storminess-related changes contribute the remaining 10–40%. In densely populated areas such as Beira and Buzi, where flood risk is most critical, the storminess share is closer to 10–30%, while it can reach up to 40–60% in less populated southern districts like Divinhe. It is important to note that in this region, the depth-limited wave response in very dissipative coastal zones dampens the contribution of wave-induced components, reinforcing the dominance of surge and SLR in these regions. However, such a finding cannot be generalised to other coastal regions, especially where wave-induced water levels are more abundant.

- **Q2. How does the inclusion of projected storminess change and sea level rise modify the spatial patterns of flood extent and depth in the storyline-based event?**

  The future flood hazard landscape under TC Idai-like conditions becomes substantially more severe when both SLR and storminess changes are considered. While SLR alone significantly expands inundation (especially in low-lying deltaic zones and around Beira's urban core), the combined scenario increases flood extent and depth even further, exposing an additional 20 km^2 of built-up and agricultural land and over 10,000 more residents to flooding. The flood depth–area distribution indicates a shift towards deeper flooding (0.5–1.5 m) under the combined scenario, which is underestimated by SLR-only projections. This clearly demonstrates that storminess change, though secondary in magnitude, plays a decisive role in amplifying compound flood impacts when interacting with sea level rise, and thus should not be ignored in the development of future coastal protection design and risk mitigation strategies.

6.2. Future Research Recommendation

Building on the findings and limitations of this study, the following directions are proposed to guide future research, especially to improve further the understanding and modelling of current and future tropical cyclone (TC)-induced coastal flood hazards in Mozambique and similar regions:

- **Extend the analysis using other synthetic TC models and emission scenarios.** While this study uses the STORM dataset, future work should also incorporate alternative synthetic TC datasets such as the MIT model or CHAZ to account for structural differences in cyclone generation and track behaviour. These datasets offer different assumptions and additional dynamical processes, which are valuable for assessing uncertainty. Furthermore, given the aleatory uncertainty present in the STORM dataset, it is also suggested that future studies incorporate the full 10,000-year synthetic track dataset to encompass the entire range of TC variability required in a specific region. Additionally, exploring a wider range of emission scenarios (e.g., SSP2–4.5, SSP1–2.6) will also allow the mapping of adaptation thresholds under multiple climate pathways rather than focusing solely on SSP5–8.5.
- **Improve hydrodynamic model validation and parametrisation** To reduce epistemic uncertainty, future studies should incorporate available observations, such as altimetry or in situ tide/wave data, for model validation, especially during past TC events. Moreover, improved representation of physical parameters, such as more accurate bathymetry, dune or coastal defence elevation, and topography, is necessary. This also includes spatially variable friction coefficients (e.g., mangroves, settlement) and non-zero river discharge. A better two-way coupling between waves and water level may also be needed, especially when replicating this study in a more wave-dominated region, given that in this research, surge and wave are modelled separately, except during the

storyline simulation. Considering the massive tidal range in this region, with a range of more than 3 m along the whole Sofala coastline (more than 7 m near the estuary region as in Figure 2.4b), the chosen location for wave observation is shown to be too shallow, thereby violating the deep-water assumption. Thus, future studies should also carefully assess the optimal location for deep-water wave observation.

- **Include rainfall and fluvial forcing and direct wind hazard to capture full TC-induced compound hazard.** Tropical cyclones often bring intense rainfall, leading to substantial pluvial and fluvial flooding, as demonstrated by the aftermath of TC Idai in deltaic regions such as the Buzi and Pungwe river systems. Moreover, direct wind damage to buildings and crops is also shown to be significant. These forcings are not yet taken into consideration in this study. Future research should incorporate rainfall-runoff modelling, river discharge, and direct wind damage into the hazard framework. Methods such as the IPET or TCR rainfall models, as well as the CLIMADA wind damage model, can be integrated with the applied Holland1980 wind field model. Especially for the hydrodynamic integration, additional rainfall boundary conditions can be incorporated in a coupled coastal, fluvial and pluvial hydrodynamic model such as SFINCS. Furthermore, applying multivariate statistics would allow a comprehensive assessment of compound flood risks under both current and future climate scenarios.

References

Athanasiou, P. et al. (2024). “Global Coastal Characteristics (GCC): a global dataset of geophysical, hydrodynamic, and socioeconomic coastal indicators”. In: *Earth System Science Data* 16, pp. 3433–3452. DOI: 10.5194/essd-16-3433-2024. URL: https://doi.org/10.5194/essd-16-3433-2024.

Bakker, T. M. et al. (2022). “Estimating tropical cyclone-induced wind, waves, and surge: A general methodology based on representative tracks”. In: *Coastal Engineering* 176, p. 104154. DOI: 10.1016/j.coastaleng.2022.104154.

Benito, I. et al. (2024). “Stochastic coastal flood risk modelling for the east coast of Africa”. In: *npj Natural Hazards* 1, p. 10. DOI: 10.1038/s44304-024-00010-1. URL: https://doi.org/10.1038/s44304-024-00010-1.

Bessafi, M. and M. C. Wheeler (2006). “Modulation of South Indian Ocean Tropical Cyclones by the Madden–Julian Oscillation and Convectively Coupled Equatorial Waves”. In: *Monthly Weather Review* 134.3, pp. 638–656. DOI: 10.1175/MWR3087.1. URL: https://doi.org/10.1175/MWR3087.1.

Bhattacharyya, M. and G. Ritolia (2008). “Conditional VaR using EVT – Towards a planned margin scheme”. In: *International Review of Financial Analysis* 17.2, pp. 382–395. ISSN: 1057-5219. DOI: 10.1016/j.irfa.2006.08.004. URL: https://doi.org/10.1016/j.irfa.2006.08.004.

Bloemendaal, N. et al. (2020a). “Estimation of global tropical cyclone wind speed probabilities using the STORM dataset”. In: *Scientific Data* 7, p. 377. DOI: 10.1038/s41597-020-00720-x.

Bloemendaal, N. et al. (2020b). “Generation of a global synthetic tropical cyclone hazard dataset using STORM”. In: *Scientific Data* 7, p. 40. DOI: 10.1038/s41597-020-0381-2.

Bloemendaal, N. et al. (2020c). *STORM IBTrACS present climate synthetic tropical cyclone tracks*. DOI: 10.4121/12706085. URL: https://data.4tu.nl/articles/dataset/STORM_IBTrACS_present_climate_synthetic_tropical_cyclone_tracks/12706085.

— (2021). *STORM Climate Change synthetic tropical cyclone tracks*. DOI: 10.4121/14237678. URL: https://data.4tu.nl/articles/dataset/STORM_Climate_Change_synthetic_tropical_cyclone_tracks/14237678.

Bloemendaal, N. et al. (2022). “A globally consistent local-scale assessment of future tropical cyclone risk”. In: *Science Advances* 8.17, eabm8438. DOI: 10.1126/sciadv.abm8438.

Booij, N., R. C. Ris, and L. H. Holthuijsen (1999). “A third-generation wave model for coastal regions: 1. Model description and validation”. In: *Journal of Geophysical Research: Oceans* 104.C4, pp. 7649–7666. DOI: 10.1029/98JC02622.

Bowyer, P. J. and A. W. MacAfee (2005). “The Theory of Trapped-Fetch Waves with Tropical Cyclones—An Operational Perspective”. In: *Weather and Forecasting* 20.2, pp. 229–244. DOI: 10.1175/WAF849.1. URL: https://doi.org/10.1175/WAF849.1.

Britannica, E. (2025). *Mozambique*. Online article. Accessed: 2025-04-30. URL: https://www.britannica.com/place/Mozambique.

Caires, S. (Oct. 2016). “A Comparative Simulation Study of the Annual Maxima and the Peaks-Over-Threshold Methods”. In: *Journal of Offshore Mechanics and Arctic Engineering* 138.5, p. 051601. DOI: 10.1115/1.4033563. URL: https://doi.org/10.1115/1.4033563.

Camargo, S. J. et al. (2007). “Seasonal tropical cyclone forecasts”. In: *WMO Bulletin* 56.4, p. 297.

Cardone, V. J. and A. T. Cox (2013). “Tropical Cyclone Marine Surface Wind Modeling: The Shape of the Radial Wind Profile Matters”. In: pp. 941–959. DOI: 10.1061/9780784412626.082. URL: https://doi.org/10.1061/9780784412626.082.

Chavas, D. R., N. Lin, and K. Emanuel (2015). “A Model for the Complete Radial Structure of the Tropical Cyclone Wind Field. Part I: Comparison with Observed Structure”. In: *Journal of the Atmospheric Sciences* 72.9, pp. 3647–3662. DOI: 10.1175/JAS-D-15-0014.1. URL: https://doi.org/10.1175/JAS-D-15-0014.1.

CIESIN (2018). *Global High Resolution Population Denominators Project - Funded by The Bill and Melinda Gates Foundation (OPP1134076)*. Online report. Accessed: 2025-04-30. URL: https://dx.doi.org/10.5258/SOTON/WP00675.

Codiga, D. L. (2011). *Unified Tidal Analysis and Prediction Using the UTide Matlab Functions*. Technical Report 2011-01. Narragansett, RI: Graduate School of Oceanography, University of Rhode Island, p. 59. URL: ftp://www.po.gso.uri.edu/pub/downloads/codiga/pubs/2011Codiga-UTide-Report.pdf.

Coles, S. G. and J. A. Tawn (1994). "Statistical Methods for Multivariate Extremes: An Application to Structural Design". In: *Journal of the Royal Statistical Society: Series C (Applied Statistics)* 43.1, pp. 1–31. DOI: 10.2307/2986112. URL: https://doi.org/10.2307/2986112.

Davis Jr., R. A. and M. O. Hayes (1984). "What is a wave dominated coast?" In: *Marine Geology* 60.1-4, pp. 313–329. DOI: 10.1016/0025-3227(84)90155-5. URL: https://doi.org/10.1016/0025-3227(84)90155-5.

Deltares (2021). *Beira Coastal Protection Preparation Study: Flood Hazard Modelling*. Tech. rep. Deltares and Royal HaskoningDHV.

— (2024a). *dfm_tools: Tools for Delft3D Flexible Mesh*. https://github.com/Deltares/dfm_tools. Accessed: 2024-11-18.

— (2024b). *HurryWave - an instationary wave model on ocean scales (Validation Report)*. Tech. rep. Deltares.

Dullaart, J., S. Muis, N. Bloemendaal, et al. (2021). "Accounting for tropical cyclones more than doubles the global population exposed to low-probability coastal flooding". In: *Communications Earth & Environment* 2, p. 135. DOI: 10.1038/s43247-021-00204-9. URL: https://doi.org/10.1038/s43247-021-00204-9.

E.-E.-Consortium (2018). *EC-Earth3P-HR model output prepared for CMIP6 HighResMIP*. DOI: 10.22033/ESGF/CMIP6.2323. URL: https://doi.org/10.22033/ESGF/CMIP6.2323.

Egbert, G. D. and S. Y. Erofeeva (2002). "Efficient Inverse Modeling of Barotropic Ocean Tides". In: *Journal of Atmospheric and Oceanic Technology* 19.2, pp. 183–204. DOI: 10.1175/1520-0426(2002)019<0183:EIMOBO>2.0.CO;2. URL: https://doi.org/10.1175/1520-0426(2002)019%3C0183:EIMOBO%3E2.0.CO;2.

Eilander et al. (2023a). "A globally applicable framework for compound flood hazard modeling". In: *Natural Hazards and Earth System Sciences* 23.2, pp. 823–846. DOI: 10.5194/nhess-23-823-2023.

Eilander et al. (2023b). "Modeling compound flood risk and risk reduction using a globally applicable framework: a pilot in the Sofala province of Mozambique". In: *Natural Hazards and Earth System Sciences* 23, pp. 2251–2272. DOI: 10.5194/nhess-23-2251-2023. URL: https://doi.org/10.5194/nhess-23-2251-2023.

Emanuel, K. and R. Rotunno (2011). "Self-Stratification of Tropical Cyclone Outflow. Part I: Implications for Storm Structure". In: *Journal of the Atmospheric Sciences* 68.9, pp. 2236–2249. DOI: 10.1175/JAS-D-10-05024.1. URL: https://doi.org/10.1175/JAS-D-10-05024.1.

Emanuel, K. et al. (2013). "Influence of Tropical Tropopause Layer Cooling on Atlantic Hurricane Activity". In: *Journal of Climate* 26.7, pp. 2288–2301. DOI: 10.1175/JCLI-D-12-00242.1. URL: https://doi.org/10.1175/JCLI-D-12-00242.1.

Emanuel, K. (2008). "The Hurricane–Climate Connection". In: *Bulletin of the American Meteorological Society* 89.5. Accessed: 2025-04-30, ES10–ES20. URL: http://www.jstor.org/stable/26216815.

Emanuel, K. et al. (2006). "A Statistical Deterministic Approach to Hurricane Risk Assessment". In: *Bulletin of the American Meteorological Society* 87, S1–S5. DOI: 10.1175/BAMS-87.3.Emanuel. URL: https://doi.org/10.1175/BAMS-87.3.Emanuel.

Filipe, E. and S. Norfolk (2017). *Changing Landscapes in Mozambique: Why Pro-Poor Land Policy Matters*. Online article. Accessed: 2025-04-30. URL: https://pubs.iied.org/17356IIED/.

GEBCO Compilation Group (2024). *GEBCO 2024 Grid - Gridded Bathymetry Data*. https://www.gebco.net/data_and_products/gridded_bathymetry_data/gebco_2024/. Last accessed: 24 September 2024.

Gori, A., N. Lin, D. Xi, et al. (2022). "Tropical cyclone climatology change greatly exacerbates US extreme rainfall–surge hazard". In: *Nature Climate Change* 12, pp. 171–178. DOI: 10.1038/s41558-021-01272-7. URL: https://doi.org/10.1038/s41558-021-01272-7.

Goulart, H. et al. (2024). "Compound flood impacts from Hurricane Sandy on New York City in climate-driven storylines". In: *Natural Hazards and Earth System Sciences* 24, pp. 29–45. DOI: 10.5194/nhess-24-29-2024. URL: https://doi.org/10.5194/nhess-24-29-2024.

Goulart, H. et al. (2025). “Exploring coastal climate adaptation through storylines: Insights from Cyclone Idai in Beira, Mozambique”. In: *Cell Reports Sustainability* 2.1. DOI: 10.1016/j.crsus.2024.100270. URL: https://doi.org/10.1016/j.crsus.2024.100270.

Gray, W. M. (1998). “The formation of tropical cyclones”. In: *Meteorology and Atmospheric Physics* 67, pp. 37–69. DOI: 10.1007/BF01277501. URL: https://doi.org/10.1007/BF01277501.

Grimley, L. E., K. E. H. Beatty, A. Sebastian, et al. (2024). “Climate change exacerbates compound flooding from recent tropical cyclones”. In: *npj Nature Hazards* 1, p. 45. DOI: 10.1038/s44304-024-00046-3. URL: https://doi.org/10.1038/s44304-024-00046-3.

Grossmann-Matheson, G., I. R. Young, A. Meucci, et al. (2024a). “Global changes in extreme tropical cyclone wave heights under projected future climate conditions”. In: *Scientific Reports* 14, p. 31797. DOI: 10.1038/s41598-024-82892-9. URL: https://doi.org/10.1038/s41598-024-82892-9.

— (2024b). “Global tropical cyclone extreme wave height climatology”. In: *Scientific Reports* 14, p. 4167. DOI: 10.1038/s41598-024-54691-9. URL: https://doi.org/10.1038/s41598-024-54691-9.

Grossmann-Matheson, G. et al. (2025). “A model for the spatial distribution of ocean wave parameters in tropical cyclones”. In: *Ocean Engineering* 317, p. 120091. ISSN: 0029-8018. DOI: 10.1016/j.oceaneng.2024.120091. URL: https://doi.org/10.1016/j.oceaneng.2024.120091.

Grossmann-Matheson, I. R. Young, et al. (2023). “Development and validation of a parametric tropical cyclone wave height prediction model”. In: *Ocean Engineering* 283, p. 115353. ISSN: 0029-8018. DOI: 10.1016/j.oceaneng.2023.115353. URL: https://doi.org/10.1016/j.oceaneng.2023.115353.

Hammond, W. et al. (2021). *ESA WorldCover 10 m 2020 V100*. https://doi.org/10.5281/zenodo.5571936. Last accessed: 24 September 2024. DOI: 10.5281/zenodo.5571936.

Harris, D. L. (1963). *Characteristics of the Hurricane Storm Surge*. Tech. rep. 48. Department of Commerce, Weather Bureau.

Heffernan, J. E. and J. A. Tawn (2004). “A Conditional Approach for Multivariate Extreme Values (with Discussion)”. In: *Journal of the Royal Statistical Society: Series B (Statistical Methodology)* 66.3, pp. 497–546. DOI: 10.1111/j.1467-9868.2004.02050.x. URL: https://doi.org/10.1111/j.1467-9868.2004.02050.x.

Holland, G. (1997). “The Maximum Potential Intensity of Tropical Cyclones”. In: *Journal of the Atmospheric Sciences* 54.21, pp. 2519–2541. DOI: 10.1175/1520-0469(1997)054<2519:TMPIOT>2.0.CO;2. URL: https://doi.org/10.1175/1520-0469(1997)054%3C2519:TMPIOT%3E2.0.CO;2.

Holland, G. J. (1980). “An Analytic Model of the Wind and Pressure Profiles in Hurricanes”. In: *Monthly Weather Review* 108, pp. 1212–1218. DOI: 10.1175/1520-0493(1980)108<1212:AAMOTW>2.0.CO;2.

Holland, G. J., J. I. Belanger, and A. Fritz (2010). “A Revised Model for Radial Profiles of Hurricane Winds”. In: *Monthly Weather Review* 138.12, pp. 4393–4401. DOI: 10.1175/2010MWR3317.1. URL: https://doi.org/10.1175/2010MWR3317.1.

Inman, D. L. and C. E. Nordstrom (1971). “On the tectonic and morphologic classification of coasts”. In: *Journal of Geology* 79.1, pp. 1–21. DOI: 10.1086/627583. URL: https://doi.org/10.1086/627583.

International Hydrographic Organization (2024). *Tide Station Data: Beira, Mozambique*. https://iho.int/en/tide-stations. Accessed: 2024-05-22.

IPET (2006). *Performance Evaluation of the New Orleans and Southeast Louisiana Hurricane Protection System: Draft Final Report, Volume VIII—Engineering and Operational Risk and Reliability Analysis*. Tech. rep. Available from: https://www.hsdl.org/?view&did=479802. U.S. Army Corps of Engineers. URL: https://www.hsdl.org/?view%5C&did=479802.

Jakobsen, F. and H. Madsen (2004). “Comparison and further development of parametric tropical cyclone models for storm surge modelling”. In: *Journal of Wind Engineering and Industrial Aerodynamics* 92.5, pp. 375–391. ISSN: 0167-6105. DOI: 10.1016/j.jweia.2004.01.003. URL: https://doi.org/10.1016/j.jweia.2004.01.003.

James, M. K. and L. B. Mason (2005). “Synthetic tropical cyclone database”. In: *Journal of Waterway, Port, Coastal, and Ocean Engineering* 131.4, pp. 181–192. DOI: 10.1061/(ASCE)0733-950X(2005)131:4(181). URL: https://doi.org/10.1061/(ASCE)0733-950X(2005)131:4(181).

Kernkamp, H. W. J. et al. (2011). “Efficient scheme for the shallow water equations on unstructured grids with application to the Continental Shelf”. In: *Ocean Dynamics* 61.8, pp. 1175–1188. DOI: 10.1007/s10236-011-0423-6. URL: https://doi.org/10.1007/s10236-011-0423-6.

Kim, H. et al. (2014). “Tropical Cyclone Simulation and Response to CO_2 Doubling in the GFDL CM2.5 High-Resolution Coupled Climate Model”. In: *Journal of Climate* 27.20, pp. 8034–8054. DOI: 10.1175/JCLI-D-13-00475.1. URL: https://doi.org/10.1175/JCLI-D-13-00475.1.

Knaff, J. A., J. P. Kossin, and M. DeMaria (2003). “Annular Hurricanes”. In: *Weather and Forecasting* 18.2, pp. 204–223. DOI: 10.1175/1520-0434(2003)018<0204:AH>2.0.CO;2. URL: https://doi.org/10.1175/1520-0434(2003)018%3C0204:AH%3E2.0.CO;2.

Knaff, J. et al. (2007). “Statistical tropical cyclone wind radii prediction using climatology and persistence”. In: *Weather and Forecasting* 22.4, pp. 781–791. DOI: 10.1175/WAF1026.1. URL: https://doi.org/10.1175/WAF1026.1.

Knapp, K. R. et al. (2010). “The international best track archive for climate stewardship (IBTrACS) unifying tropical cyclone data”. In: *Bulletin of the American Meteorological Society* 91.3, pp. 363–376. DOI: 10.1175/2009BAMS2755.1. URL: https://doi.org/10.1175/2009BAMS2755.1.

Kropf, C. M. et al. (2022). “Uncertainty and sensitivity analysis for probabilistic weather and climate-risk modelling: an implementation in CLIMADA v.3.1.0”. In: *Geoscientific Model Development* 15, pp. 7177–7201. DOI: 10.5194/gmd-15-7177-2022.

Kurian, N. P. et al. (2009). “Coastal flooding due to synoptic scale, meso-scale and remote forcings”. In: *Natural Hazards* 48, pp. 259–273. DOI: 10.1007/s11069-008-9260-4. URL: https://doi.org/10.1007/s11069-008-9260-4.

Lee, C. et al. (2020). “Statistical–Dynamical Downscaling Projections of Tropical Cyclone Activity in a Warming Climate: Two Diverging Genesis Scenarios”. In: *Journal of Climate* 33, pp. 4815–4834. DOI: 10.1175/JCLI-D-19-0452.1. URL: https://doi.org/10.1175/JCLI-D-19-0452.1.

Lee, C. Y. et al. (2018). “An Environmentally Forced Tropical Cyclone Hazard Model”. In: *Journal of Advances in Modeling Earth Systems* 10, pp. 223–241. DOI: 10.1002/2017MS001186. URL: https://doi.org/10.1002/2017MS001186.

Lee, J.-W. et al. (2021). “Rapid prediction of peak storm surge from tropical cyclone track time series using machine learning”. In: *Coastal Engineering* 170, p. 104024. ISSN: 0378-3839. DOI: 10.1016/j.coastaleng.2021.104024. URL: https://doi.org/10.1016/j.coastaleng.2021.104024.

Leijnse, T. et al. (2021). “Modeling compound flooding in coastal systems using a computationally efficient reduced-physics solver: Including fluvial, pluvial, tidal, wind- and wave-driven processes”. In: *Coastal Engineering* 163, p. 103796. ISSN: 0378-3839. DOI: 10.1016/j.coastaleng.2020.103796. URL: https://doi.org/10.1016/j.coastaleng.2020.103796.

Leijnse, T. et al. (2022). “Generating reliable estimates of tropical-cyclone-induced coastal hazards along the Bay of Bengal for current and future climates using synthetic tracks”. In: *Natural Hazards and Earth System Sciences* 22, pp. 1863–1891. DOI: 10.5194/nhess-22-1863-2022.

Leijnse, T. et al. (2024). “Estimating nearshore infragravity wave conditions at large spatial scales”. In: *Frontiers in Marine Science* 11. ISSN: 2296-7745. DOI: 10.3389/fmars.2024.1355095. URL: https://www.frontiersin.org/journals/marine-science/articles/10.3389/fmars.2024.1355095.

Leijnse, T. et al. (2025). “The importance of waves in large-scale coastal compound flooding: A case study of Hurricane Florence (2018)”. In: *Coastal Engineering* 199, p. 104726. ISSN: 0378-3839. DOI: 10.1016/j.coastaleng.2025.104726.

Lin, N., K. Emanuel, M. Oppenheimer, et al. (2012). “Physically based assessment of hurricane surge threat under climate change”. In: *Nature Climate Change* 2, pp. 462–467. DOI: 10.1038/nclimate1389. URL: https://doi.org/10.1038/nclimate1389.

Marcos, M. et al. (2019). “Increased extreme coastal water levels due to the combined action of storm surges and wind waves”. In: *Geophysical Research Letters* 46, pp. 4356–4364. DOI: 10.1029/2019GL082599. URL: https://doi.org/10.1029/2019GL082599.

Mares-Nasarre, P., M. R. van Gent, and O. Morales-Nápoles (2024). “A copula-based model to describe the uncertainty of overtopping variables on mound breakwaters”. In: *Coastal Engineering* 189, p. 104483. ISSN: 0378-3839. DOI: https://doi.org/10.1016/j.coastaleng.2024.104483.

Marsooli, R. et al. (2019). “Climate change exacerbates hurricane flood hazards along US Atlantic and Gulf Coasts in spatially varying patterns”. In: *Nature Communications* 10, p. 3785. DOI: 10.1038/s41467-019-11755-z. URL: https://doi.org/10.1038/s41467-019-11755-z.

Masson-Delmotte, V. e. a., ed. (2021). *Climate Change 2021: The Physical Science Basis. Contribution of Working Group I to the Sixth Assessment Report of the Intergovernmental Panel on Climate*

Change. Cambridge, United Kingdom and New York, NY, USA: Cambridge University Press, p. 2391. DOI: 10.1017/9781009157896. URL: https://doi.org/10.1017/9781009157896.

Matyas, C. J. (2015). "Tropical cyclone formation and motion in the Mozambique Channel". In: *International Journal of Climatology* 35.3, pp. 375–390. DOI: 10.1002/joc.3985. URL: https://doi.org/10.1002/joc.3985.

Meiler, S., T. Vogt, N. Bloemendaal, et al. (2022). "Intercomparison of regional loss estimates from global synthetic tropical cyclone models". In: *Nature Communications* 13.1, p. 6156. DOI: 10.1038/s41467-022-33918-1. URL: https://doi.org/10.1038/s41467-022-33918-1.

Meiler, S. et al. (2025). "Navigating and attributing uncertainty in future tropical cyclone risk estimates". In: *Science Advances* 11, eadn4607. DOI: 10.1126/sciadv.adn4607. URL: https://www.science.org/doi/10.1126/sciadv.adn4607.

Météo-France (2025). *Frequently Asked Questions about Tropical Cyclones*. http://www.meteo.fr/temps/domtom/La_Reunion/webcmrs9.0/anglais/faq/FAQ_Ang_G.html. Accessed: 2025-05-30.

Morim, J. et al. (2019). "Robustness and uncertainties in global multivariate wind-wave climate projections". In: *Nature Climate Change* 9, pp. 711–718. DOI: 10.1038/s41558-019-0542-5. URL: https://doi.org/10.1038/s41558-019-0542-5.

Muis, S. et al. (2023). "Global projections of storm surges using high-resolution CMIP6 climate models". In: *Earth's Future* 11, e2023EF003479. DOI: 10.1029/2023EF003479. URL: https://doi.org/10.1029/2023EF003479.

Mulet, S. et al. (2021). "The New CNES-CLS18 Global Mean Dynamic Topography". In: *Ocean Science* 17.3, pp. 789–808. DOI: 10.5194/os-17-789-2021.

Nederhoff, K., T. W. B. Leijnse, K. Parker, et al. (2024). "Tropical or extratropical cyclones: what drives the compound flood hazard, impact, and risk for the United States Southeast Atlantic coast?" In: *Natural Hazards* 120, pp. 8779–8825. DOI: 10.1007/s11069-024-06552-x. URL: https://doi.org/10.1007/s11069-024-06552-x.

Nederhoff, K. et al. (2021). "Simulating synthetic tropical cyclone tracks for statistically reliable wind and pressure estimations". In: *Natural Hazards and Earth System Sciences* 21, pp. 861–878. DOI: 10.5194/nhess-21-861-2021. URL: https://doi.org/10.5194/nhess-21-861-2021.

Needham, H. F., B. D. Keim, and D. Sathiaraj (2015). "A review of tropical cyclone-generated storm surges: Global data sources, observations, and impacts". In: *Reviews of Geophysics* 53.2, pp. 545–591. DOI: 10.1002/2014RG000477. URL: https://doi.org/10.1002/2014RG000477.

NOAA (2008). *Introduction to Storm Surge*. http://www.nws.noaa.gov/om/hurricane/resources/surge_intro.pdf.

— (2019). *Saffir-Simpson Hurricane Wind Scale*. https://www.nhc.noaa.gov/aboutsshws.php. National Hurricane Center and Central Pacific Hurricane Center, accessed 3 May 2025.

Ormondt, M. van, K. Nederhoff, and A. van Dongeren (May 2020). "Delft Dashboard: a quick set-up tool for hydrodynamic models". In: *Journal of Hydroinformatics* 22.3, pp. 510–527. DOI: 10.2166/hydro.2020.092. URL: https://doi.org/10.2166/hydro.2020.092.

Pall, P. et al. (2024). "Assessing South Indian Ocean tropical cyclone characteristics in HighResMIP simulations". In: *International Journal of Climatology* 44.13, pp. 4792–4808. DOI: 10.1002/joc.8609. URL: https://doi.org/10.1002/joc.8609.

Parodi, M. U. et al. (2020). "Uncertainties in coastal flood risk assessments in small island developing states". In: *Natural Hazards and Earth System Sciences* 20, pp. 2397–2414. DOI: 10.5194/nhess-20-2397-2020.

Perry, Z. et al. (2024). "Analysing the atmospheric-oceanic conditions driving the sustained long track and intensity of Tropical Cyclone Freddy". In: *Tropical Cyclone Research and Review* 13.4, pp. 356–388. ISSN: 2225-6032. DOI: 10.1016/j.tcrr.2024.11.008. URL: https://doi.org/10.1016/j.tcrr.2024.11.008.

Pronk, M., A. Hooijer, D. Eilander, et al. (2024). "DeltaDTM: A Global Coastal Digital Terrain Model". In: *Scientific Data* 11, p. 273. DOI: 10.1038/s41597-024-03091-9.

Rappaport, E. N. and J. J. Fernández-Partagás (1995). *The Deadliest Atlantic Tropical Cyclones, 1492–1994*. Tech. rep. 47. National Hurricane Center. URL: https://repository.library.noaa.gov/view/noaa/49728.

Rego, J. L. and C. Li (2009). "On the importance of the forward speed of hurricanes in storm surge forecasting: A numerical study". In: *Geophysical Research Letters* 36, p. L07609. DOI: 10.1029/2008GL036953. URL: https://doi.org/10.1029/2008GL036953.

Resio, D. T. and J. J. Westerink (2008). “Modeling the physics of storm surges”. In: *Physics Today* 61.9, pp. 33–38.

Resnick, S. I. (1987). *Extreme Values, Regular Variation, and Point Processes*. Vol. 4. Springer Series in Operations Research and Financial Engineering. Springer Science & Business Media. ISBN: 9780387759593.

Richter, R., M. Behrens, and J. Döllner (2013). “Object Class Segmentation of Massive 3D Point Clouds of Urban Areas Using Point Cloud Topology”. In: *International Journal of Remote Sensing* 34.23, pp. 8408–8424. DOI: 10.1080/01431161.2013.838710. URL: https://doi.org/10.1080/01431161.2013.838710.

Roberts, M. (2017). *HadGEM3-GC31-HM model output prepared for CMIP6 HighResMIP*. DOI: 10.22033/ESGF/CMIP6.446. URL: https://doi.org/10.22033/ESGF/CMIP6.446.

Roberts, M. et al. (2020). “Projected Future Changes in Tropical Cyclones Using the CMIP6 HighResMIP Multimodel Ensemble”. In: *Geophysical Research Letters* 47.21, e2020GL088662. DOI: 10.1029/2020GL088662. URL: https://doi.org/10.1029/2020GL088662.

Roelvink, D. et al. (2025). “SnapWave: fast, implicit wave transformation from offshore to nearshore”. In: *EGUsphere*. preprint, under review for *Geoscientific Model Development*. DOI: 10.5194/egusphere-2025-492. URL: https://doi.org/10.5194/egusphere-2025-492.

Scoccimarro, E., A. Bellucci, and D. Peanno (2017). *CMCC-CM2-VHR4 model output prepared for CMIP6 HighResMIP*. DOI: 10.22033/ESGF/CMIP6.1367. URL: https://doi.org/10.22033/ESGF/CMIP6.1367.

Steinmann, C. B., B. P. Guillod, C. Fairless, et al. (2023). “A generalized framework for designing open-source natural hazard parametric insurance”. In: *Environmental Systems and Decisions* 43, pp. 555–568. DOI: 10.1007/s10669-023-09934-x.

Stockdon, H. F. et al. (2006). “Empirical parameterization of setup, swash, and runup”. In: *Coastal Engineering* 53.7, pp. 573–588. DOI: 10.1016/j.coastaleng.2005.12.005.

Tolman, H. L. (2009). *User manual and system documentation of WAVEWATCH III^{TM} version 3.14*. Technical Note MMAB Contribution No. 276. Camp Springs, MD: NOAA/NWS/NCEP – Marine Modeling and Analysis Branch. URL: https://polar.ncep.noaa.gov/mmab/papers/tn276/MMAB_276.pdf.

Trisos, C. et al. (2022). “Chapter 9: Africa”. In: *Climate Change 2022: Impacts, Adaptation and Vulnerability*. Ed. by H.-O. Pörtner et al. Cambridge, United Kingdom and New York, NY, USA: Cambridge University Press, pp. 2043–2121.

Uhlhorn, E. W. et al. (2014). “Observed Hurricane Wind Speed Asymmetries and Relationships to Motion and Environmental Shear”. In: *Monthly Weather Review* 142.4, pp. 1290–1311. DOI: 10.1175/MWR-D-13-00249.1. URL: https://doi.org/10.1175/MWR-D-13-00249.1.

UNDP (May 2019). *Post-Disaster Needs Assessment: Cyclone Idai*. Executive Summary. Accessed: 2025-04-30. URL: https://www.undp.org/publications/mozambique-cyclone-idai-post-disaster-needs-assessment-pdnadna.

UNDRR (2024). *Forensic Insights for Future Resilience: Learning from Past Disasters*. https://www.undrr.org/gar. Global Assessment Report (GAR) Special Report. URL: https://www.undrr.org/gar.

UNITAR (2019). *Satellite Analysis and Applied Research: Mapping the Destruction of Tropical Cyclone IDAI, ‘One of the Worst Disasters in the Southern Hemisphere’*. Online article. Accessed: 2025-04-30. URL: https://unitar.org/satellite-analysis-and-applied-research-mapping-destruction-tropical-cyclone-idai-one-worst.

USACE (2002). *Coastal engineering manual, report number 11102-1100*. Washington, DC: US Army Corps of Engineers, p. 477.

Uusitalo, L. et al. (2015). “An overview of methods to evaluate uncertainty of deterministic models in decision support”. In: *Environmental Modelling & Software* 63, pp. 24–31. DOI: 10.1016/j.envsoft.2014.09.017. URL: https://doi.org/10.1016/j.envsoft.2014.09.017.

Vecchi, G. and B. Soden (2007). “Effect of remote sea surface temperature change on tropical cyclone potential intensity”. In: *Nature* 450, pp. 1066–1070. DOI: 10.1038/nature06423. URL: https://doi.org/10.1038/nature06423.

Vincent, E. M. et al. (2011). “Interannual variability of the South Pacific Convergence Zone and implications for tropical cyclone genesis”. In: *Climate Dynamics* 36, pp. 1881–1896. DOI: 10.1007/s00382-009-0716-3. URL: https://doi.org/10.1007/s00382-009-0716-3.

Voldoire, A. (2019). *CNRM-CERFACS CNRM-CM6–1-HR model output prepared for CMIP6 HighResMIP*. DOI: 10.22033/ESGF/CMIP6.1387. URL: https://doi.org/10.22033/ESGF/CMIP6.1387.

Walsh, K. J. E. et al. (2015). "Hurricanes and Climate: The U.S. CLIVAR Working Group on Hurricanes". In: *Bulletin of the American Meteorological Society* 96.6, pp. 997–1017. DOI: 10.1175/BAMS-D-13-00242.1. URL: https://doi.org/10.1175/BAMS-D-13-00242.1.

Walsh, K. J. E. et al. (2016). "Tropical cyclones and climate change". In: *WIREs Climate Change* 7.1, pp. 65–89. DOI: 10.1002/wcc.371. URL: https://doi.org/10.1002/wcc.371.

Wang, S. et al. (2021). "Is the tropical cyclone surge in Shanghai more sensitive to landfall location or intensity change?" In: *Atmospheric Science Letters* 22.10, e1058. DOI: 10.1002/asl2.1058. URL: https://doi.org/10.1002/asl2.1058.

Wei, C.-C. and J.-Y. Cheng (2020). "Nearshore two-step typhoon wind-wave prediction using deep recurrent neural networks". In: *Journal of Hydroinformatics* 22.2, pp. 346–367. DOI: 10.2166/hydro.2019.084. URL: https://doi.org/10.2166/hydro.2019.084.

Williams, J. et al. (2016). "Tide and skew surge independence: New insights for flood risk". In: *Geophysical Research Letters* 43.12, pp. 6410–6417. DOI: 10.1002/2016GL069522. URL: https://doi.org/10.1002/2016GL069522.

Williamson, C. (June 2022). "Exploring Household Vulnerability: The Compounding Loss of Resource and Service Access in Post-Cyclone Idai Beira, Mozambique". Accessed: 2025-04-30. PhD thesis. Waterloo, Ontario, Canada: University of Waterloo. URL: https://uwspace.uwaterloo.ca/items/b6f61b10-42b1-419b-a473-d86ee296e92b.

Woodruff, J., J. Irish, and S. Camargo (2013). "Coastal flooding by tropical cyclones and sea-level rise". In: *Nature* 504, pp. 44–52. DOI: 10.1038/nature12855. URL: https://doi.org/10.1038/nature12855.

World-Bank (Dec. 2019). *Mozambique Economic Update: Mind the Rural Investment Gap*. Report. Accessed: 2025-04-30. URL: https://documents.worldbank.org/curated/en/480651580155354219/pdf/Mozambique-Economic-Update-Mind-the-Rural-Investment-Gap.pdf.

Xu, H. et al. (2022). "Compound flood impact of water level and rainfall during tropical cyclone periods in a coastal city: the case of Shanghai". In: *Natural Hazards and Earth System Sciences* 22, pp. 2347–2358. DOI: 10.5194/nhess-22-2347-2022. URL: https://doi.org/10.5194/nhess-22-2347-2022.

Yamazaki, D., G. A. M. de Almeida, and P. D. Bates (2013). "Improving computational efficiency in global river models by implementing the local inertial flow equation and a vector-based river network map". In: *Water Resources Research* 49, pp. 7221–7235. DOI: 10.1002/wrcr.20552. URL: https://doi.org/10.1002/wrcr.20552.

Young, I. R. (1998). "Observations of the spectra of hurricane generated waves". In: *Ocean Engineering* 25.4–5, pp. 261–276. ISSN: 0029-8018. DOI: 10.1016/S0029-8018(97)00011-5. URL: https://doi.org/10.1016/S0029-8018(97)00011-5.

— (2006). "Directional spectra of hurricane wind waves". In: *Journal of Geophysical Research: Oceans* 111, p. C08020. DOI: 10.1029/2006JC003540. URL: https://doi.org/10.1029/2006JC003540.

— (2017). "A Review of Parametric Descriptions of Tropical Cyclone Wind–Wave Generation". In: *Atmosphere* 8.10, p. 194. DOI: 10.3390/atmos8100194.

Zhang, J. A. and E. W. Uhlhorn (2012). "Hurricane Sea Surface Inflow Angle and an Observation-Based Parametric Model". In: *Monthly Weather Review* 140.11, pp. 3587–3605. DOI: 10.1175/MWR-D-11-00339.1. URL: https://doi.org/10.1175/MWR-D-11-00339.1.

Zheng, F. et al. (2014). "Modeling dependence between extreme rainfall and storm surge to estimate coastal flooding risk". In: *Water Resources Research* 50.3, pp. 2050–2071. DOI: 10.1002/2013WR014616.

Zhu, L., S. M. Quiring, and K. A. Emanuel (2013). "Estimating tropical cyclone precipitation risk in Texas". In: *Geophysical Research Letters* 40.23, pp. 6225–6230. DOI: 10.1002/2013GL058284. URL: https://doi.org/10.1002/2013GL058284.

Zscheischler, J., S. Westra, B. J. J. M. van den Hurk, et al. (2018). "Future climate risk from compound events". In: *Nature Climate Change* 8, pp. 469–477. DOI: 10.1038/s41558-018-0156-3. URL: https://doi.org/10.1038/s41558-018-0156-3.

A

Tide Distribution Validation & Tide-Skew Surge Independence

This appendix relates to the discussion that took place at SubSection 3.2.3. A comparison of the high-water tide elevation kernel density between each STORM variation at the nearest observation point near Beira IHO tide station is presented in Figure A.1. This tide distribution is developed based on mined Delft3D-FM tide-only simulation output at every observation point that is used for skew surge calculation. A sea level rise correction is conducted by subtracting 0.25 m uniformly from the future STORM-GCMs high-water tide distribution. It can be noted from the figure that there is satisfactory agreement between each STORM variation, confirming equivalent tide variability across the different runs. Moreover, the distribution from the Beira IHO tide station is also presented. The comparison with the Beira IHO station demonstrates the hydrodynamic model's performance in replicating the actual tide situation in the study area.

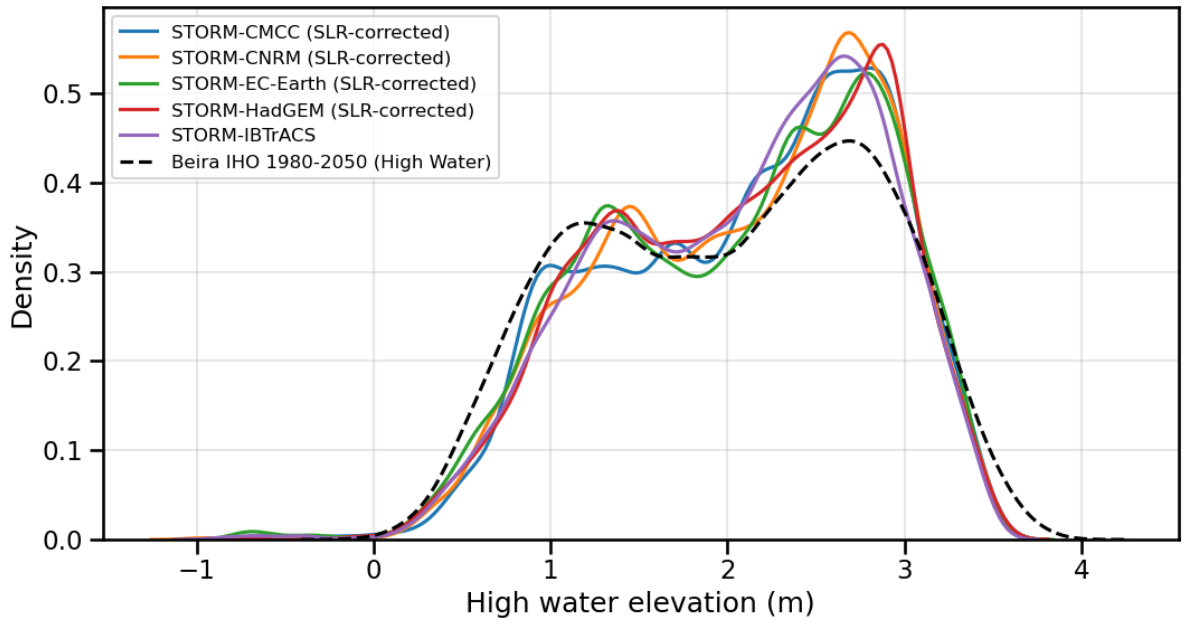

Figure A.1: Kernel density estimates of high-water tide elevations from Delft3D-FM tide-only simulations (STORM variations) at the observation point near the Beira IHO tide station. A uniform sea level rise correction of 0.25 m is applied to the future STORM-GCMs. The nearest tide station, Beira IHO, distribution is also shown for comparison.

Aside from tide distribution, the correlation between tide and skew surge is also evaluated, as shown in the scatter plots presented in Figure A.2. From this figure, we can infer that the correlation between skew surge and its corresponding high tide is almost nonexistent across all STORM variations, with maximum absolute values of 0.08. This finding confirms the validity of the assumptions underlying the choice of skew surge over non-tidal residual, ensuring an independent relationship.

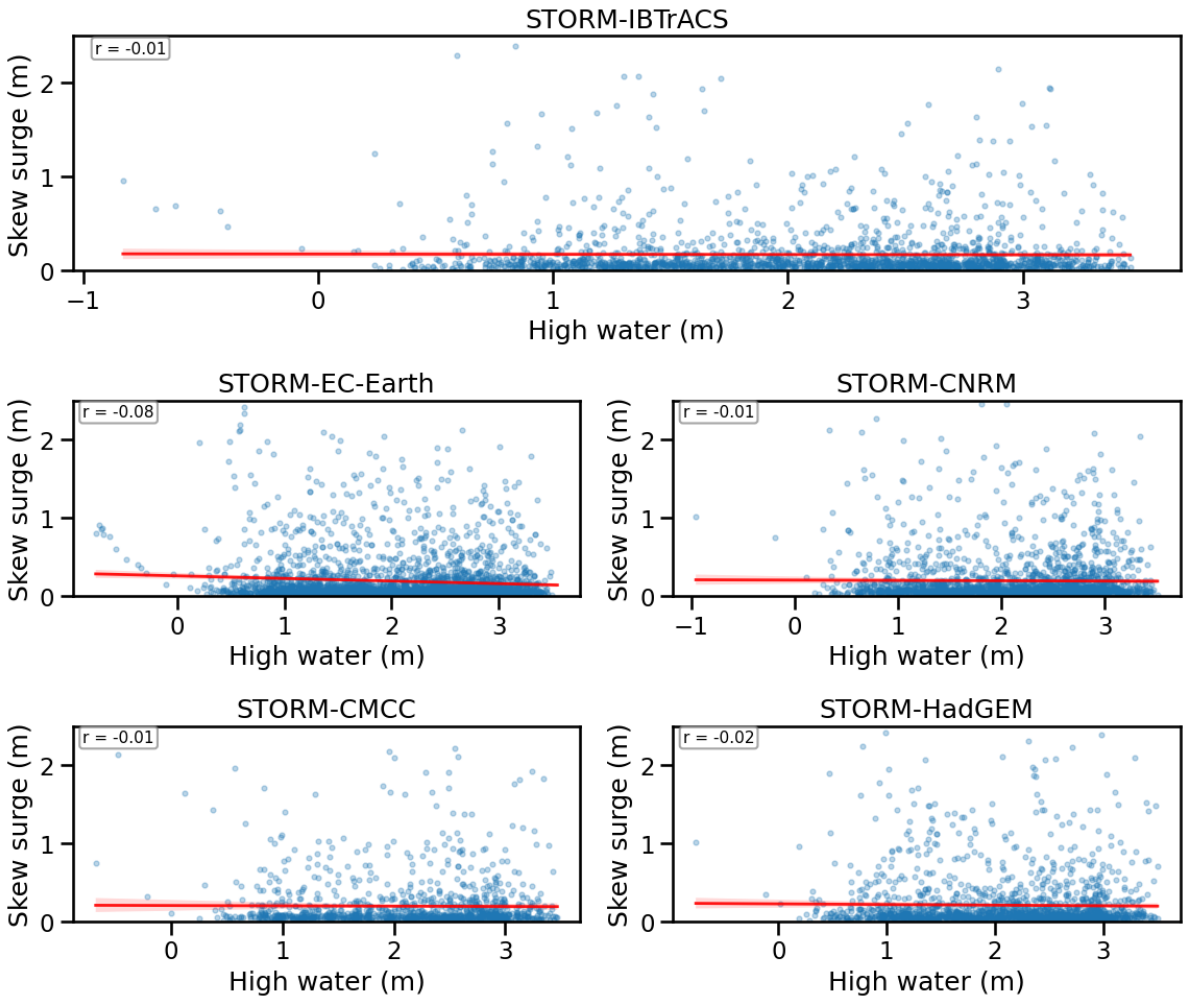

Figure A.2: Scatter plots of skew surge versus corresponding high water for each STORM variation at the Beira observation point. The red line indicates the correlation line, with its value shown in the top left of each scatter plot.

B

IBTrACS vs STORM-IBTrACS Occurrences

The figure below shows the differences in occurrences between the original IBTrACS dataset and STORM-IBTrACS, relating to the discussion that took place in Section 4.1. The comparison of TC intensity (maximum wind speed) between STORM and IBTrACS can be seen in its original publication by Bloemendaal et al. (2020b)

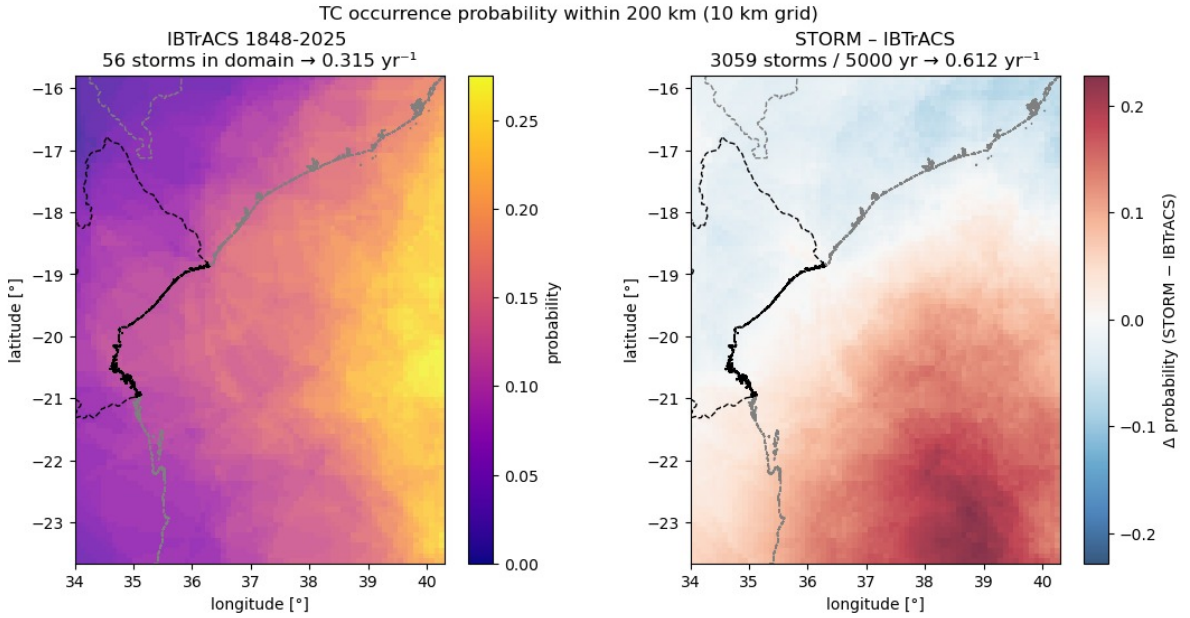

Figure B.1: Yearly probability of at least one tropical cyclone (TC) occurrence within a 200 km radius per 10 km grid cell in the Mozambique Channel. Left: Based on domain-filtered IBTrACS (1980–2023) observations. Right: Difference between STORM (5,000-year synthetic catalogue) and IBTrACS; red areas indicate regions where STORM shows a lower annual occurrence probability than IBTrACS.

C

TC Idai Hindcast Map

Figures below illustrate the result of TC Idai storm surge and wave hindcast in connection to the discussion in Subsection 4.4.1.

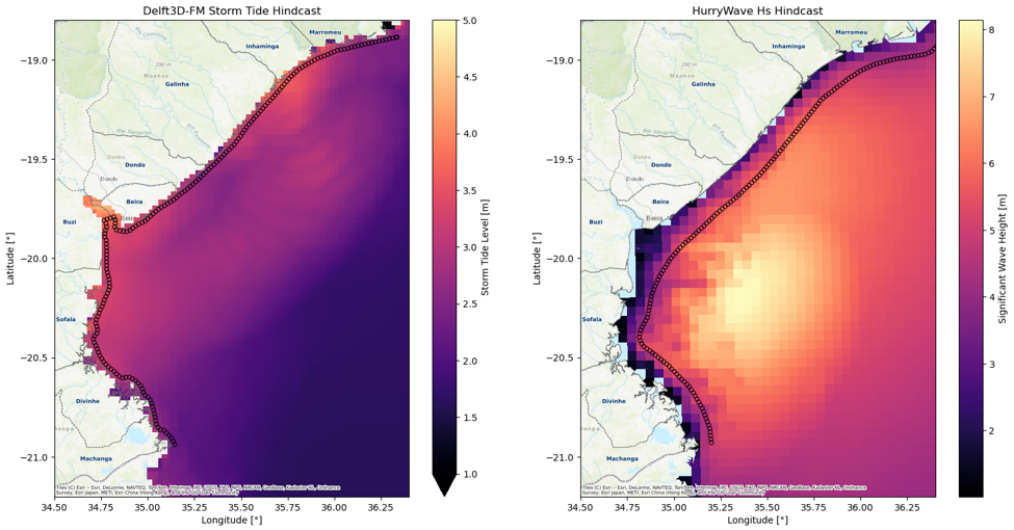

Figure C.1: TC Idai storm surge and wave hindcast. The left plot shows the maximum water level produced using Delft-3D FM, whereas the right plot shows the maximum offshore significant wave height simulated using HurryWave.

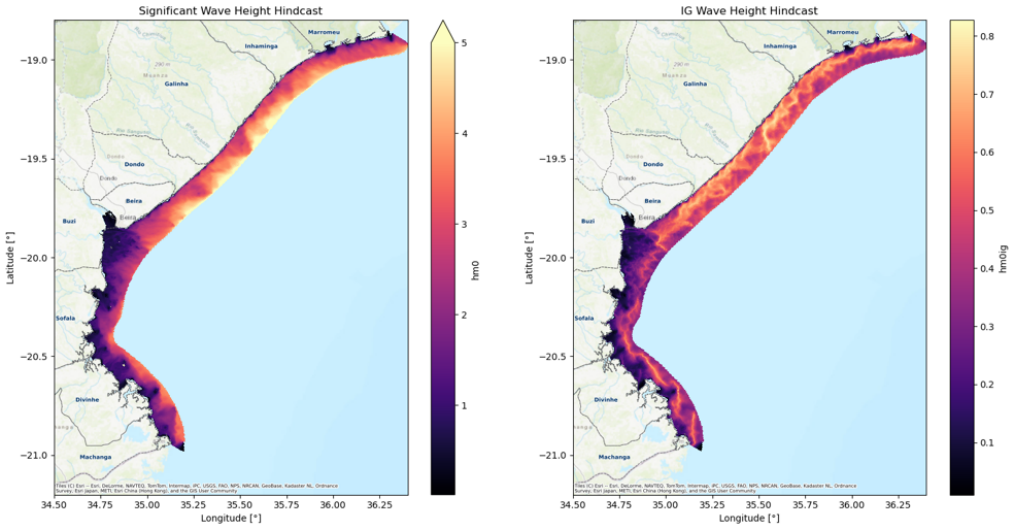

Figure C.2: TC Idai nearshore significant wave height (left) and infragravity wave height (right) hindcast map produced using coupled flow-wave SFINCS-SnapWave model.

D

Marginal Fit Sensitivity

This appendix elaborates on the marginal fit sensitivity discussed briefly in Subsection 5.3.4 on aleatory uncertainties introduced by the sampling of the STORM synthetic tropical cyclone dataset. The sensitivity analysis of the marginal extreme value distribution fit is done by conducting a POT and GPD analysis across all simulated STORM 1000-year subsets. Figure D.2 shows 100-year return period wind speed, skew surge, and significant wave height across different STORM subsets (1st 1000 years to 5th 1000 years) in three different coastal points (5: Machanga, 85: Beira, and 160: Marromeu districts). It can be inferred that the 100-year STORM-IBTrACS and ensemble median of STORM-GCMs value is highly variable across different subsets, except for point 160's wind speed and surge. The variability is even more pronounced once we consider each STORM-GCMs 100-year return levels, with very definitive magnitude differences between each subset. This finding thus highlights the unreliability of using only a single 1000-year subset of STORM, as it introduces significant aleatory uncertainty.

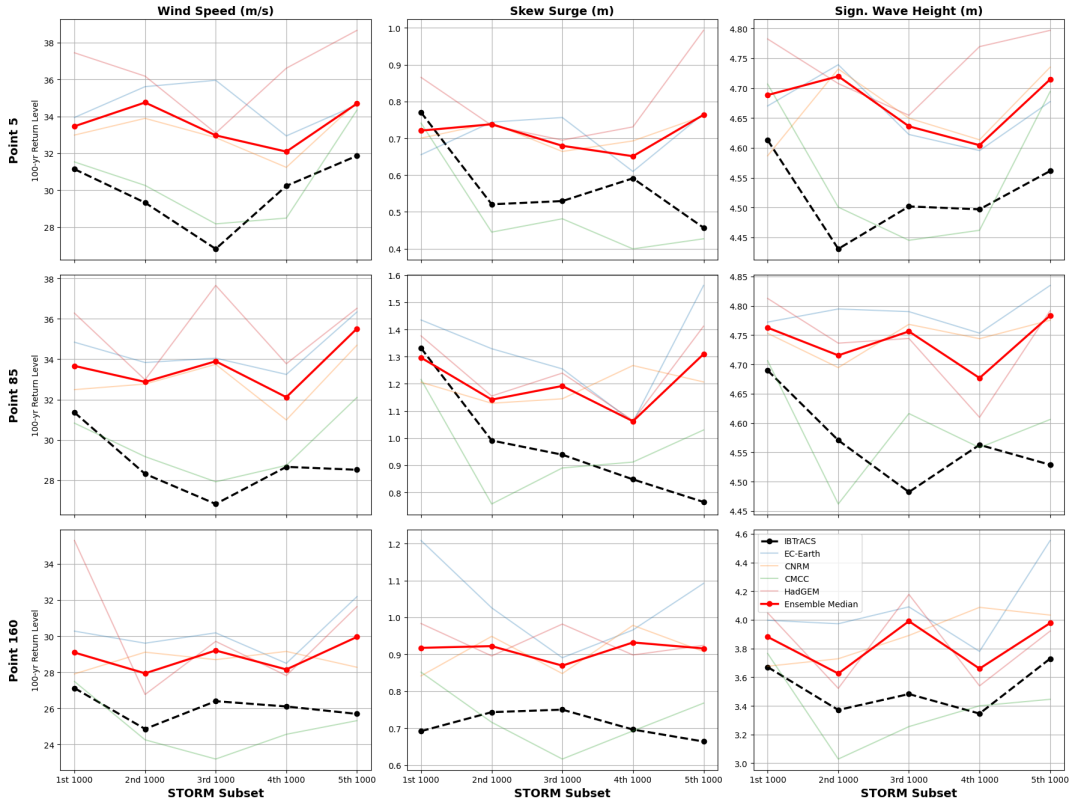

Figure D.1: Sensitivity of 100-year return levels for wind speed, skew surge, and significant wave height across five different non-overlapping 1000-year STORM subsets at three coastal locations: Point 5 (Machanga), Point 85 (Beira), and Point 160 (Marromeu). Each line represents a different STORM-GCM or observational reference (IBTrACS), while the ensemble median is shown in red.

Furthermore, we also tested how the 100-year return levels will look as more STORM subset is taken into account, as shown in Figure D.2. It can be observed from the figure that most of the STORM-IBTrACS and the ensemble median of STORM-GCMs exhibit a convergence pattern as more 1000-year subsets are introduced, particularly for wind speed and wave height. This convergence pattern is also depicted in each STORM-GCM. This finding suggests that 5000 years appears to be an overall justified number of simulated events, as indicated by the convergence, which denotes a minimum possible aleatory uncertainty. Still, upon closer examination of the surge, especially at observation points 5 and 85, the STORM-IBTrACS' return level appears to decrease almost linearly as more subsets are considered, indicating failure to converge. Meaning that, if a larger number of subsets is introduced, the 100-year surge might still be considerably different. This non-convergence pattern is even more pronounced under a higher return period, e.g. in a 1000-year return level as shown in Figure D.3, which is especially problematic when considering that TC Idai is shown to exceed those of a 1000-year return period event (see Figure 4.10). Still, given the limited time resources, the 5000 years' worth of synthetic TC tracks simulated in this study is preferred compared to using only a single STORM subset.

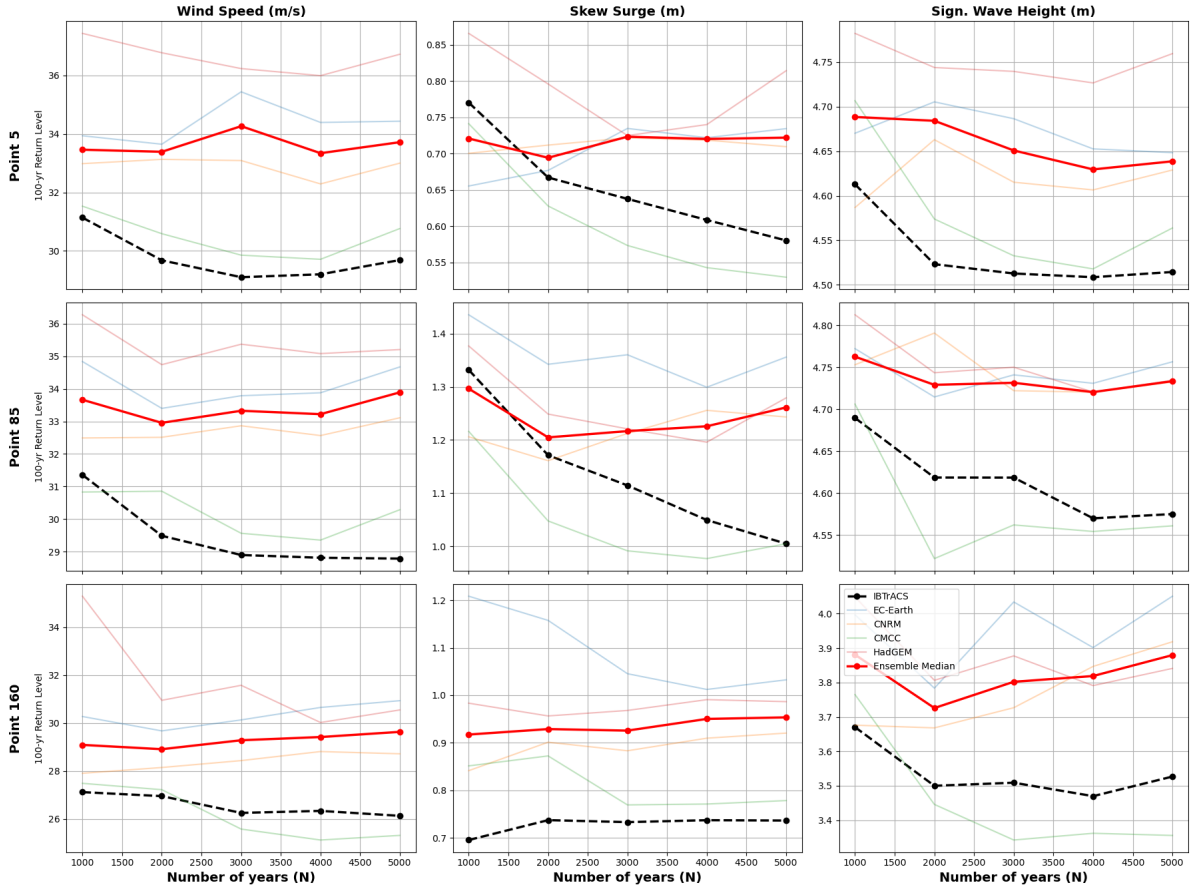

Figure D.2: The 100-year return levels for wind speed, skew surge, and significant wave height as a function of increasing STORM subset size (from 1000 to 5000 years), for Points 5, 85, and 160. Each line represents a STORM-GCM or observational baseline (IBTrACS), with the ensemble median shown in red.

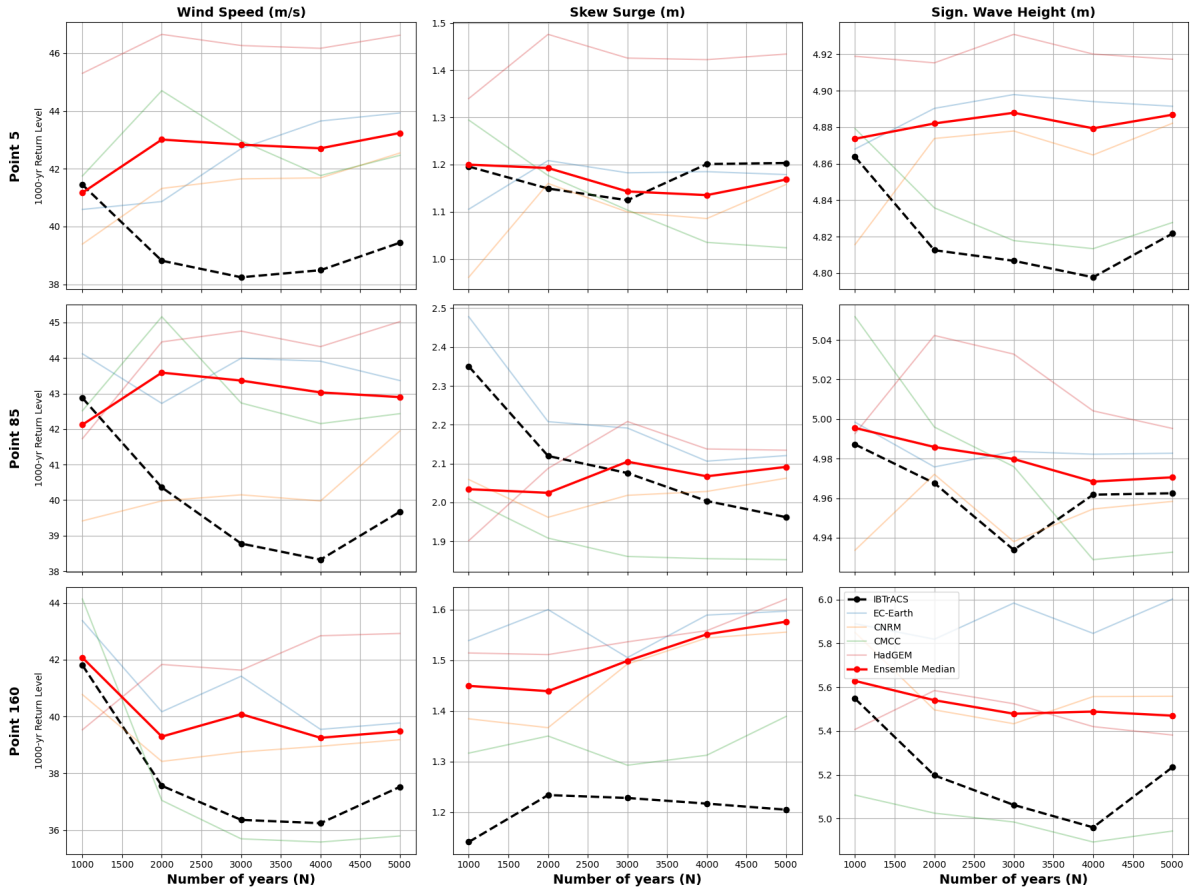

Figure D.3: Same as Figure D.2, but for 1000-year return level